

Universidade de São Paulo
Instituto de Física

Projeto BINGO: Vínculos cosmológicos a partir de simulações de mapas de intensidade de HI

Pablo César Benevides de Carvalho Rossas Motta



Orientador: Prof. Dr. Elcio Abdalla

Dissertação de mestrado apresentada ao Instituto de Física
da Universidade de São Paulo, como requisito parcial para
a obtenção do título de Mestre em Ciências.

Banca Examinadora:

Prof. Dr. Elcio Abdalla - Orientador (IFUSP)

Prof. Dr. Daniel Augusto Turolla Vanzela (IFSC USP)

Prof. Dr. Alberto Vazquez Saa (UNICAMP)

São Paulo

2021

FICHA CATALOGRÁFICA
Preparada pelo Serviço de Biblioteca e Informação
do Instituto de Física da Universidade de São Paulo

Motta, Pablo Cesar Benevides de Carvalho Rossas

Projeto BINGO: vínculos cosmológicos a partir de simulações de mapas de intensidade de HI. São Paulo, 2021.

Dissertação (Mestrado) – Universidade de São Paulo. Instituto de Física. Depto. de Física Geral

Orientador: Prof. Dr. Elcio Abdalla
Área de Concentração: Física

Unitermos: 1. Cosmologia; 2. Linha 21cm do hidrogênio; 3. Método de Monte Carlo.

USP/IF/SBI-059/2021

University of São Paulo
Physics Institute

The BINGO project: Cosmological constraints from simulated HI intensity maps

Pablo César Benevides de Carvalho Rossas Motta

Supervisor: Prof. Dr. Elcio Abdalla

Dissertation submitted to the Physics Institute of the
University of São Paulo in partial fulfillment of the
requirements for the degree of Master of Science.

Examining Committee:

Prof. Dr. Elcio Abdalla - Supervisor (IFUSP)
Prof. Dr. Daniel Augusto Turolla Vanzela (IFSC USP)
Prof. Dr. Alberto Vazquez Saa (UNICAMP)

São Paulo
2021

Abstract

One of the main cosmological challenges today is to explain dark energy. A recent project which aims to understand dark energy properties is BINGO (Baryon Acoustic Oscillations from Integrated Neutral Gas Observation). BINGO is an IM instrument designed to measure BAO in the radio band, in the frequency range of 980MHz - 1260MHz ($0.13 < z < 0.45$), through the measurement of the 21cm line of emission. The optical configuration consists of two static dishes of ~ 40 m of diameter and 28 feed horns disposed in a configuration called Double-Rectangular arrangement. In this work, we use the *nested sampling* Monte Carlo method to study cosmological constraints in BINGO. Since BINGO has not released any real data yet, we use some recently published HIR4 mocks of the HI Intensity Mapping signal. The technique requires the use of objects such as the *mixing matrix*, which mainly contains information on the BINGO observation area, and the *covariance matrix*, that relates to the statistical uncertainties. We provide a large discussion on these topics, as well as on the angular power spectrum formalism. The covariance matrix is computed through FLASK lognormal simulations, and we compare it to a theoretical model. We do not take into account any noise or foreground removal. We placed constraints separately on three redshift bins (from a total of 30) over the BINGO range, and we combined them through a Planck likelihood. We have successfully recovered the fiducial parameters, so our results seem to validate the HIR4 mocks. The next step will be to extend this analysis to the 30 BINGO bins all together. This task involves a high computational cost, so a large computer cluster is required.

Keywords: Cosmology, BINGO, angular power spectra, cosmological constraints, Monte Carlo, nested sampling, parameter estimation, 21cm, HI.

Resumo

Um dos principais desafios em cosmologia é explicar a energia escura. Um dos projetos recentes voltado à entender as propriedades da energia escura é o BINGO (Oscilações Acústicas Bariônicas em Observações Integradas de Gás Neutro). BINGO é um experimento de Mapeamento de Intensidade concebido para medir Oscilações Acústicas Bariônicas na banda de rádio, na faixa de frequencia de 980MHz - 1260MHz ($0.13 < z < 0.45$). A configuração ótica consiste em dois pratos estáticos de $\sim 40\text{m}$ de diâmetro e 28 detectores dispostos em uma configuração chamada Duplo-Retangular. Neste trabalho, usamos o método de Monte Carlo *amostragem aninhada* para estudar vínculos cosmológicos no BINGO. Como ainda não há dados observacionais do BINGO, usamos as recém publicadas simulações HIR4 do sinal de Mapeamento de Intensidade. A técnica requer o uso de objetos como a *matriz mistura*, que contém principalmente a informação da área de observação do BINGO, e a *matriz de covariância*, que está relacionada às incertezas estatísticas. Nós fornecemos uma longa discussão destes tópicos, assim como do formalismo do espectro de potência angular. A matriz de covariância é calculada a partir de simulações lognormais do FLASK. Não levamos em conta nenhum ruído ou remoção de contaminantes. Nós colocamos vínculos separadamente em três bins de redshift (de um total de 30), e combinamos com a *likelihood* (função de verossimilhança) do Planck. Conseguimos recuperar com sucesso os parâmetros fiduciais, de modo que nossos resultados parecem validar a simulação HIR4. O próximo passo será estender a análise para os 30 bins de redshift do BINGO juntos. Esta tarefa envolve um alto custo computacional, sendo necessário um *cluster* de computadores.

Palavras-chave: Cosmologia, BINGO, espectro de potência angular, vínculos cosmológicos, Monte Carlo, amostragem aninhada, estimativa de parâmetros, 21cm, HI.

Acknowledgements

First, I would like to thank my supervisor Prof. Dr. Elcio Abdalla and co-supervisor Prof. Dr. Filipe Abdalla for granting me this opportunity and for their guidance in this work. I would like to thank Dr. Jiajun Zhang for the productive discussions. I am thankful to Prof. Dr. Marcos Lima for his lectures on cosmology. I also thank Alessandro Marins, for his valuable discussions and advice. Dr. Karin Fornazier and Dr. Camila Novaes also helped me in this work. I am thankful to my colleagues Jordany Melo, Rafael Ribeiro, Daniel Correia, Carlos Otobone, João Barretos and others. I would like to thank Ana Camila Esteves for proofreading the dissertation.

I am most of all thankful to my parents Evelyn and Augusto, and also my girlfriend Celeste, for their love and unconditional support. I only got this far thanks to you.

This study was financed in part by the Coordenação de Aperfeiçoamento de Pessoal de Nível Superior - Brasil (CAPES) - Finance Code 001.

Contents

Abstract	1
Resumo	2
Acknowledgements	3
List of Figures	7
List of Tables	12
List of Abbreviations	13
1 Introduction	15
1.1 Organization of the Dissertation	17
2 Cosmology Overview	18
2.1 Fundamental equations	18
2.1.1 Einstein field equation	18
2.1.2 Boltzmann equation	20
2.2 Expanding universe	22
2.2.1 FLRW metric and Friedmann equations	22
2.2.2 Equilibrium thermodynamics	24
Ultra-relativistic species	25
Non-relativistic species	27
2.2.3 Cosmological distances	28
2.3 Perturbed Universe	29
2.3.1 First order Einstein Equations	31
2.3.2 First order Boltzmann Equations	32
Photons	33
Dark Matter	37

Baryons	38
Neutrinos	38
2.4 Correlation function and power spectra	39
2.4.1 3D Correlation function	39
Higher orders	42
2.4.2 2D angular correlation function	42
2.4.3 3D power spectrum	43
Growth factor	45
Bias function	46
Primordial power spectrum	46
2.4.4 2D angular power spectrum	47
2.5 Lognormal fields	49
Lognormals in harmonic space	51
3 The BINGO experiment and optics	53
3.1 BINGO project overview	53
3.2 The optical System	55
3.2.1 Optimization of the optical plane	58
3.2.2 Beam analysis	59
The beam polarization	66
The power spectrum of the beams	67
4 Angular Power Spectra: theory, measurements and covariance	69
4.1 The theoretical APS	69
4.1.1 Projection on the sky	69
4.1.2 Redshift Space Distortion	72
4.1.3 Non-linearities	74
4.1.4 UCLCL code	74
4.2 Cut sky formalism	74
4.2.1 The projection operator	76
Properties of the projection operator	76
4.2.2 The pseudo-APS	77
Renormalization	78
4.2.3 The mixing matrix	79
Renormalization revisited	80
4.3 Pseudo-APS estimate	80

4.3.1	The pixel window function	82
4.3.2	Generalizing the estimate for fields with non-zero mean	83
4.4	Building a covariance	84
4.4.1	Lognormal covariance	86
	FLASK code description	86
4.4.2	Theoretical covariance	87
5	Cosmological parameter estimation	91
5.1	HIR4 mock description	91
	Abundance Matching	93
	Halo Occupation Distribution (HOD)	94
5.2	Parameter estimation algorithm	95
5.2.1	Bayesian statistics	95
5.2.2	UCLCL-PARAM-EST code description	96
	Pliny: a nested sampling implementation	97
5.3	Results of parameter estimation	99
6	Conclusion	112
A	Spherical Harmonics	115
A.1	Wigner 3-j Symbols	117
Bibliography		118

List of Figures

2.1	Evolution of scale factor over cosmological time in a flat universe ($\Omega_m + \Omega_\Lambda = 0$). The Friedmann equation was solved for different contributions of cosmological constant. Notice that for the $\Omega_\Lambda = 1$ universe the expansion keeps decelerating even in later times.	21
2.2	2-point correlation function for selected redshift values computed with the CAMB free source code. The orange and green lines correspond to the redshift limits of operation for the BINGO experiment. Note how the BAO peak is visible in these redshift values.	40
2.3	Matter power spectrum at selected redshift values computed with the CAMB free source code. In Fourier space, the BAO effect is manifested as wiggles around the wave number $k = 0.1 h\text{Mpc}^{-1}$. Here we show the linear (solid lines) and non-linear (dashed lines) predictions.	43
2.4	The CMB angular power spectrum computed with the free source CAMB code. T, E, B stand, respectively, for the brightness temperature, E -mode (gradient) polarization and B -mode (curl) polarization. The TT, TE, EE, BB are amplified by a factor of (1, 20, 50, 2e4) for better visualization.	47
3.1	Left: A diagram of the telescope showing the primary and secondary reflectors, as well as the structure where the horns will be located. Right: The hexagonal cage for allocating each individual horn. The horn position can be displaced by $\pm 15\text{cm}, \pm 30\text{cm}$ from the center of the cage. Source: Wuensche et al., 2021a.	54
3.2	The BINGO optical system in 3D (top) and 2D perspectives: $x = 0$ (middle left), $z = 0$ (middle right), $y = 0$ (bottom). It is displayed in blue the primary reflector (paraboloid) and in red/orange the secondary reflector (hyperboloid). The center of the optical plane is represented by a green dot in the 3D plot.	56

- 3.3 Four arrangements of detectors (horns) positioned along the optical plane. The *Rectangular arrangement* (upper left), *Double-Rectangular arrangement* (upper right), *Triple-Rectangular arrangement* (bottom left) and *Hexagonal arrangement* (bottom right). Source: (Abdalla, Marins, Motta et al., 2021). 57
- 3.4 The side lobes of BINGO’s central beam present a moiré effect due to the two-mirror configuration of the instrument (figure 3.4a). We found that this effect attenuates when integrating the beam over the frequency. Figures (3.4b) and (3.4c) show integrated beams over widths of 10 MHz and 20 MHz respectively, computed in the ranges of 1105 – 1115 MHz and 1100 – 1120 MHz, with displacements of 1 MHz, and normalized by the number of steps. The attenuation effect is also clearer in fig. (3.4d), that portrays a 1-dimensional cut of those three results combined. 60
- 3.5 We present here the optical aberrations for the final beams of the horns located at different places within the focal plane. The focus of the telescope is placed at –15 DEC and has a beam which is devoid of aberrations, while the aberrations are increasingly large as we move away from the focal center of the telescope (we note here that the focal plane chosen in all configurations has a focus at –15 DEC, but given its asymmetry, the center of the focal plane is always at a lower declination). We can see, however, that the peak of the beam is relatively well maintained in this range of locations chosen, and that the aberrations remain at a level around 30 dB below that of the main beam. This gives us confidence that the optical aberrations within the field-of-view chosen by this work can be well modelled when the final survey is produced. 61
- 3.6 (3.6a), (3.6b), (3.6c), (3.6d): Beam responses (intensities) for, respectively, the Triple-Rectangular, Double-Rectangular, Rectangular and Hexagonal arrangements, normalized by the intensity of the central horn (see Eq. (3.11)). Fig. (3.6e): Response function of the beams, integrated in RA, for selected columns (corresponding to a declination range) and different horn arrangements. Results are normalized to the response of the central horn, according to Eq. (3.12). For the Triple-Rectangular and Double-Rectangular arrangements, the beam average also took into account the five displacements of 0, $\pm 15\text{cm}$, $\pm 30\text{cm}$. For the Rectangular arrangement, the five displacements were 0, $\pm 21\text{cm}$, $\pm 42\text{cm}$ 62

3.7	The Stokes parameters I, Q, U, V summed over for the beams of the Double-Rectangular arrangement, and transformed into dB units, i.e. $X_{dB} = 10 \log_{10}(\pm X)$. The two color bars indicate the positive (red) and negative (blue) values for the Q, U and V parameters. Each beam was previously averaged between the responses of each linearly polarized state.	63
3.8	A one-dimensional cut of the Stokes parameters presented in Fig. (3.7) for the Double-Rectangular arrangement. The cut is over $RA = RA_{peak}$, where RA_{peak} is the coordinate of the peak intensity. We see that V is at least 25 dB lower than I on the peaks, while Q and U are even lower.	64
3.9	Auto angular power spectra for the Double-Rectangular arrangement beams. Low frequency beams reach low values in the spectra for high ℓ . Since we have previously normalized the intensity, the spectra is adimensional.	67
4.1	Angular Power Spectrum computed with the UCLCL code of the HI IM temperature for the lowest, an intermediate one, and the highest redshift bins for the BINGO setting: 30 channels of $\Delta\nu = 10\text{MHz}$ in the range of 960MHz to 1260MHz. We account both RSD and non-linear effects.	70
4.2	Angular Power Spectrum computed with UCLCL code for the HI IM temperature with $\Delta\nu = 10\text{MHz}$ centered at 1115MHz. We show three cases: linear, linear accounting for RSD, and non-linear accounting for RSD. The effect of the RSD is an increase of the APS in low ℓ and the effect of non-linearities is a decrease of the APS in high ℓ	72
4.3	Mask for the BINGO experiment. Since the galaxy is a source of contamination, it also takes into account the location of the galaxy, in addition to the observation coverage itself. The mask is also apodized in the borders in order to avoid optical effects in the pixels at the border of the survey, due the wave nature of light.	75
4.4	Mixing matrix computed for a binary BINGO mask. On the upper left and right we show 2D plots in different ℓ ranges, while on the bottom, 1D cuts of the matrix are shown.	78
4.5	Comparison between theoretical (pseudo) APS and the measured (pseudo) APS estimate. The full sky theoretical one corresponds to the dashed line of figure (4.2) and the partial sky theoretical one was convolved with the mixing matrix shown in figure (4.4). The estimates were computed with the PseudoPower code on simulations created with the FLASK code.	81

4.6	The pixel window function squared for some values of Nside, computed with HEALPIX library. It decreases more quickly for lower resolutions.	82
4.7	This figure shows the consistency of the FLASK simulations with respect to the theoretical pseudo-APS and to the theoretical covariance for one of the BINGO channels (965MHZ). Upper left: In blue, average and variance (error-bars) of 500 FLASK simulations. The error bars are given by the variance $\sigma(\ell) = \sqrt{\Sigma_{\ell\ell}}$. In yellow, one of those simulations, and in black, the theoretical UCLCL convolved with the BINGO mixing matrix. Lower left: comparison between FLASK variance and theoretical variance. Upper right: the FLASK covariance. Lower right: the theoretical covariance.	85
5.1	Top: HIR4 mock for one of the BINGO channels, $\nu = 965\text{MHz}$, $\Delta\nu = 10\text{MHz}$, computed for the HOD distribution. Bottom: The same situation, but after convolving with a Gaussian kernel FWHM = 40 arcmin, in order to mimic the BINGO beam.	92
5.2	Left: Comparison between the APS estimate from the HOD mock and the theoretical UCLCL in linear and non-linear theory. We show the spectra for three frequencies: 1255MHz, 1115MHz, and 965MHz, which are amplified by 2, 1, and 0.5, respectively, for better visualization. Lower frequencies have a larger range of multipoles in the linear regime and, therefore, greater agreement between theory and data. Right: 5% and 10% of discrepancy between linear and non-linear UCLCL computations. These values were used to define the multipole range for the Monte Carlo analysis.	99
5.3	The (red) contours obtained using the HIR4 HOD mock spectrum as data vector and the covariance from FLASK are compared to (green) contours obtained using the same data vector but with the theoretical covariance implemented as explained in the text, and also to a fully theoretical description (in blue), where the data vector is also theoretical. The similarity of the contours shows the consistency of the methods. All three cases correspond to a redshift bin of 10MHz centered at 965MHz, and bandwidth of $\Delta\ell = 11$	100
5.4	Comparison of cosmological constraints for different $\Delta\ell$ values. We are using the spectrum of the HIR4 HOD mock in the redshift bin centered at 965MHz and the FLASK covariance. The contours for different $\Delta\ell$ are very consistent.	101

5.5	Comparison of cosmological constraints for different redshift bins. We are fitting the HIR4 HOD mock for the redshift bins centered at 1255MHz, 1115MHz and 965MHz, respectively, using a FLASK covariance and a bandwidth binning of $\Delta\ell = 11$. The constraints are stronger for lower frequency (higher redshift) due to the larger ℓ_{max} .	102
5.6	Comparison of cosmological constraints for the Planck 2015 data and a theoretical CMB likelihood defined at fiducial cosmology given by the WMAP5 results. Notice that the contours do not overlap for most of the parameters.	103
5.7	Comparison of cosmological constraints for BINGO 965MHz alone, BINGO 965MHz combined with Planck 2015 data, BINGO 965MHz combined with theoretical CMB likelihood. In all cases, it was used HIR4 HOD mock, FLASK covariance, and a bandwidth binning of $\Delta\ell = 11$. When combining with CMB (either Planck 2015 or theoretical), the constraints in $\Omega_{HI}b_{HI}$ are much stronger due to the measurement of the Ω_{cdm} . When using theoretical CMB likelihood, the constraint in $\Omega_{HI}b_{HI}$ is shifted in the direction of the correct value.	104
5.8	Comparison of cosmological constraints for BINGO 965MHz + CMB, BINGO 1115MHz + CMB, BINGO 1255MHz + CMB, where CMB stands for the theoretical CMB likelihood with fiducial cosmology according to WMAP5. We are using the HIR4 mock spectrum and the FLASK covariance with a bandwidth binning of $\Delta\ell = 11$. $\Omega_{HI}b_{HI}$ presents better constraints in all cases compared to BINGO alone. Also, the constraints are stronger for lower frequencies (higher redshift). The bias (b_{HI}) parameter, on the other hand, is not constrained even with CMB.	105
5.9	Constraints for six parameters of Λ CDM model plus two parameters of HI history. We compare the contours obtained for BINGO 965MHz + CMB, BINGO 1115MHz + CMB, BINGO 1255MHz and CMB alone. The data vectors, covariance and bandwidth binning are the same as in figure (5.8). We did not find a significant improvement compared to CMB alone.	106
A.1	The absolute values of Spherical Harmonics for $\ell = 0, 1, 2, 3$. Each colour represents a non-negative m value, i.e.: blue, orange, green and red stands for $m = 0, 1, 2, 3$, respectively. (The multipoles with $m < 0$ are not portrayed due to the simmetry propriety $Y_{\ell-m} = Y_{\ell m}^*$).	116

List of Tables

5.1	Prior range for the samplings. The line divides the parameters that were not used in all the jobs.	109
5.2	Recovered parameters from Planck 2015 and theoretical CMB likelihood. They correspond to the contours of fig. (5.6)	109
5.3	Recovered parameters and 68% level of confidence for Monte Carlo analysis done with limited number of free parameters: Ω_{cdm} , b_{HI} , $\Omega_{HI}b_{HI}$. Each sub-table corresponds to the set of contours portrayed in figures (5.4, 5.5, 5.7, 5.8), respectively.	110
5.4	Recovered parameters and 68% level of confidence for six Λ CDM parameters plus b_{HI} and $\Omega_{HI}b_{HI}$. We compare three frequencies combined with CMB and CMB alone. They correspond to the contours of Fig. (5.9).	111

List of Abbreviations

2PACF	2-Point Angular Correlation Function
APS	Angular Power Spectrum
BAO	Baryon Acoustic Oscillations
BINGO	Baryon Acoustic Oscillations from Integrated Neutral Gas Observation
BE	Bose-Einstein
CAMB	Code for Anisotropies in the Microwave Background
CDM	Cold Dark Matter
CLASS	Cosmic Linear Anisotropy Solving System
CMB	Cosmic Microwave Background
CNB	Cosmic Neutrino Background
DE	Dark Energy
DM	Dark Matter
EFE	Einstein Field Equations
EM	Electromagnetism/Electromagnetic
EoS	Equation-of-State
FD	Fermi-Dirac
FoV	Field-of-View
FLASK	Full-sky Lognormal Astro-fields Simulation Kit
FRB	Fast Radio Bursts
HAM	Halo Abundance Matching
HEALPix	Hierarchical Equal Area isoLatitude Pixelation
HI	neutral Hydrogen
HIR4	Horizon-Run 4 mocks populated with neutral Hydrogen
HOD	Halo Occupation Distribution
IM	Intensity Mapping
LHS	Left-Hand Side
LSS	Large Scale Structure
MCMC	Monte Carlo Markov Chain

PDE	Partial Differential Equation
RHS	Right-Hand Side
RSD	Redshift Space Distortion
UCLCL	Unified Cosmological Library for C_ℓ
UCLCL-Param-est	Unified Cosmological Library for C_ℓ -Parameter-Estimation
WMAP	Wilkinson Microwave Anisotropy Probe

Chapter 1

Introduction

Until the late 90s, the common belief was that the universe was expanding at a decelerated rate due to gravitational attraction. This changed after observations of Type Ia supernovae suggested the opposite: the expansion is accelerated! (Perlmutter et al., 1999; Riess et al., 1998). The physics Nobel prize of 2011 was dedicated to the authors of this discovery. The accelerated expansion implies that most of the energy of the universe is some sort of dark energy with a ratio of pressure to density of less than $-1/3$. So far, this phenomenon has been confirmed by several independent observations: Cosmic Microwave Background anisotropies, large-scale structures, Baryon Acoustic Oscillations, etc. However, until now, the fundamental nature of Dark Energy is still unknown. Several candidates have been proposed, the simplest of them being the cosmological constant.

Dark Energy corresponds to about 70% of the present energy fraction of the universe. The second most common component is Dark Matter ($\sim 25\%$). It distinguishes from baryonic (visible) matter by the fact that it does not interact with light. Although it has not been directly detected yet, its existence is mainly inferred by its gravitational effect on visible matter. The first evidence came in the 1930s, when Zwicky (Zwicky, 1933) studied the motion of galaxies of the Coma cluster and concluded that the velocity dispersion could not be described by visible matter only. Today, several other evidences support the existence of Dark Matter, however its origin is still unknown. There are a few candidates of Dark Matter. Some of them are astrophysical, e.g. black holes, neutron stars and white dwarfs, but they cannot explain all Dark Matter. The most part of Dark Matter should be made of some unknown particle yet to be discovered. Some examples are axions and Weakly Interacting Massive Particles (WIMPs, including neutralinos).

Besides Dark Energy and Dark Matter, the remaining components of the cosmic budget are baryonic matter ($\sim 5\%$) and radiation (less than 0.005%). Baryonic matter refers to all visible matter of the universe, responsible for forming (for example) galaxies, stars and diffuse gas of the present universe. The term "baryon" in cosmology is used more loosely than in particle physics. Here, it includes protons, neutrons and also electrons, although electrons are actually

leptons. In fact, since electrons have a small mass, they correspond to a negligible energy fraction of the total visible matter, which makes this choice of name reasonable. Baryons coupled with photons in the early universe and formed a single primordial plasma. This coupling was responsible for the Baryon Acoustic Oscillations (BAO), which left an imprint on the large scale structure we observe today.

The last component of our energy budget is radiation, which includes both photons and relativistic neutrinos. When photons decoupled from the plasma they originated the Cosmic Microwave Background (CMB) radiation. This moment of time is called recombination. Since then, the CMB photons have been travelling through the universe without interaction. This radiation can actually be detected, which provides a good snapshot of the universe at that time. Some experiments have been developed to measure CMB anisotropies, the most remarkable ones being the Wilkinson Microwave Anisotropy Probe (WMAP) (Dunkley et al., 2009), operated by NASA, and the Planck spacecraft (Adam et al., 2016), operated by the European Space Agency (ESA). Both experiments provided precise constraints on the cosmological parameters. The neutrinos decoupled earlier from the plasma and originated the Cosmic Neutrino Background (CNB). However, neutrinos are notoriously difficult to detect, so CNB has not been directly observed so far.

The current standard cosmological model is the Λ CDM, with Λ representing the cosmological constant and CDM the cold dark matter. Dark matter can be classified as "cold", "warm", or "hot" according to its velocity. Several independent measurements point to the fact that dark matter has to be "cold" (non-relativistic), otherwise the structures would not have the form we observe today. Extensions of this model would include other theoretical scenarios for dark energy such as quintessence, k-essence and perfect fluid models, dark energy interacting with dark matter, and even modified gravity models. In order to know which of these models is correct, we need to place constraints by using large observational data and hard data analysis. The CMB spectrum alone is not sufficient to place strong constraints on dark energy, and one should combine Large Scale Structure (LSS) data to the analysis, in particular at low redshift, where dark energy plays a bigger role in the cosmic evolution.

The standard approach to probe LSS is through large galaxy-redshift surveys. Over the past decades, several redshift surveys have been developed to sample the spatial distribution of extragalactic objects. Some examples are the Baryon Oscillation Spectroscopic Survey (BOSS) (Dawson et al., 2012), Dark Energy Survey (DES) (Abbott et al., 2016), and Dark Energy Spectroscopic Instrument (DESI) (Levi et al., 2013). Galaxies are used as tracers of the total matter, which is mostly dark. These surveys are then able to show the particular pattern in which matter is distributed in cosmological scales, which is believed to be the result of the evolution of

primordial perturbations on the early quasi-homogeneous and isotropic universe under the effect of gravity. Another method for probing LSS is the Intensity Mapping (IM) technique, which is less expensive and more efficient. Instead of measuring individual galaxies, IM measures the total flux from many galaxies which will underline matter. In its most common variant, 21cm Intensity Mapping, the 21cm line of emission of the neutral hydrogen is used as tracer of matter. This is the case of the BAO from Integrated Neutral Gas Observations (BINGO) experiment (Abdalla, Ferreira et al., 2021), which is projected, among other things, to measure BAO in the radio band. There are three main reasons to use IM instead of galaxy surveys: i) a larger volume of the universe can be surveyed in less time, ii) the redshift is measured directly from the redshifted 21cm line, iii) the whole signal is recorded, including the gas inbetween galaxies (Olivari, 2018).

In order to extract cosmological information from the data, one needs appropriate statistical methods. 2-point statistics is an essential tool in the analysis of the large scale structure. In particular, the angular power spectrum (APS), the 2-point correlator in Harmonic space, is one of the most used tools to describe fluctuations on the density or temperature field. In this work, we apply the APS to the 21cm temperature projected in thin spherical shells, which correspond to the redshift bin (channels) of the BINGO experiment. These measurements are compared to the theoretical prediction that comes from the solutions of the Einstein-Boltzmann equations. This formalism requires the use of the mixing matrix, that encodes the information of the observation area, and of the covariance matrix, which encodes the uncertainties of the observables. All these objects are used together in an appropriate Monte Carlo method for sampling and placement of constraints on the cosmological parameters.

1.1 Organization of the Dissertation

This dissertation is organized as follows: In chapter 2, I give an overview of cosmology, including topics such as Friedman equations, Einstein-Boltzmann equations and correlation functions. In chapter 3, I introduce the BINGO project, with emphasis on the instrumental aspects, in particular the simulation of the optical plane, based on (Abdalla, Marins, Motta et al., 2021). In chapter 4, I give a more technical description of the APS theory, APS estimate, mixing matrix and covariance building. This description is more technical, and with emphasis on how these equations are implemented in the codes. In chapter 5, I first introduce the HI mocks developed in (Zhang, Motta, Novaes et al., 2021), then I explain the Monte Carlo algorithm of nested sampling in the results of cosmological parameter estimations. In chapter 6, I give the conclusions and final remarks of this dissertation and expectations for future works.

Chapter 2

Cosmology Overview

In this chapter, we aim to introduce to the reader all the main concepts in physical cosmology which are necessary for the understanding of this work. We start by introducing the fundamental equations of cosmology: the Einstein field equation and the Boltzmann equation. Then, we explore the cosmic expansion in the homogeneous and isotropic universe, and topics such as thermodynamics and cosmological distances. Finally, we formulate the equations that describe the evolution of perturbations in the universe, and define the main statistical correlators. Here, we use the convention of $\hbar = k_B = c = 1$, where \hbar is the reduced Planck constant, k_B is the Boltzmann constant and c is the speed of light in the vacuum.

2.1 Fundamental equations

The Einstein field equation of general relativity describes gravity as a result of spacetime being curved due to the energy within it. The Boltzmann equation describes the statistical mechanics of each component of the energy budget. Since cosmology is essentially the application of the Einstein and Boltzmann equations coupled, we formulate both of them in this section.

2.1.1 Einstein field equation

Gravity is the only fundamental force of nature with the property of universality: the trajectory of a free falling body depends only on its position and initial speed and not on its mass or any intrinsic property of the body. This allows gravity to be described geometrically as a deformation or curvature of spacetime due to the presence of mass or energy. Mathematically, the spacetime geometry is represented by the metric tensor $g_{\mu\nu}(\mathbf{x}, t)$, given by

$$ds^2 = g_{\mu\nu} dx^\mu dx^\nu. \quad (2.1)$$

As in special relativity, the interval ds^2 is a scalar invariant and it can be either positive (space-like), negative (time-like) or null, which characterizes the causal structure of spacetime. Minkowski metric $\eta_{\mu\nu} = \text{diag}(-1, 1, 1, 1)$ is the particular case of flat spacetime (absence of gravity). A curved spacetime means presence of gravity, and $g_{\mu\nu}(\mathbf{x}, t)$ assumes a more general form, which should be a solution for the Einstein field equations. The Minkowski metric (and the Poincaré symmetry) are required to be valid only locally. This means that there is always a *local* coordinate transformation to the Minkowski metric, and Minkowski spacetime can be seen as a tangent space to the manifold.

The Einstein field equations are a set of second order non-linear partial differential equations (PDEs) for the $g_{\mu\nu}(\mathbf{x}, t)$ field. In order to enunciate them, we define the following geometric objects,

$$\Gamma_{\nu\lambda}^\mu = \frac{1}{2} g^{\mu\alpha} (g_{\alpha\nu,\lambda} + g_{\alpha\lambda,\nu} - g_{\nu\lambda,\alpha}) , \quad (2.2)$$

$$R_{\mu\nu} = \Gamma_{\mu\nu,\alpha}^\alpha - \Gamma_{\mu\alpha,\nu}^\alpha + \Gamma_{\mu\nu}^\alpha \Gamma_{\alpha\beta}^\beta - \Gamma_{\mu\beta}^\alpha \Gamma_{\alpha\nu}^\beta , \quad (2.3)$$

$$R = g^{\mu\nu} R_{\mu\nu} , \quad (2.4)$$

$$G_{\mu\nu} = R_{\mu\nu} - \frac{1}{2} g_{\mu\nu} R , \quad (2.5)$$

namely the Christoffel symbol, the Ricci tensor, the Ricci scalar and the Einstein tensor, respectively. Thus, the Einstein field equations (EFE) read

$$G_{\mu\nu} = 8\pi G T_{\mu\nu} . \quad (2.6)$$

While in Newtonian gravity, $\nabla^2\psi = 4\pi G\rho$, only the mass density ρ is source of the gravitational potential ψ , in Einstein's theory all the components of the energy-momentum tensor $T_{\mu\nu}$ are required. Notice that G is the Newtonian constant, and Eq. (2.6) reduces to Newton's law in the limit of weak gravitational field and low velocities (see e.g. Rindler, 2012 or Carroll, 2019). Moreover, since $T_{\mu\nu}$ (and $G_{\mu\nu}$) are symmetric, Eq. (2.6) corresponds to a system of 10 independent PDEs. Also, the symmetries of a given problem can introduce constraints which reduce the number of independent equations. In summary, EFE relates density and flux of energy and momentum ($T_{\mu\nu}$) to spacetime geometry ($G_{\mu\nu}$). As in the case of Maxwell equations, solving the PDEs requires taking into account all the symmetries of the problem, as well as boundary conditions. In the next section we apply them to the cosmological scenario. First, we present the zeroth-order equations describing the homogeneous and isotropic universe, and then we explore the first-order equations, which describe the evolution of the perturbations.

2.1.2 Boltzmann equation

While the EFE describe gravity, the Boltzmann equation is fundamental for describing matter and radiation. In cosmology, we are interested in the statistical properties rather than in individual particles. Therefore, we work with the probability distribution function for each species of particles. The function is described on the 6-dimensional *phase space* (\mathbf{x}, \mathbf{p}) , each point representing a possible state of the particle in terms of its position \mathbf{x} and momentum \mathbf{p} . If the number of particles is large enough, we can define the distribution function such that (in $\hbar = c = 1$ units)

$$dN_s = f_s(\mathbf{x}, \mathbf{p}, t) \frac{d^3\mathbf{x} d^3\mathbf{p}}{(2\pi)^3} \quad (2.7)$$

is the number of particles of the species s at a given time t in the given infinitesimal volume of the phase space. The Boltzmann equation describes the dynamics of the distribution function

$$\frac{df_s}{dt} = \frac{\partial f_s}{\partial t} + \frac{dx^i}{dt} \frac{\partial f_s}{\partial x^i} + \frac{dp}{dt} \frac{\partial f_s}{\partial p} + \frac{dp^i}{dt} \frac{\partial f_s}{\partial p^i} = C[f_s]. \quad (2.8)$$

The RHS is the *collision term*. When $C[f_s] = 0$ (collisionless case), the Boltzmann equation implies conservation of particles. The collision can be any kind of interaction among particles, such as scattering, pair creation, annihilation, and particle decay. For the sake of formulating the collision term, let us assume a very common process

$$(1)_\mathbf{p} + (2)_\mathbf{q} \leftrightarrow (3)_\mathbf{p}' + (4)_\mathbf{q}', \quad (2.9)$$

where we have two particles with momenta \mathbf{p} and \mathbf{q} resulting in two particles with momenta \mathbf{p}' and \mathbf{q}' . The collision term reads (Dodelson and Schmidt, 2020)

$$\begin{aligned} C[f_1(\mathbf{p})] &= \frac{1}{2E_1(p)} \int \frac{d^3\mathbf{q}}{(2\pi)^3 2E_2(q)} \int \frac{d^3\mathbf{p}'}{(2\pi)^3 2E_3(p')} \int \frac{d^3\mathbf{q}'}{(2\pi)^3 2E_4(q')} |\mathcal{M}|^2 \\ &\times (2\pi)^4 \delta_D^{(3)}(\mathbf{p} + \mathbf{q} - \mathbf{p}' - \mathbf{q}') \delta_D^{(1)}(E_1(p) + E_2(q) - E_3(p') - E_4(q')) \\ &\times [f_3(p') f_4(q') (1 \pm f_1(\mathbf{p})) (1 \pm f_2(\mathbf{q})) - f_1(\mathbf{p}) f_2(\mathbf{q}) (1 \pm f_3(\mathbf{p}')) (1 \pm f_4(\mathbf{q}'))], \end{aligned} \quad (2.10)$$

where $E_s(p) = \sqrt(m_s^2 + p^2)$. The collision depends on the product of distribution functions $f_1 f_2$ (forward reaction) and $f_3 f_4$ (reverse reaction). Also, the $(1 \pm f_s)$ terms are corrections due to the quantum effects of Bose enhancement (+) and Pauli exclusion principle (-), which we

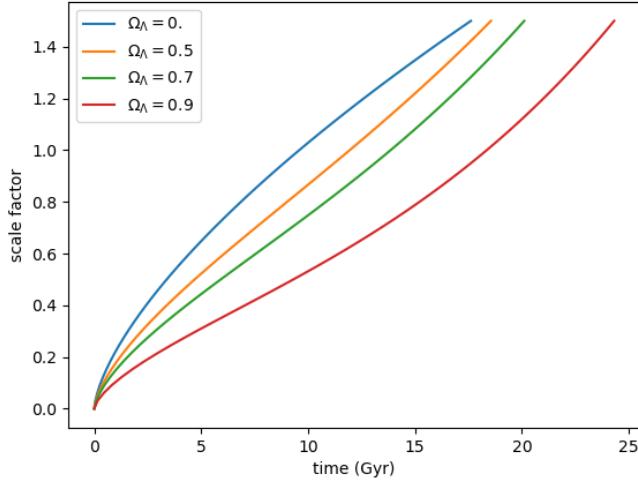


FIGURE 2.1: Evolution of scale factor over cosmological time in a flat universe ($\Omega_m + \Omega_\Lambda = 0$). The Friedmann equation was solved for different contributions of cosmological constant. Notice that for the $\Omega_\Lambda = 1$ universe the expansion keeps decelerating even in later times.

are going to neglect in the subsequent sections. Note that the Dirac delta functions enforce momentum and energy conservation. All the microphysical details of the interaction are encoded in the amplitude squared $|\mathcal{M}|^2$. Equation (2.10) can be easily generalized for a higher number of particles.

Furthermore, the distribution function helps us know what to put in the RHS of the EFE. It can be shown that the energy–momentum tensor for a given distribution can be expressed as (Dodelson and Schmidt, 2020)

$$T^\mu_\nu(\mathbf{x}, t)_s = \frac{g_s}{\sqrt{-g}} \int \frac{dP_1 dP_2 dP_3}{(2\pi)^3} \frac{P^\mu P_\nu}{P^0} f_s(\mathbf{x}, \mathbf{p}, t). \quad (2.11)$$

We denote by g_s the species degeneracy factor, by g the determinant of the metric tensor and by P^μ the 4-momentum. The degeneracy factor g_s counts how many different particle states are in fact described by the distribution function.

2.2 Expanding universe

2.2.1 FLRW metric and Friedmann equations

The current cosmological model is based on the idea that the universe is homogeneous, i.e. it looks the same in its whole extension (Copernican principle) and is isotropic, i.e. it is the same in all directions. These assumptions are made only on very large scales, where one takes the average of local variations in density. Its validity has been confirmed systematically over several observations, such as number counts of galaxies, observations of diffuse radio- x and radio- γ backgrounds and mostly of CMB (Carroll, 2019). The metric that takes into account these symmetries together with the concept of expanding universe is

$$ds^2 = g_{\mu\nu}dx^\mu dx^\nu = -dt^2 + a(t)^2 d\ell^2, \quad (2.12)$$

where the *scale factor* $a(t)$ is a free parameter that describes the expansion and

$$d\ell^2 = \gamma_{ij}dx^i dx^j = \frac{dr^2}{1-Kr^2} + r^2(d\theta^2 + \sin^2\theta d\phi^2) \quad (2.13)$$

is the homogeneous and isotropic 3-dimensional space. K denotes the curvature of space. If $K > 0$, we have a closed space (3-sphere), if $K < 0$ an open space (3-hyperbola), and if $K = 0$ a flat space (3-plane). We call eq. (2.12) the FLRW (Friedmann-Robertson-Walker) metric. Under the same assumption of homogeneity and isotropy, we model the energy-momentum tensor as

$$T^\mu_\nu = \text{diag}(-\rho, \omega\rho, \omega\rho, \omega\rho), \quad (2.14)$$

where ρ denotes the energy density and $\omega\rho$ the pressure. Replacing $T_{00} = \rho$ and $T_{ij}a^2\delta_{ij}\omega\rho$ together with the *ansatz* of eq. (2.12) in the EFE (2.6) results in two independent Einstein equations (00 and ij components) which we call the Friedmann equations

$$\left(\frac{\dot{a}}{a}\right)^2 = \frac{8\pi G}{3}\rho - \frac{K}{a^2}, \quad (2.15)$$

$$\frac{\ddot{a}}{a} = -\frac{4\pi G}{3}\rho(1+3\omega). \quad (2.16)$$

Next, we define the Hubble function as

$$H(t) = \frac{\dot{a}(t)}{a(t)}. \quad (2.17)$$

It represents the expansion rate of the universe. Let us define the *critical density* as the energy density for a flat ($K = 0$) universe. From eq. (2.15), it is given by

$$\rho_{\text{crit}}(t) = \frac{3H(t)^2}{8\pi G}. \quad (2.18)$$

Also notice that if $\rho > \rho_{\text{crit}}$, the universe is closed, and if $\rho < \rho_{\text{crit}}$, the universe is open. Furthermore, the curvature of space depends on what is the total energy density of the universe. However, the observations point towards a flat universe, which requires a very fine tuning of the density to the critical value. This is called the *flatness problem*.

Equation (2.15) can be rewritten as

$$H(t)^2 = \frac{8\pi G}{3} \sum_s \rho_s(t), \quad (2.19)$$

where the sum is over the components of the universe: radiation, matter, dark energy and curvature. For the latter we define an effective density given by

$$\rho_K(t) = -\frac{3K}{8\pi G a^2}. \quad (2.20)$$

However, each component evolves differently over time. As we shall see, it depends on the ratio ω between the pressure and the energy density of each species, also called equation-of-state (EoS) parameter. To see that, let us take the $\nu = 0$ component of the energy-momentum conservation $\nabla_\mu T^{\mu\nu} = 0$. It gives us the following continuity equation

$$\frac{d\rho}{dt} + 3H(1+\omega)\rho = 0. \quad (2.21)$$

Replacing $a = (1+z)^{-1}$, we find the following exact solution

$$\rho(z) = \rho(0) \exp \left[3 \int_0^z dz' \frac{1+\omega(z')}{1+z'} \right]. \quad (2.22)$$

For $\omega = \text{constant}$, we have

$$\rho(z) = \rho(0)(1+z)^{3(1+\omega)}. \quad (2.23)$$

Then, we just have to replace the accurate ω for each species. The (non-relativistic) matter has $\omega_m = 0$, since their momentum is negligible compared to the density. For curvature, as $\rho_K \sim a^{-2}$, we have an effective $\omega_K = -1/3$. For radiation, we have $\omega_r = 1/3$. This can be seen from the fact that the EM energy-momentum has zero trace (Motta, 2018), so its EoS parameter can be derived from eq. (2.21). Alternatively, we can prove this from the distribution function of the ultra-relativistic species as we shall see later. The dark energy EoS parameter depends on the dark energy model and it could also be a dynamical quantity. From eq. (2.16), it should satisfy $\omega_{DE} < -1/3$ in later times, so the expansion is accelerated in the dark energy dominated universe. The most standard candidate for dark energy is the cosmological constant, a vacuum energy given by $T_{\mu\nu} = \Lambda$. That scenario yields a EoS parameter of $\omega_\Lambda = -1$. Assuming a constant ω_{DE} , let us replace the EoS parameter of each species in eq. (2.19). The first Friedmann equation reads

$$E(z)^2 = \frac{H(z)^2}{H_0^2} = \sum_s \frac{\rho_s(0)}{\rho_{\text{crit}}(0)} (1+z)^{3(1+\omega_s)} \quad (2.24)$$

$$= \Omega_K(1+z)^2 + \Omega_m(1+z)^3 + \Omega_r(1+z)^4 + \Omega_{DE}(1+z)^{3(1+\omega_{DE})}, \quad (2.25)$$

where the Ω_s represents the ratios with respect to the critical density today ($z = 0$). Also, H_0 is the Hubble function today, called Hubble constant. It has unities of velocity per distance usually expressed in $(\text{Km/s}) \text{Mps}^{-1}$. However, it can also be parametrized in terms of a dimensionless Hubble constant h , given by $H_0 = 100 h / [(\text{Km/s}) \text{Mps}^{-1}]$. In figure (2.1) we solve the Friedmann equation (2.25) for a flat universe ($\Omega_m + \Omega_\Lambda = 1$) and $h = 0.68$. We choose some different $(\Omega_m, \Omega_\Lambda)$ values to show the impact in the scale factor evolution. The higher the dark energy density, the faster the evolution and the earlier the inflection point to the accelerated expanding universe. In the universe with only matter ($\Omega_\Lambda = 0$), the inflection point never happens, so the universe keeps decelerating in later times.

2.2.2 Equilibrium thermodynamics

In subsection 2.1.2 we defined the distribution function and explained that it is an important tool to tackle the statistical properties of matter and radiation. In subsection 2.2.1 we described our universe with the help of some macroscopic quantities, energy density and pressure, to

describe each species. The distribution function allows one to link microscopic to macroscopic quantities. For instance, the number density, energy density and pressure are (Kolb, 2018)

$$n_s(\mathbf{x}, t) = g_s \int \frac{d^3 p}{(2\pi)^3} f_s(\mathbf{x}, \mathbf{p}, t), \quad (2.26)$$

$$\rho_s(\mathbf{x}, t) = g_s \int \frac{d^3 p}{(2\pi)^3} E_s f_s(\mathbf{x}, \mathbf{p}, t), \quad (2.27)$$

$$\mathcal{P}_s(\mathbf{x}, t) = g_s \int \frac{d^3 p}{(2\pi)^3} \frac{p^2}{3E_s} f_s(\mathbf{x}, \mathbf{p}, t), \quad (2.28)$$

where $E_s(p) = \sqrt{m_s^2 + p^2}$ is the energy of the particle. The integral is therefore an average of possible states (momentum) of the particle weighted by the distribution function. We have already shown this for the energy-momentum tensor (eq. 2.11). In fact, equations (2.27) and (2.28) are components of (2.11).

In equilibrium, the distribution function follows the well known Bose-Einstein (BE) distribution (for bosons) or Fermi-Dirac (FD) distribution (for fermions),

$$f_s(\mathbf{x}, \mathbf{p}, t) = f_s(p, t) = \frac{1}{e^{(E_s - \mu_s)/T_s} \pm 1}. \quad (2.29)$$

Here, the plus sign stands for FD distribution and the minus sign for BE distribution. Also, we denote by T_s and μ_s , respectively, the temperature and the chemical potential. In the classical limit ($T_s \rightarrow \infty$), both distributions reduce to Maxwell-Boltzmann distribution:

$$f(p, t) = e^{-(E_s - \mu_s)/T_s}. \quad (2.30)$$

Ultra-relativistic species

From equations (2.26) to (2.28) and Eq. (2.29), we find that the ultra-relativistic ($p \gg m$) and non-degenerated ($T \gg \mu$) particle has

$$n_s(t) = \frac{\zeta(3)}{\pi^2} g_s T_s^3 \times \begin{cases} 1 & \text{if boson} \\ \frac{3}{4} & \text{if fermion} \end{cases} \quad (2.31)$$

$$\rho_s(t) = \frac{\pi^2}{30} g_s T_s^4 \times \begin{cases} 1 & \text{if boson} \\ \frac{7}{8} & \text{if fermion} \end{cases} \quad (2.32)$$

$$\mathcal{P}_s(t) = \frac{\rho_s(t)}{3}. \quad (2.33)$$

This result implies that the EoS parameter is $\omega_r = 1/3$ for the ultra-relativistic particle. The most important case is the photon, which is a boson with degeneracy $g_\gamma = 2$ (two spin states), and, consequently, energy density of

$$\rho_\gamma = \frac{\pi^2}{15} T_\gamma^4 . \quad (2.34)$$

It constitutes most of the radiation contribution of the cosmic energy budget in the form of Cosmic Microwave Background (CMB), a radiation emitted in the recombination epoch $z \sim 1100$. Before recombination, photons, protons and electrons were tightly coupled with each other through Compton and Coulomb scattering, constituting a single plasma in equilibrium. When the temperature of the plasma dropped the ionization energy of the hydrogen, the hydrogen atom was formed as a result of the binding of protons and electrons, which results in the emission of photons. After recombination, the CMB photons travelled freely in the universe without interacting. Therefore, the CMB observed today is a good snapshot of the universe at $z \sim 1100$ (Dodelson and Schmidt, 2020).

Another important ultra-relativistic particle is the neutrino. In opposition to the photon, neutrinos have mass, but since it is low, neutrinos behave as ultra-relativistic in the early universe. What we should know about them is this: there are three generations of neutrinos (and anti-neutrinos); each generation has one spin degree of freedom; they are fermions, and therefore follow the FD distribution in equilibrium (Dodelson and Schmidt, 2020). Putting all these together we find

$$\rho_\nu = \frac{7}{8} N_{\text{eff}} \frac{\pi^2}{15} T_\nu^4 . \quad (2.35)$$

We denote by N_{eff} the effective number of neutrino species. Although it is 3 in standard models, we can let it be a free parameter accounting for other degrees of freedom. The current standard value is $N_{\text{eff}} = 3.04$ (Mangano et al., 2002), which is slightly higher than 3. Remember that unlike photons and baryons, the cosmic neutrinos have not been directly observed yet. For convenience, we might write its density in terms of the photon density

$$\frac{\rho_\nu}{\rho_\gamma} = \frac{7}{8} N_{\text{eff}} \left(\frac{T_\nu}{T_\gamma} \right)^4 \approx 0.69 . \quad (2.36)$$

The neutrino and photon temperatures are not the same because neutrinos decoupled earlier from the plasma. Particularly, the neutrino decoupling happened slightly before the electron-positron annihilation, therefore they did not participate on the energy injection resulting from

this process. Thus, neutrinos ended up with a lower temperature than photons. This ratio is given by

$$\frac{T_\nu}{T_\gamma} = \left(\frac{4}{11} \right)^{\frac{1}{3}}, \quad (2.37)$$

which can be shown from entropy conservation (see e.g. [Dodelson and Schmidt, 2020](#); [Amendola and Tsujikawa, 2010](#)). Equation (2.36) is only true earlier in the universe, since later neutrinos became non-relativistic. However, the number density ratio

$$\frac{n_\nu}{n_\gamma} = \frac{3}{4} N_{\text{eff}} \left(\frac{T_\nu}{T_\gamma} \right)^3 = \frac{3}{11} N_{\text{eff}} \approx 0.83 \quad (2.38)$$

remains true. So, after they become non-relativistic, we can infer the energy density of each generation as

$$\rho_{\nu_i} = \frac{3}{11} m_{\nu_i} n_\gamma. \quad (2.39)$$

As well as the photons, the neutrinos keep traveling freely since the decoupling and are still present during the current epoch as Cosmic Neutrino Background (CNB). Although these neutrinos are in principle all around us, they have so far escaped detection due to their extremely small interaction cross sections ([Burgess, 2016](#)).

Non-relativistic species

In the non-relativistic limit, $p \ll m$ (or $T \ll m$), the BE and FD distributions reduce to the Boltzmann distribution and the energy of the particle goes to $E = m + p^2/2m$. Therefore, equations (2.26) to (2.28) yield

$$n_s(t) = g_s \left(\frac{m_s T_s}{2\pi} \right)^{3/2} \exp [-(m_s - \mu_s)/T_s], \quad (2.40)$$

$$\rho_s(t) = m_s n_s(t), \quad (2.41)$$

$$\mathcal{P}_s(t) = T_s(t) n_s(t) \ll \rho_s. \quad (2.42)$$

The last equation shows that $\omega_m \approx 0$, as expected. Also, unlike photons, non-relativistic matter cannot be described by the temperature only. Therefore, we need to measure the density of non-relativistic particles (baryons and dark matter) directly from observations ([Amendola and Tsujikawa, 2010](#)). Moreover, matter at the present time cannot be simply described by an

equilibrium distribution function. This is because it comes in many different phases: diffuse neutral gas and ionized plasma, stars and planets, compact objects, and so on (Dodelson and Schmidt, 2020).

2.2.3 Cosmological distances

Measuring distances in the expanding universe can be tricky, so one should be careful with the different definitions. From equation (2.12), we immediately see that we can either define distances in comoving coordinates, which remain fixed as the universe expand, or in physical coordinates, that grows as the universe expands. First, let us think in the comoving distance between a distant light source and us. Since in an interval dt the light travels a comoving distance dt/a , the total comoving distance travelled by the photon is

$$\chi(t) = \int_t^{t_0} \frac{dt'}{a(t')} = \int_{a(t)}^1 \frac{da'}{a'^2 H(a')} = \int_0^z \frac{dz'}{H(z')} . \quad (2.43)$$

The physical distance between the source and us is then $a\chi$. However, $a\chi$ is not the physical distance travelled by the photon, since it was emitted in a younger universe and the scale has increased since the emission.

Moreover, we can find the comoving distance travelled by the photon since the beginning of time ($t = 0$) in the absence of interaction by

$$\eta(t) = \int_0^t \frac{dt'}{a(t')} . \quad (2.44)$$

This is called *comoving horizon*. It represents the maximum distance (in comoving coordinates) which allows for a causal connection, since no information could have travelled a distance higher than that. Although in general we would have to compute the integral of Eq. (2.44) numerically, we can solve it analytically for simplified cases. In the radiation dominated epoch, $H \propto a^{-2}$, so we have $\eta = [aH]^{-1}$. Similarly, for the matter dominated epoch, $H \propto a^{-3/2}$, and we can find $\eta = 2[aH]^{-1}$. Then we assume that η is of the order of aH for the most part of the universe, so scales with $k \gg aH$ ($k \ll aH$) are taken as the sub-horizon (super-horizon) limit. We can also think of η as a time coordinate, which we call *conformal time*. In the literature, it is common to move back and forth between cosmic time and conformal time, because it can simplify the equations.

Furthermore, we are also interested in transversal distances. Notice that the comoving distance given by Eq. (2.43) is defined with respect to the observer, and therefore it is also a radial

distance. We can then write the spatial metric as

$$d\ell^2 = d\chi^2 + r^2 d\Omega^2. \quad (2.45)$$

The comoving transversal distance is then given by $r\Delta\Omega$. It is common in astronomy for the transverse distance to be inferred from the angular separation $\Delta\Omega$ between objects. r is the comoving angular diameter distance and it is not equal to χ in a curved space. By equating (2.13) and (2.45), we can find

$$\chi = \int \frac{dr^2}{\sqrt{1 - Kr^2}} = \frac{\sin^{-1}(\sqrt{K}r)}{\sqrt{K}}. \quad (2.46)$$

Solving for r

$$r = \frac{\sin(\sqrt{K}\chi)}{\sqrt{K}}. \quad (2.47)$$

The angular diameter distance is usually expressed as a physical rather than a comoving distance. We multiply eq. (2.47) by the scale factor, getting the following expression that is found in the literature (Dodelson and Schmidt, 2020; Weinberg, 2008; Hogg, 1999)

$$d_A = ar = a \frac{\sin(\sqrt{K}\chi)}{\sqrt{K}} = a \frac{\sin(\sqrt{-\Omega_K}H_0\chi)}{H_0\sqrt{-\Omega_K}}, \quad (2.48)$$

where the last equation comes from equations (2.18), (2.19) and (2.20). In the case of $K = 0$,

$$d_A = a\chi \quad (2.49)$$

2.3 Perturbed Universe

We have so far discussed the universe under the assumptions of homogeneity and isotropy. Although this is true for sufficiently large scales $\sim 100\text{Mpc}$, the universe is clearly neither homogeneous nor isotropic in small scales. Deviations from smoothness, i.e. inhomogeneities or structures, constitute an important source of cosmological information which has been systematically analyzed from either CMB or LSS. Perturbations in matter at scales lower than $\sim 10\text{Mpc}$ have become large in the late universe, and therefore nonlinear. On the other hand, perturbations in scales higher than $\sim 10\text{Mpc}$ are still small enough to be described by linear

perturbation theory, which is the focus of this section. Similarly, the CMB anisotropies are small since they were produced in an early quasi-smooth universe.

Let us start with the geometrical perturbations. The metric tensor is perturbed around the background solution, i.e. $g_{\mu\nu} = \bar{g}_{\mu\nu} + \delta g_{\mu\nu}$, where $\bar{g}_{\mu\nu}$ is the background FLRW metric (2.12), and $\delta g_{\mu\nu}$ is assumed to be small. Although in principle the metric perturbation can have generic components, we are going to assume the specific form

$$ds^2 = -(1 + 2\Psi)dt^2 + a^2(1 + 2\Phi)d\mathbf{x}^2. \quad (2.50)$$

This is because a generic perturbation can be decomposed in scalar, vector and tensor perturbations (e.g. Kurki-Suonio, 2015), which play different roles in cosmology. Scalar perturbations are the most important ones, since they are the only ones coupling with matter and are responsible for the formation of structure in the universe from small initial perturbations. Vector perturbations couple with rotational velocity and tend to decay in an expanding universe, thus becoming unimportant. Tensor perturbations are related to gravitational waves, and are relevant to characterize the polarization of photon perturbations. Equation (2.50) then includes an arbitrary scalar perturbation in the form of the gravitational potentials $\Psi, \Phi \ll 1$. From now on, we are also assuming, for simplicity, a flat background ($K = 0$ in 2.13).

We also need to include perturbations in the other components of the universe (except, in the standard model, for dark energy, which is described by a cosmological constant): dark matter, baryonic matter, photons and neutrinos. As we know, gravity couples with all components through its energy-momentum. Moreover, photons interact with baryons through Compton scattering and baryons also interact via Coulomb scattering. We should also, in principle, include perturbations for dark energy. They exist if dark energy is not a cosmological constant. However, most of the viable models predict that they should be very small and have only become relevant very recently (Dodelson and Schmidt, 2020). While the dynamics of gravity (Ψ, Φ potentials) is given by the Einstein Equations, the dynamics of the perturbations in matter and radiation is given by the Boltzmann Equations (Eq. 2.8). Since they are all coupled, we call them the Einstein-Boltzmann equations. In order to derive the first order theory, we collect all the first order terms (small fluctuations over the background) and drop the second order terms. In order to account for fluctuations in matter, we define the energy overdensity as

$$\delta_{cdm/b}(\mathbf{x}, t) = \frac{\rho_{cdm/b}(\mathbf{x}, t)}{\bar{\rho}_{cdm/b}(t)} - 1, \quad (2.51)$$

where $\bar{\rho}_{cdm/b}$ is the average energy density. We also need to take into account the velocities

$v_{cdm}, v_b \ll 1$ of dark and baryonic matter, which are first order terms since they are non-relativistic. Moreover, for photons we perform the following perturbation around equilibrium

$$\Theta(\mathbf{x}, \hat{\mathbf{p}}, t) = \frac{T_\gamma(\mathbf{x}, \hat{\mathbf{p}}, t)}{\bar{T}_\gamma(t)} - 1. \quad (2.52)$$

The photon perturbation depends not only on \mathbf{x} and t but also on the direction of the propagation $\hat{\mathbf{p}}$. It will also be helpful to transform these quantities to Fourier space and conformal time. Furthermore, the photon perturbation depends on k , η , as well as on $\mu = \hat{\mathbf{p}} \cdot \mathbf{k}$. It will also be helpful to define the ℓ th multipole moment for the photon temperature,

$$\Theta_\ell(k, \eta) = -(-1)^\ell \int_{-1}^1 \frac{d\mu}{2} P_\ell(\mu) \Theta(\mu, k, \eta), \quad (2.53)$$

where P_ℓ is the Legendre polynomial of order ℓ . Similarly, we define for neutrinos the temperature perturbation $\mathcal{N}(\mathbf{x}, \hat{\mathbf{p}}, p, t)$ and the Legendre multipole moments $\mathcal{N}_\ell(k, \eta, p)$. In contrast to the photons, neutrinos also depend on p due to the fact that they have mass. However, we can neglect this dependency at least until recombination.

2.3.1 First order Einstein Equations

We must collect all the first order terms of the Einstein tensor for the perturbed spacetime (Eq. 2.50), as well as of the energy-momentum tensor (Eq. 2.11). This results in two independent equations (00 and ij components), which in Fourier space read

$$k^2 \Phi + 3 \frac{a'}{a} \left(\Phi' - \Psi \frac{a'}{a} \right) = 4\pi G a^2 [\bar{\rho}_{cdm} \delta_{cdm} + \bar{\rho}_b \delta_b + 4\bar{\rho}_\gamma \Theta_0 + 4\bar{\rho}_\nu \mathcal{N}_0], \quad (2.54)$$

$$k^2 (\Phi + \Psi) = -32\pi G a^2 [\bar{\rho}_\gamma \Theta_2 + \bar{\rho}_\nu \mathcal{N}_2]. \quad (2.55)$$

The prime denotes derivative with respect to conformal time. Notice that the factor of 4 in the radiation components in Eq. (2.54) comes from the fact that $\rho \propto T^4$ for relativistic species. Here we are neglecting the neutrino mass. Equation (2.55) does not have any derivative in Ψ or Φ , thus it is a constraint equation. This is an important result because it states that $\Psi \approx -\Phi$, unless photons or neutrinos have an appreciable quadrupole moment.

2.3.2 First order Boltzmann Equations

We shall see how Eq. (2.8) is simplified for the particle following a geodesic in the perturbed spacetime of Eq. (2.50). We follow (Lima, 2019; Dodelson and Schmidt, 2020). First of all, we shall write the 4-momentum of the particle as $P^\mu = dx^\mu/d\lambda$, where λ is an affine parameter. In this way, we can treat both massive and non-massive particles in the same manner. We denote $p^2 = g_{ij}P^iP^j$, so, defining $E(p) = \sqrt{m^2 + p^2}$ as usual, the 4-momentum of the particle in the perturbed spacetime reads

$$P^\mu = \left[E(1 - \Psi), \mathbf{p} \frac{1 - \Phi}{a} \right]. \quad (2.56)$$

Looking at equation (2.8), our goal is to compute the coefficients dx/dt , dp/dt from equation (2.56). The term $d\hat{\mathbf{p}}/dt$ does not need to be computed, since $\partial f/\partial \hat{\mathbf{p}}$ and $d\hat{\mathbf{p}}/dt$ are both first order terms, which results in their product vanishing in the first order theory. Let us start with dx/dt . It follows from Eq. (2.56) that

$$\frac{dx^i}{dt} = \frac{dx^i}{d\lambda} \frac{d\lambda}{dt} = \frac{P^i}{P^0} = \frac{p\hat{p}^i(1 - \Phi)}{aE(1 - \Psi)} \approx \frac{p\hat{p}^i}{aE}(1 + \Psi - \Phi). \quad (2.57)$$

The term dp/dt follows from the geodesic equation,

$$\frac{dP^0}{d\lambda} = -\Gamma^0_{\alpha\beta}P^\alpha P^\beta. \quad (2.58)$$

Since the LHS can be written as

$$\begin{aligned} \frac{dP^0}{d\lambda} &= \frac{dP^0}{dt} \frac{dt}{d\lambda} = E(1 - \Psi) \frac{d}{dt}[E(1 - \Psi)] \\ &\approx E(1 - 2\Psi) \left[\frac{dE}{dt} - E \left(\frac{\partial \Psi}{\partial t} + \frac{\partial \Psi}{\partial x^i} \frac{p\hat{p}^i}{aE} \right) \right], \end{aligned} \quad (2.59)$$

we have

$$\frac{dE}{dt} = E \left(\frac{\partial \Psi}{\partial t} + \frac{\partial \Psi}{\partial x^i} \frac{p\hat{p}^i}{aE} \right) - \left(\frac{1 + 2\Psi}{E} \right) \Gamma^0_{\alpha\beta}P^\alpha P^\beta. \quad (2.60)$$

The Christoffel symbols of the perturbed spacetime (2.50) are given by

$$\begin{aligned}\Gamma^0_{00} &= \frac{\partial\Psi}{\partial t}, \quad \Gamma^0_{0i} = \frac{\partial\Psi}{\partial x^i}, \\ \Gamma^0_{ij} &= \delta_{ij}a^2 \left[H + 2H(\Phi - \Psi) + \frac{\partial\Phi}{\partial t} \right].\end{aligned}\quad (2.61)$$

Therefore, by replacing them in (2.60) we find

$$\frac{dE}{dt} = - \left(\frac{p^2}{E} \frac{\partial\Phi}{\partial t} + \frac{\partial\Psi}{\partial x^i} \frac{p\hat{p}^i}{a} + \frac{p^2 H}{E} \right). \quad (2.62)$$

Since $E(p) = \sqrt{m^2 + p^2}$, we can also write

$$\frac{dp}{dt} = -p \left[\frac{\partial\Psi}{\partial t} + \frac{\partial\Psi}{\partial x^i} \frac{E\hat{p}^i}{p} + H \right]. \quad (2.63)$$

Thus we replace equations (2.57), (2.62) and (2.63) in (2.8), and the Boltzmann equation becomes

$$\frac{df}{dt} = \frac{\partial f}{\partial t} + \frac{\hat{p}^i}{a} \frac{p}{E} \frac{\partial f}{\partial x^i} - \frac{\partial f}{\partial E} \left[\frac{p^2}{E} \frac{\partial\Phi}{\partial t} + \frac{\partial\Psi}{\partial x^i} \frac{p\hat{p}^i}{a} + \frac{p^2 H}{E} \right] = C[f]. \quad (2.64)$$

Next, we apply this equation to photons, dark matter, baryons and neutrinos. Although the collision term does not contribute in zeroth order, it does contribute for first or higher orders. Equation (2.10) should be applied for each case, according to which interactions the particle underwent through cosmic history.

Photons

For photons, equation (2.64) is simplified, since $E = p$. Moreover, we know that the equilibrium distribution for photons is the BE distribution (Eq. 2.29) with $\mu_\gamma = 0$. Perturbing the distribution function around the equilibrium, we write

$$\delta f(\mathbf{x}, \mathbf{p}, t) = -p \frac{\partial f_0}{\partial t} \Theta. \quad (2.65)$$

Since we are interested in the first order equation, we replace (2.65) in (2.64), and we get

$$\frac{df}{dt} \Big|_{1\text{st order}} = -p \frac{\partial f_0}{\partial p} \left[\frac{\partial\Theta}{\partial t} + \frac{\hat{p}_i}{a} \frac{\partial\Theta}{\partial x^i} + \frac{\partial\Psi}{\partial t} + \frac{\hat{p}_i}{a} \frac{\partial\Psi}{\partial x^i} \right] = C[f]. \quad (2.66)$$

The main interaction here is the Compton scattering, i.e. the scattering of the photon by an electron. The collision term is negligible for the zeroth order term, but it is relevant for first order perturbation or higher. We derive it from Eq. (2.10) following (Dodelson and Schmidt, 2020; Lima, 2019). Let \mathbf{q} , \mathbf{p} (\mathbf{q}' , \mathbf{p}') be, respectively, the electron and photon momenta before (after) the collision. Neglecting Pauli blocking, we have from Eq. (2.10) that

$$\begin{aligned} C[f(\mathbf{p})] &= \frac{1}{2E_\gamma(p)} \int \frac{d^3\mathbf{q}}{(2\pi)^3 2E_e(q)} \frac{d^3\mathbf{q}'}{(2\pi)^3 2E_e(q')} \frac{d^3\mathbf{p}'}{(2\pi)^3 2E_\gamma(p')} \\ &\times \sum |\mathcal{M}|^2 (2\pi)^4 \delta_D^{(3)}[\mathbf{p} + \mathbf{q} - \mathbf{p}' - \mathbf{q}'] \delta_D^{(1)}[E_\gamma(p) + E_e(q) - E_\gamma(p') - E_e(q')] \\ &\times [f_e(\mathbf{q}') f_\gamma(\mathbf{p}') - f_e(\mathbf{q}) f_\gamma(\mathbf{p})]. \end{aligned} \quad (2.67)$$

The sum in (2.67) is with respect to the final spin states of both the electron and the photon (two each) and also with respect to the initial spin state of the electron. The photon has energy $E_\gamma(p) = p$ and the electron $E_e(q) \approx m_e$, since it is non-relativistic. We can perform the integral in \mathbf{q}' removing the 3D Dirac delta, which results in

$$\begin{aligned} C[f(\mathbf{p})] &= \frac{\pi}{2m_e p} \int \frac{d^3\mathbf{q}}{(2\pi)^3 2m_e} \frac{d^3\mathbf{p}'}{(2\pi)^3 2(p')} \delta_D^{(1)}[p + E_e(q) - p' - E_e(|\mathbf{q} + \mathbf{p} - \mathbf{p}'|)] \\ &\times \sum |\mathcal{M}|^2 [f_e(\mathbf{q} + \mathbf{p} - \mathbf{p}') f_\gamma(\mathbf{p}') - f_e(\mathbf{q}) f_\gamma(\mathbf{p})]. \end{aligned} \quad (2.68)$$

Since the photon momentum is much lower than that of the electron, we can write

$$E_e(q) - E_e(|\mathbf{q} + \mathbf{p} - \mathbf{p}'|) = \frac{\mathbf{q}^2}{2m_e} - \frac{(\mathbf{q} + \mathbf{p} - \mathbf{p}')^2}{2m_e} \approx \frac{(\mathbf{p}' - \mathbf{p}) \cdot \mathbf{q}}{m_e}. \quad (2.69)$$

Then, we can do a Taylor expansion of the energy $(|\mathbf{q} + \mathbf{p} - \mathbf{p}'|)^2/(2m_e)$ around the zeroth order term $\mathbf{q}^2/(2m_e)$. The Dirac delta reads

$$\begin{aligned} \delta_D^{(1)}[p + E_e(q) - p' - E_e(|\mathbf{q} + \mathbf{p} - \mathbf{p}'|)] &\approx \delta_D^{(1)}(p - p') + \frac{(\mathbf{p}' - \mathbf{p}) \cdot \mathbf{q}}{m_e} \frac{\partial}{\partial p} \delta_D^{(1)}(p - p') \\ &\approx \delta_D^{(1)}(p - p') + \frac{(\mathbf{p} - \mathbf{p}') \cdot \mathbf{q}}{m_e} \frac{\partial}{\partial p'} \delta_D^{(1)}(p - p'). \end{aligned} \quad (2.70)$$

Replacing it in Eq. (2.68), we have

$$\begin{aligned} C[f(\mathbf{p})] &= \frac{\pi}{8m_e^2 p} \int \frac{d^3\mathbf{q}}{(2\pi)^3} f_e(\mathbf{q}) \frac{d^3\mathbf{p}'}{(2\pi)^3 2\mathbf{p}'} \sum |\mathcal{M}|^2 \\ &\times \left[\delta_D^{(1)}(p - p') + \frac{(\mathbf{p} - \mathbf{p}') \cdot \mathbf{q}}{m_e} \frac{\partial}{\partial p'} \delta_D^{(1)}(p - p') \right] [f(\mathbf{p}') - f(\mathbf{p}')] . \end{aligned} \quad (2.71)$$

For the amplitude of the Compton scattering we use the result

$$\begin{aligned} \sum |\mathcal{M}|^2 &= 24\pi\sigma_T m_e [1 + (\mathbf{p} \cdot \mathbf{p}')^2] \\ &= 32\pi\sigma_T m_e^2 \left[1 + \frac{1}{2} P_2(\mathbf{p} \cdot \mathbf{p}') \right] \approx 32\pi\sigma_T m_e^2 , \end{aligned} \quad (2.72)$$

where σ_T is the Thomson scattering cross-section. For now, let us neglect the dipole term which is subdominant. We are also neglecting the effect due to the photon polarization, which would add an extra term in Eq. (2.72). Under these assumptions, (2.72) is independent of the momenta involved, so the integral in \mathbf{q}' becomes simply $n_e/2$, where n_e is the number of electrons. The factor of $1/2$ arises due to the electron spin degeneracy. Moreover, we can expand the photon distribution functions up to first order (Eq. 2.65), so the collision term becomes

$$\begin{aligned} C[f(\mathbf{p})] &= \frac{2\pi^2 n_e \sigma_T}{p} \int \frac{d^3\mathbf{p}'}{(2\pi)^3 p'} \left[\delta_D^{(1)}(p - p') + (\mathbf{p} - \mathbf{p}') \cdot \mathbf{v}_b \frac{\partial}{\partial p'} \delta_D(p - p') \right] \\ &\times \left[f^{(0)}(p') - f^{(0)}(p) - p' \frac{\partial f^{(0)}}{\partial p'} \Theta(\hat{\mathbf{p}}') + p \frac{\partial f^{(0)}}{\partial p} \Theta(\hat{\mathbf{p}}) \right] . \end{aligned} \quad (2.73)$$

We also replaced $\mathbf{q}/m_e = \mathbf{v}_b$, where \mathbf{v}_b is the electron velocity. Since electrons and protons are tightly coupled through Coulomb scattering, they have a single fluid velocity, which we call *baryonic velocity*. Breaking the integral in a radial and an angular part, we have

$$\begin{aligned} C[f(\mathbf{p})] &= \frac{n_e \sigma_T}{4\pi p} \int_0^\infty dp' p' \int d\Omega' \left[\delta_D^{(1)}(p - p') \left(-p' \frac{\partial f^{(0)}}{\partial p'} \Theta(\hat{\mathbf{p}}') + p \frac{\partial f^{(0)}}{\partial p} \Theta(\hat{\mathbf{p}}) \right) \right. \\ &\left. + (\mathbf{p} - \mathbf{p}') \cdot \mathbf{v}_b \frac{\partial}{\partial p'} \delta_D(p - p') (f^{(0)}(p') - f^{(0)}(p)) \right] . \end{aligned} \quad (2.74)$$

We then calculate the radial integral. Using the definition of the zeroth multipole moment of the photon (Eq. 2.53), we have

$$C[f(\mathbf{p})] = \frac{n_e \sigma_T}{4\pi p} \int_0^\infty dp' p' \left[\delta_D^{(1)}(p - p') \left(-p' \frac{\partial f^{(0)}}{\partial p'} \Theta_0 + p \frac{\partial f^{(0)}}{\partial p} \Theta(\hat{\mathbf{p}}) \right) + \mathbf{p} \cdot \mathbf{v}_b \frac{\partial}{\partial p'} \delta_D(p - p') (f^{(0)}(p') - f^{(0)}(p)) \right]. \quad (2.75)$$

Using integral by parts in the second term,

$$C[f(\mathbf{p})] = \frac{n_e \sigma_T}{4\pi p} \int_0^\infty dp' p' \left[\delta_D^{(1)}(p - p') \left(-p' \frac{\partial f^{(0)}}{\partial p'} \Theta_0 + p \frac{\partial f^{(0)}}{\partial p} \Theta(\hat{\mathbf{p}}) \right) - \mathbf{p} \cdot \mathbf{v}_b \delta_D(p - p') \frac{\partial f^{(0)}}{\partial p'}(p') \right]. \quad (2.76)$$

Solving the integral, the collision term reads

$$C[f] = -p \frac{\partial f^{(0)}}{\partial p} n_e \sigma_T [\Theta_0 - \Theta(\hat{\mathbf{p}}) + \hat{\mathbf{p}} \cdot \mathbf{v}_b]. \quad (2.77)$$

Putting the collision term of Eq. (2.77) into Eq. (2.66) and transforming to Fourier space, the Boltzmann equation for photons reads

$$\Theta' + ik\mu\Theta + \Phi' + ik\mu\Psi = -\tau' [\Theta_0 - \Theta + \mu v_b], \quad (2.78)$$

where primes denote derivative with respect to conformal time and

$$\tau = \int_\eta^{\eta_0} d\eta a(\eta') n_e(\eta') \sigma_T \quad (2.79)$$

is called optical depth. Since $n_e \sigma_T$ is the photon scattering rate, the optical depth is the line-of-sight expected number of scatterings over cosmic history (Ribeiro, 2019).

Finally, one can include the dipole and polarization effects. The full equation becomes

$$\Theta' + ik\mu\Theta + \Phi' + ik\mu\Psi = -\tau' \left[\Theta_0 - \Theta + \mu v_b - \frac{1}{2} P_2(\mu) \Pi \right], \quad (2.80)$$

where

$$\Pi = \Theta_2 + \Theta_{P,2} + \Theta_{P,0}. \quad (2.81)$$

This term includes the temperature dipole (Θ_2), the polarization dipole ($\Theta_{P,2}$) and the polarization monopole ($\Theta_{P,0}$). The photon polarization field itself is described by the following Boltzmann equation

$$\Theta'_P + ik\mu\Theta_P = -\tau' \left[-\Theta_P + \frac{1}{2} (1 - P_2(\mu)) \Pi \right]. \quad (2.82)$$

As one can see, it is sourced by the quadrupole moment and no other moment of the temperature field. Also, in opposition to the temperature equation, polarization does not couple with gravity, baryons or any other component besides photons themselves. In fact, polarization is the result of successive Thomson scatterings, and therefore equation (2.82) reflects the microphysics of the process.

Dark Matter

In opposition to the photon equation, for dark matter we do not use an equilibrium distribution function to derive the Boltzmann equation. We just assume they are non-relativistic so that $(p/m)^2$ is negligible. The first equation comes from integrating Eq. (2.64) over the phase space, and the second one from the same procedure, but after previously multiplying Eq. (2.64) by the term p^j/E . The resulting equations are the zeroth and first order moments of the distribution function

$$\frac{\partial \delta}{\partial t} + \frac{1}{a} \frac{\partial v_{dm}^i}{\partial x^i} + 3 \frac{\partial \Phi}{\partial t} = 0, \quad (2.83)$$

$$\frac{\partial v_{dm}^i}{\partial t} + H v_{dm}^i + \frac{1}{a} \frac{\partial \Psi}{\partial x^i} = 0. \quad (2.84)$$

Moving to Fourier space and conformal time, and now assuming that the velocity is an irrotational field such that $v_{dm}^i = (k^i/k)v_{dm}$, we have

$$\delta'_{cdm} + ikv_{cdm} + 3\Phi' = 0, \quad (2.85)$$

$$v'_{cdm} + \left(\frac{a'}{a} \right) v_{cdm} + ik\Psi = 0. \quad (2.86)$$

Since dark matter is cold, i.e. non-relativistic, these equations do not couple with moments of second order or higher. Therefore, they fully describe dark matter motion. Moreover, we do not account for any collision term. In principle, dark matter does not interact with any other component since some time after its generation. However, a possible alternative scenario would

be a strongly self-interacting dark matter (Tulin and Yu, 2018). Another possibility concerns an interacting Dark Sector, for which there is an extensive literature. See e.g. (Wang et al., 2016a).

Baryons

Baryons, like dark matter, are non-relativistic, so their equation can be derived in a similar way. However, here we also need to take interactions into account. Both electrons and protons interact with photons via Compton scattering, and electrons also interact with protons via Coulomb scattering. In fact, the Coulomb scattering couples them together so tightly that they are forced into a single overdensity and a single velocity value, which allows us to treat them together as baryons. Reactions that change the number of electrons or nucleons such as pair production, annihilation and nuclear reactions are irrelevant around and after recombination. Moreover, we can also neglect Compton scattering of protons, so the relevant interactions are the Compton scattering of electrons and the Coulomb scattering. Therefore, one can take the zeroth and first order moments of the Boltzmann equations for electrons and protons and add them together. The resulting equations are

$$\delta'_b + ikv_b + 3\Phi' = 0, \quad (2.87)$$

$$v'_b + \left(\frac{a'}{a}\right)v_b + ik\Psi = \tau' \frac{4\rho_\gamma}{3\rho_b} [3i\Theta_1 + v_b]. \quad (2.88)$$

The LHS is identical to the dark matter case, as expected. The derivation of the collision term follows the same formalism that we presented for the photon case, and can be found in (Dodelson and Schmidt, 2020), for example. The dipole term in the RHS results in an effect called Compton drag. The electrons moving in the direction of higher temperature will face a drag force pointing in the opposite direction.

Neutrinos

Neutrinos, as well as photons, follow an equilibrium distribution function at zeroth order. So we can perform the same procedure of deriving the first order Boltzmann equation from the first order perturbation on the distribution function. However, there are a few differences that should be addressed. The first one is that we do not need to include any collision term, since interactions are negligible during the epochs of interest. The second one is that neutrinos have mass, so we no longer assume $E \approx p$ as we did for photons. Having this in mind, we can

proceed as in the photon case, getting

$$\mathcal{N}' + ik\mu \frac{p}{E_\nu(p)} \mathcal{N} - Hp \frac{\partial}{\partial p} \mathcal{N} + \Phi' + ik\mu \frac{E_\nu(p)}{p} \Psi = 0. \quad (2.89)$$

The LHS differs from the photon equation through the factors of E/p , which reduce to 1 when the temperature drops the neutrino mass and they become ultra-relativistic.

2.4 Correlation function and power spectra

In the previous section, we presented a set of coupled differential equations that describe the perturbed universe: the Einstein-Boltzmann equations. In principle, they can be solved for each k -mode given the initial condition. However, it is not trivial to guess the exact initial solution. The initial perturbations arise from quantum-mechanical fluctuations of the inflationary period and, therefore, carry a probabilistic character. For that reason, perturbations should be treated statistically. In this section we define the statistical functions commonly used in cosmology to characterize matter and radiation perturbations. Since these functions can be either simulated from the theory (Einstein-Boltzmann eq.) or estimated from the data (e.g. CMB, number counts of galaxies, IM experiments), they constitute a tool to test cosmological models and constraint parameters.

2.4.1 3D Correlation function

Suppose we have N astrophysical objects distributed in a volume V . The first interesting descriptor of such distribution is the number density $\bar{n} = N/V$. This information, despite being useful, is clearly not sufficient to characterize the distribution, since it does not tell us anything about how the population is distributed. Therefore, further definitions are required.

Let us take a small volume dV in V . The average number of particles in the infinitesimal volume is $\langle dN \rangle = \bar{n}dV$. However, taking two infinitesimal volumes dV_a and dV_b , the number of pairs given by one object inside dV_a and the other inside dV_b can be written as

$$\langle dN_a dN_b \rangle = \bar{n}^2 dV_a dV_b [1 + \xi(r_{ab})]. \quad (2.90)$$

This equation implicitly defines the 3D 2-point correlation function $\xi(r_{ab})$, where r_{ab} is the separation between these volumes. Notice that if the objects were randomly populated in V , without any preference with respect to the place, we would have $\langle dN_a dN_b \rangle = \langle dN_a \rangle \langle dN_b \rangle$

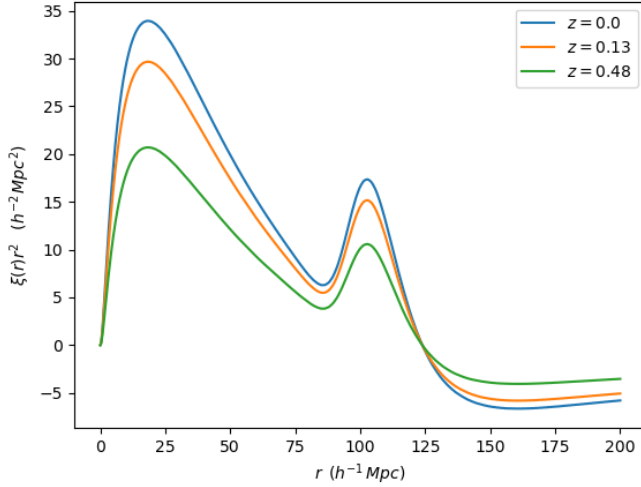


FIGURE 2.2: 2-point correlation function for selected redshift values computed with the CAMB free source code. The orange and green lines correspond to the redshift limits of operation for the BINGO experiment. Note how the BAO peak is visible in these redshift values.

and then ξ would vanish. Therefore, the $\xi(r_{ab})$ function gives us an incremental probability of finding objects separated by r_{ab} with respect to a random (Poisson) distribution. We can say that the objects are correlated if $\xi > 0$, anti-correlated if $\xi < 0$ and uncorrelated if $\xi = 0$. Alternatively, we can write the correlation function in terms of the overdensities. Writing $\delta(r_a) = dN_a / (\bar{n}dV_a) - 1$, we have

$$\xi(r_{ab}) = \langle \delta(r_a)\delta(r_b) \rangle . \quad (2.91)$$

In equations (2.90) and (2.91) (and in this thesis in general), the brackets $\langle \rangle$ denote an average over multiple realizations of the same type, e.g. N-body simulation, Gaussian or lognormal simulations, etc. In that sense, equations (2.90) and (2.91) mean that the same locations dV_a and dV_b are selected in each realization, and then the average is taken over the realizations. This is called *ensemble average*. Alternatively, we can take an average over all possible positions in a single realization

$$\xi(\mathbf{r}) = \frac{1}{V} \int dV_x \delta(\mathbf{x})\delta(\mathbf{x} + \mathbf{r}) , \quad (2.92)$$

which is called sample average. When $\xi(r_{ab})$ depends only on the separation \mathbf{r} and not on the specific locations r_a, r_b , the system is said to be *statically homogeneous*. Strictly speaking, the

higher-order statistics should also be independent of location in order for the system to be called statistically homogeneous. Moreover, if the ensemble average and the sample average coincide, the system is said to be *ergodic*. In astrophysics, it is more common to say that the system is a *fair sample* of the universe (Amendola and Tsujikawa, 2010).

If the distribution is also isotropic we can infer that ξ depends only on the modulus $r = |\mathbf{r}|$ of the separation vector. In practice, a good way of estimating ξ for a single realization is from

$$\hat{\xi} = \frac{DD(r)}{RR(r)} - 1, \quad (2.93)$$

where $DD(r)$ is the number of pairs separated by the distance r in the catalog, and $RR(r)$ is the number of pairs separated by the same distance but in a random (Poisson) catalog. This is called the natural estimator. Some other more elaborated estimators exist and can be found in (Landy and Szalay, 1993).

The expected correlation function which describes the Large Scale structures can be simulated with the help of some publicly available codes for solving the Einstein-Boltzmann equation. The most famous ones are the Code for Anisotropies in the Microwave Background - CAMB - (Lewis and Challinor, 2011) and the Cosmic Linear Anisotropy Solving System - CLASS - code (Lesgourges, 2011a). It has already been shown that these two independently written codes agree in a high precision level (Lesgourges, 2011b). In figure (2.2) we show some examples computed with the CAMB free-source code assuming a flat Λ CDM model with fiducial cosmology. The shape of this curve reflects the structure formation history. In fact, the Einstein-Boltzmann equations predict gravitational instability, which means that regions with higher density than its surroundings tend to attract more matter and become even more dense. This explains why the function decreases after the first peak in figure (2.2), indicating a higher correlation at small scales. Also, we recall that baryonic matter and radiation were tightly coupled in the early universe, which significantly impacted how the structures came to be what we observe today. In early times, gravitational instability was counterbalanced by the pressure imbalance of the plasma, caused by the photons trapped in it. Therefore, the structures at that time were oscillating rather than growing, due to this continuous dispute between pressure and gravity. As a result, spherical acoustic waves were emitted from each overdensity spot, and propagated through the primordial plasma until the matter-radiation decoupling occurred. These waves are called Baryon Acoustic Oscillations (BAO). Although they do not propagate anymore, they left an imprint in the structure formation. Since dark matter interacts with baryons gravitationally, the total matter (dark + baryons) ends up having the second peak shown in (2.2) at the scale corresponding to the sound horizon, i.e. the distance traveled by the

sound until decoupling. Further discussions and statistical analysis from the BAO signal can be found in (Marins, 2018, Ribeiro, 2019).

Higher orders

It is easy to see that the correlation function can be generalized to higher orders. For instance, the 3-point correlation function reads

$$\zeta_{abc} = \langle \delta(r_a) \delta(r_b) \delta(r_c) \rangle . \quad (2.94)$$

It can be shown that

$$\langle N_a N_b N_c \rangle = \bar{n}^3 dV_a dV_b dV_c (1 + \xi_{ab} + \xi_{bc} + \xi_{ac} + \zeta_{abc}) . \quad (2.95)$$

If the distribution is Gaussian, the 3-point function ζ_{abc} vanishes and the statistical properties of the field are fully described by the 2-point function. More information about the 3-point function and its Fourier transform, the bispectrum, can be found in (Melo, 2020).

2.4.2 2D angular correlation function

The 2-point 2D angular correlation function (2PACF) is pretty much like the 3D one, with the difference lying in the fact that it is applied to 2D catalogs. Instead of thinking of a distribution of N objects in a volume V , the objects are distributed over a sufficiently thin spherical shell centered at the observer. Then, instead of infinitesimal volumes, we define infinitesimal solid angles, so the number of pairs reads

$$\langle dN_a^i dN_b^j \rangle = \bar{n}^i \bar{n}^j d\Omega_a d\Omega_b [1 + \omega^{ij}(r_{ab})] . \quad (2.96)$$

We are now using superscripts i, j since the 3D volume surrounding the observer can be sliced in a sequence of concentric spherical shells. So the superscript denotes each one of these slices. For instance, a galaxy catalog can be projected in shells by

$$\delta_g^i(\mathbf{n}) = \int_{\Delta z^i} dz n^i(z) \delta_g(\mathbf{n}, z) , \quad (2.97)$$

where $n(z)$ is the selection function which also accounts for spectroscopic errors associated with the observation. In general, i, j denote any two 2D astrophysical fields, for instance, catalogs of different experiments or simulations, each one having their own set of redshift slices.

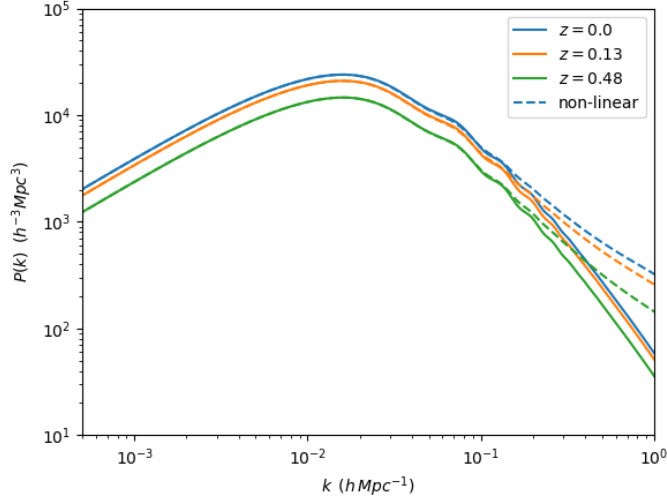


FIGURE 2.3: Matter power spectrum at selected redshift values computed with the CAMB free source code. In Fourier space, the BAO effect is manifested as wiggles around the wave number $k = 0.1 \text{ } h\text{Mpc}^{-1}$. Here we show the linear (solid lines) and non-linear (dashed lines) predictions.

By Similar arguments to the 3D case, the 2D 2-point correlation function can be written as

$$\omega^{ij}(\theta) = \langle \delta^i(\mathbf{n}) \delta^j(\mathbf{n}') \rangle , \quad (2.98)$$

where $\cos \theta = \mathbf{n} \cdot \mathbf{n}'$. Here, we are assuming isotropy and statistical homogeneity so that the correlation only depends on the angular separation between the objects. Moreover, we can define the variance by

$$\sigma_i^2 = \omega^{ii}(0) , \quad (2.99)$$

where σ_i means the standard deviation of the field at the same location. Furthermore, generalizations to higher orders, like the 3-point correlation, is similar to the 3D case and are left to the reader.

2.4.3 3D power spectrum

All the correlation functions defined above were defined in real space. However, in cosmology it is convenient to work in Fourier space since, as we have seen, in the linear theory each k -mode evolves independently. For our purposes, let us define the power spectrum as the Fourier

transform of the 3D 2-point correlation function

$$P(\mathbf{k}) = \int dV \xi(\mathbf{r}) e^{i\mathbf{k}\cdot\mathbf{r}}. \quad (2.100)$$

Assuming spatial isotropy, i.e. ξ depends only on $r = |\mathbf{r}|$, the power spectrum depends only on $k = |\mathbf{k}|$ and as a result,

$$P(k) = 4\pi \int dr r^2 \xi(r) \frac{\sin(kr)}{kr}. \quad (2.101)$$

Next, computing the ensemble average we find

$$\begin{aligned} \langle \delta(\mathbf{k}) \delta^*(\mathbf{k}') \rangle &= \int dV_x dV_r \langle \delta(\mathbf{x}) \delta(\mathbf{x} + \mathbf{r}) \rangle e^{-i(\mathbf{k}-\mathbf{k}')\cdot\mathbf{x} - i\mathbf{k}\cdot\mathbf{r}} \\ &= \int dV_x e^{-i(\mathbf{k}-\mathbf{k}')\cdot\mathbf{x}} \int dV_r \xi(\mathbf{r}) e^{-i\mathbf{k}\cdot\mathbf{r}} \\ &= (2\pi)^3 P(k) \delta_D(\mathbf{k} - \mathbf{k}'). \end{aligned} \quad (2.102)$$

See how similar this expression is to Eq. (2.91) or (2.98). We conclude that the power spectrum is also the second moment of the field (δ) in Fourier space, in a similar way as the 2-point correlation function is the second moment in real space. The Dirac delta function in Eq. (2.102) means that different k -modes are uncorrelated. This is expected since the modes are orthogonal.

In the same way as we did for the correlation function, we show the theoretical matter power spectrum computed with the CAMB free source code in figure (2.3). Since $P(k)$ is a Fourier transform of the $\xi(r)$ function, the solid lines contain the same information of the plots of figure (2.2), but in a different representation. As a matter of fact, what the package actually gives you is $P(k)$, and one should perform an inverse Fourier transform to find $\xi(r)$. In figure (2.3), the redshift effect is a simple rescaling of the amplitude, which is explained by the growth factor discussed below. Moreover, the wiggles (oscillations) in the plot are a manifestation of the BAO effect. To gain some intuition, remember that the Fourier transform of a Dirac delta is a plane wave. Hence, since the BAO is a bumping in real space, one can expect an oscillation pattern in Fourier space. Finally, figure (2.3) also compares the spectrum according to a linear description to the spectrum according to a nonlinear description given by the Takahashi fitting (Takahashi et al., 2012). One can see that both descriptions agree with each other in the higher scales (lower k), while the difference appears and increases in smaller scales (higher k). In fact, gravitational instability led to large perturbations on smaller scales so that gravity is no longer linear.

Growth factor

Due to the growth of matter perturbation, the matter power spectrum should in general depend on both k and z . At later times, the evolution of matter perturbations becomes scale independent and therefore can be described by a single time dependent factor D . Moreover, since the matter power spectrum is quadratic in δ , we have

$$\delta(\mathbf{k}, z) = D(z)\delta(\mathbf{k}, 0) \Rightarrow \quad (2.103)$$

$$P(k, z) = D(z)^2 P(k, 0). \quad (2.104)$$

The growth factor can be found from the Einstein-Boltzmann equations for $a \gg a_{\text{decoupling}}$. In this limit, we can neglect the pressure in the baryons, so that they follow the same equations of dark matter. In addition, we can assume that $k \gg aH$. This means that at later times, the horizon is much larger than the modes that interest us. The relevant equations are

$$k^2\Phi = 4\pi G a^2 \rho_m \delta_m, \quad (2.105)$$

$$\delta'_m + ikv_m = -3\Phi', \quad (2.106)$$

$$v'_m + \frac{a'}{a}v_m = ik\Phi. \quad (2.107)$$

Eq. (2.105) is Eq. (2.55) in the sub-horizon limit, and (2.106) and (2.107) describe the total matter. Multiplying Eq. (2.106) by a and taking the derivative with respect to conformal time, we have

$$(a\delta'_m)' + ik[a'v_m + av'_m] = -3(a\Phi')' \approx 0, \quad (2.108)$$

where the RHS vanishes in the sub-horizon limit. Inserting Eq. (2.107) into (2.108), we have

$$ak^2\Phi = (a\delta_m)'. \quad (2.109)$$

Then, inserting (2.105) into it, we get

$$(a\delta'_m)' = 4\pi G a^3 \rho_m \delta_m = 4\pi G a^3 (\rho_{\text{crit},0} \Omega_m a^{-3}) \delta_m \quad (2.110)$$

$$= \frac{3}{2} \Omega_m H_0^2 \delta_m, \quad (2.111)$$

where $\rho_{\text{crit},0}$ is the critical density (Eq. 2.18) evaluated at $z = 0$. It is convenient to transform the derivatives with respect to conformal time to derivatives with respect to the scale factor a .

Equation (2.111) then becomes

$$\frac{d^2\delta_m}{da^2} + \frac{d}{da} \ln(a^3 H) \frac{d\delta_m}{da} - \frac{3\Omega_m H_0^2}{2a^5 H^2} \delta_m = 0. \quad (2.112)$$

Assuming that the Hubble depends only on matter, curvature and cosmological constant, the non-decaying solution is (Dodelson and Schmidt, 2020; Hamilton, 2001)

$$D(a) \propto H(a) \int^a \frac{da'}{(a' H(a'))^3}. \quad (2.113)$$

Since the normalization is arbitrary, we can define it such that the growth factor is equal to the one we have today, so equation (2.104) holds. However, if dark energy is something other than a cosmological constant, equation (2.113) does not hold and one would have to solve Eq. (2.112) numerically.

Bias function

When probing large scale structure, we make use of same tracer of the underlying matter (e.g. galaxies, supernovae). However, we do not expect it to be unbiased with regards to the total underlying matter. This discrepancy is encoded by the bias function. Then the power spectrum of a tracer relates to the matter power spectrum by

$$\delta_T(\mathbf{k}, z) = b_T(z)\delta_m(\mathbf{k}, z) = b_T(z)D(z)\delta_m(\mathbf{k}, 0) \Rightarrow \quad (2.114)$$

$$P_T(\mathbf{k}, z) = b_T(z)^2 P_m(\mathbf{k}, z) = b_T(z)^2 D(z)^2 P_m(\mathbf{k}, 0). \quad (2.115)$$

This is also true, for instance, in Intensity Mapping experiments. Since the 21cm line comes from the Hydrogen atoms, we have a bias b_{HI} of the neutral Hydrogen with respect to the underlying matter.

Primordial power spectrum

As discussed previously, the statistical character in cosmology comes from the quantum mechanics of the early universe. Although we do not know the value of the perturbation in each point, the inflationary theory predicts the initial power spectrum for each component. They are usually parametrized in terms of the power spectrum of the curvature perturbation \mathcal{R}

$$\Delta_{\mathcal{R}}(k) = \frac{k^3}{(2\pi)^2} P_{\mathcal{R}}(k) = A_s \left(\frac{k}{k_0} \right)^{n_s - 1}. \quad (2.116)$$

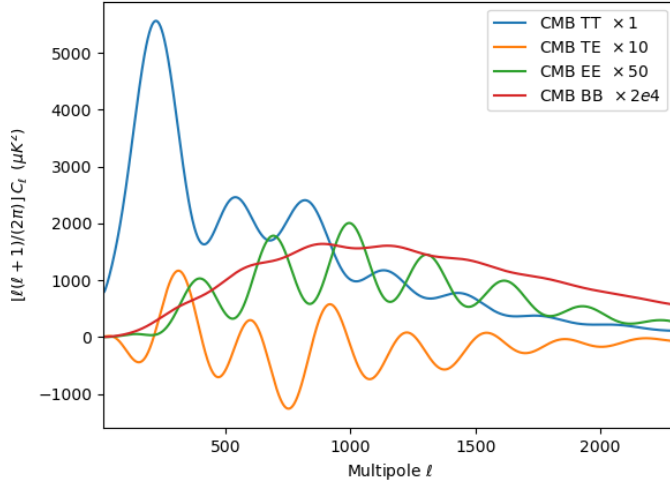


FIGURE 2.4: The CMB angular power spectrum computed with the free source CAMB code. T , E , B stand, respectively, for the brightness temperature, E -mode (gradient) polarization and B -mode (curl) polarization. The TT , TE , EE , BB are amplified by a factor of (1, 20, 50, 2e4) for better visualization.

We denote by $\Delta(k)$ the adimensional power spectrum, in opposition to $P(k)$, which has dimension of volume. The spectral index n_s is very close to unity, which means that the primordial spectrum is almost scale invariant. A_s is the amplitude of the primordial power spectrum. The pivot k_0 is arbitrary, usually defined as $k_0 = 0.5 \text{ Mpc}^{-1}$.

2.4.4 2D angular power spectrum

The 2D angular power spectrum (APS) is, like the 2D angular correlation function, applied to a 2D dataset. Instead of Fourier space, we project the fields into spherical harmonics

$$\delta^i(\hat{\mathbf{n}}) = \sum_{\ell=0}^{\infty} \sum_{m=-\ell}^{\ell} a_{\ell m}^i Y_{\ell m}^*(\hat{\mathbf{n}}). \quad (2.117)$$

In fact, the spherical harmonics are a complete set of eigenfunctions on the surface of a sphere, similarly as the e^{ikx} are a complete set of eigenfunctions. The reader should check appendix A for more information about spherical harmonics properties. The coefficients of the harmonic expansion are given by

$$a_{\ell m}^i = \int d\Omega \delta^i(\hat{\mathbf{n}}) Y_{\ell m}(\hat{\mathbf{n}}). \quad (2.118)$$

The set of coefficients $a_{\ell m}^i$ contains, therefore, the same information of the 2D field δ^i . The angular power spectrum is then defined by the ensemble average

$$\langle a_{\ell m}^i a_{\ell' m'}^{j*} \rangle = \delta_{\ell \ell'} \delta_{mm'} C_\ell^{ij}, \quad (2.119)$$

where isotropy implies they depend on just ℓ and not m . We can estimate the APS from a single realization by averaging on m the coefficients of equal ℓ . Let us recall that m is only allowed to assume values in the interval $\{-\ell, \dots, 0, \dots, \ell\}$, which means a total of $2\ell + 1$ m -values for each ℓ . One can expect that the higher multipoles will be more accurately estimated. The intrinsic uncertainty in the C_ℓ is called cosmic variance and is given by

$$\frac{\Delta C_\ell}{C_\ell} = \sqrt{\frac{2}{2\ell + 1}} \quad (2.120)$$

for Gaussian fields.

While the 3D power spectrum and the 3D correlation function can be transformed back and forth via direct and inverse Fourier transformations, we can also find a transformation between the 2D APS and the 2D correlation function. From equation (2.117) and the addition theorem (A.7), we find

$$\begin{aligned} \omega^{ij}(\theta) &= \sum_{\ell,m} \langle a_{\ell m}^i a_{\ell' m'}^{j*} \rangle Y_{\ell m}^*(\hat{\mathbf{n}}) Y_{\ell' m'}(\hat{\mathbf{n}}') \\ &= \frac{1}{4\pi} \sum_{\ell} (2\ell + 1) C_\ell^{ij} P_\ell(\cos \theta). \end{aligned} \quad (2.121)$$

Similarly, from Eq. (2.118)

$$\sum_m C_\ell^{ij} = \int d\Omega d\Omega' \omega^{ij}(\theta) \sum_m Y_{\ell m}(\hat{\mathbf{n}}) Y_{\ell m}^*(\hat{\mathbf{n}}'), \quad (2.122)$$

which yields

$$C_\ell^{ij} = 2\pi \int_0^\pi d\theta \sin \theta \omega^{ij}(\theta) P_\ell(\cos \theta). \quad (2.123)$$

The discussion of this section has been focused on the matter distribution, but the same concepts apply to CMB. Since we shall discuss in details the angular power spectrum (APS) for LSS in chapter 4, let us have a brief discussion about CMB spectrum here. The APS formalism is a natural tool to study CMB anisotropies, since our CMB sky is a spherical shell at $z \sim 1100$.

Photons have two independent polarization states. One way of decomposing it is in an E-mode (gradient) component and in a B-mode (curl) component. In figure (2.4), we show the C_ℓ^{TT} , C_ℓ^{TE} , C_ℓ^{EE} and C_ℓ^{BB} spectra, where E, B are the E, B -mode components and T is the brightness temperature. The E-mode contains valuable cosmological information, and has been measured very precisely by now. B-mode on the other hand can be used to search for non-scalar perturbations.

2.5 Lognormal fields

In this section we give a brief introduction to lognormal fields based on reference (Xavier, Abdalla and Joachimi, 2016). First of all, let us recall that a Gaussian field is the random field whose probability density (PDF) function is a multivariate Gaussian distribution. Although this is the simplest way of modelling an astrophysical field, it is not a good approximation. For instance, the matter overdensity field PDF should lie in the interval $[-1, \infty[$, while a Gaussian field is given in $] -\infty, \infty[$. Therefore, modelling this field as a Gaussian variable would lead to non-physical negative densities. The same argument would also work for temperature fields, since they have an absolute zero. A multivariate shifted lognormal distribution, on the other hand, constitutes a more versatile and appropriate way of modeling such astrophysical fields, thus avoiding non-physical quantities.

A set of variables Z_i following a multivariate Gaussian distribution is fully described by the mean $\mu_i = \langle Z_i \rangle$ and the covariance matrix $\omega_g^{ij} = \langle Z_i Z_j \rangle - \langle Z_i \rangle \langle Z_j \rangle$. All higher order moments vanish. Although we use the same notation for 2PACF and the covariance matrix of the variables¹, strictly speaking, they are only the same when $\langle Z_i \rangle = \langle Z_j \rangle = 0$. Given the set Z_i of Gaussian variables, one can define a set of multivariate shifted lognormal variables by (Xavier, Abdalla and Joachimi, 2016)

$$X_i = e^{Z_i} - \lambda_i . \quad (2.124)$$

From now on, we call them just lognormal variables or lognormal fields for short. They are fully described by the shift parameter λ_i , the associated Gaussian variable's mean μ_i and the covariance matrix ω_g^{ij} of the associated Gaussian variables. They have therefore one extra degree of freedom per field, which makes them more flexible than Gaussian variables.

Next, we relate the statistical descriptors (e.g. mean, covariance) of the lognormal variables to those of the associated Gaussian variables. First, expanding the exponential in Taylor series

¹Do not confuse this with the APS covariance matrix, which will be discussed in chapter 4

we have

$$\langle e^{Z_i} \rangle = e^{\mu_i} \sum_{n=0}^{\infty} \frac{\langle (Z_i - \mu_i)^n \rangle}{n!}. \quad (2.125)$$

The central Gaussian moments obey the relation

$$\langle (Z_i - \mu_i)^n \rangle = \begin{cases} 0 & \text{if } n \text{ is odd} \\ \frac{n!}{(n/2)!} \frac{\sigma_i^2}{2}^{n/2} & \text{if } n \text{ is even} \end{cases}. \quad (2.126)$$

Since the odd terms in (2.126) vanish, we replace equation (2.126) in equation (2.125) and rescale $n = 2m$, getting

$$\langle X_i \rangle = e^{\mu_i + \frac{\sigma_i^2}{2}} - \lambda_i. \quad (2.127)$$

This result shows us that the lognormal variable's mean depends on both the mean and the variance of the associated Gaussian variable. We can also use this relation to find the covariance matrix. Denoting $\alpha_i = \langle X_i \rangle + \lambda_i$, we have

$$\begin{aligned} \omega_{ln}^{ij} &= \langle X_i X_j \rangle - \langle X_i \rangle \langle X_j \rangle \\ &= \langle e^{Z_i + Z_j} \rangle - \alpha_i \alpha_j \\ &= \exp \left\{ \langle Z_i + Z_j \rangle + \frac{1}{2} [\langle (Z_i + Z_j)^2 \rangle - \langle Z_i + Z_j \rangle^2] \right\} - \alpha_i \alpha_j \\ &= \exp \left\{ \mu_i + \mu_j + \frac{1}{2} \sigma_i^2 + \frac{1}{2} \sigma_j^2 + \omega_g^{ij} \right\} - \alpha_i \alpha_j \\ &= \alpha_i \alpha_j \left(e^{\omega_g^{ij}} - 1 \right). \end{aligned} \quad (2.128)$$

Setting $i = j$ in eq. (2.128) we find the variance of the lognormal variable as

$$v_i = \langle X_i^2 \rangle - \langle X_i \rangle^2 = \alpha_i^2 \left(e^{\sigma_i^2} - 1 \right), \quad (2.129)$$

which also depends on both the mean (through α_i) and variance of its associated Gaussian variable. The same method can be used for the three-point correlation function. We find

$$\begin{aligned} \zeta_{ijk} &= \langle (X_i - \langle X_i \rangle)(X_j - \langle X_j \rangle)(X_k - \langle X_k \rangle) \rangle \\ &= \frac{\omega_{ln}^{ij}\omega_{ln}^{jk}\omega_{ln}^{ki}}{\alpha_i\alpha_j\alpha_k} + \frac{\omega_{ln}^{ji}\omega_{ln}^{ik}}{\alpha_i} + \frac{\omega_{ln}^{ij}\omega_{ln}^{jk}}{\alpha_j} + \frac{\omega_{ln}^{ik}\omega_{ln}^{kj}}{\alpha_k}. \end{aligned} \quad (2.130)$$

Defining *skewness* as

$$\gamma_i = \frac{(X_i - \langle X_i \rangle)^3}{v_i^{\frac{3}{2}}}, \quad (2.131)$$

we have

$$\gamma_i = \frac{\sqrt{v_i}}{\alpha_i} \left(\frac{v_i}{\alpha_i^2} + 3 \right). \quad (2.132)$$

This equation can be inverted to be solved for α_i . Although it is a cubic algebraic equation, only one of the solutions is real. We can then write the shift parameter λ_i as a function of the variable's mean, variance and skewness

$$\lambda_i = \frac{\sqrt{v_i}}{\gamma_i} \left[1 + y(\gamma_i) + \frac{1}{y(\gamma_i)} \right] - \langle X_i \rangle, \quad (2.133)$$

where

$$y = \sqrt[3]{\frac{2 + \gamma_i^2 + \gamma_i \sqrt{4 + \gamma_i^2}}{2}}. \quad (2.134)$$

Once we have computed λ_i , we can also find μ_i and σ_i in terms of the first three moments. Inverting equations (2.129) and (2.132) we have

$$\mu_i = \ln \left(\frac{\alpha_i^2}{\sqrt{\alpha_i^2 + v_i^2}} \right), \quad (2.135)$$

$$\sigma_i = \sqrt{\ln \left(1 + \frac{v_i}{\alpha_i^2} \right)}. \quad (2.136)$$

Therefore, one could use equations (2.133), (2.135) and (2.136) as a method to find a distribution from a dataset that has the exact same mean, variance and skewness.

Lognormals in harmonic space

We have seen that a collection of 2D isotropic random fields can be described by either their angular 2-point correlation function (2PACF) or by their angular power spectra (APS), which relate to each other by equations (2.121) and (2.123). If these fields are lognormal variables we can relate their APS with the ones of the associated Gaussian variables. Using equation (2.128)

together with (2.121) and (2.123), we find

$$\begin{aligned}
 C_g^{ij}(l) &= 2\pi \int_0^\infty \omega_g^{ij}(\theta) P_\ell(\cos \theta) \sin \theta d\theta \\
 &= 2\pi \int_0^\infty \ln \left[\frac{\omega_{ln}^{ij}(\theta)}{\alpha_i \alpha_j} + 1 \right] P_\ell(\cos \theta) \sin \theta d\theta \\
 &= 2\pi \int_0^\pi \ln \left[\sum_{\ell'=0}^{\infty} \frac{(2\ell' + 1)}{4\pi} \frac{C_{ln}^{ij}(\ell')}{\alpha_i \alpha_j} P_{\ell'}(\cos \theta) + 1 \right] P_\ell(\cos \theta) \sin \theta d\theta. \quad (2.137)
 \end{aligned}$$

Notice that each multipole of the associated Gaussian variable depends on *all* multipoles of the lognormal variable. In real space, on the other hand, the lognormal and associated Gaussian covariance matrices are related to each other at the same point (θ). In that case, we say that it is a *local* relation. Conversely, equation (2.137) is a *non-local* relation.

Chapter 3

The BINGO experiment and optics

The BINGO (**B**aryon **A**coustic **O**scillations from **I**ntegrated **N**eutral **G**as **O**bervation) telescope is a 21cm IM experiment designed to measure BAO in the radio band. BINGO will operate in the frequency range of 980–1260 MHz¹, corresponding to the redshift interval $0.13 < z < 0.45$, and it will survey an area of 6000 square degrees of the sky. A series of papers was recently published to describe the project (Abdalla, Ferreira et al., 2021), the instrument (Wuensche et al., 2021a), the optics (Abdalla, Marins, Motta et al., 2021), the mission (Licciano, Mericia, Wuensche et al., 2021), the component separation analyses (Fornazier, Abdalla et al., 2021), the HI mocks (Zhang, Motta, Novaes et al., 2021) and forecasts (Costa, Landim et al., 2021). In this chapter, we start with an overview of the project, and then we discuss the experiment, in particular the optical system and the optical design.

3.1 BINGO project overview

The standard approach to probe Large Scale Structure is through large galaxy-redshift surveys, where the galaxy positions and redshifts are measured individually, so that galaxies are used as tracers of the underlying total matter distribution. This method has been extensively used to probe LSS in the optical and far-infrared bands. However, measuring each galaxy individually is an expensive and inefficient way of mapping cosmological volume. It has been proposed another method called Intensity Mapping (IM) (Battye, Davies and Weller, 2004) that instead of identifying individual galaxies, measures the total flux from many galaxies, which gives us information on the underlying matter. Although other possibilities have been proposed, such as the CO lines (e.g. Lidz et al., 2011; Gong et al., 2011), most of the IM experiments are based on the observation of the 21cm line. This is a very typical spectral line radiation corresponding to the hyperfine transition in the Hydrogen atom. Since Hydrogen is the most

¹In the next chapters of this thesis, we assume an old convention of 960 – 1260 MHz, corresponding to the redshift interval $0.13 < z < 0.49$

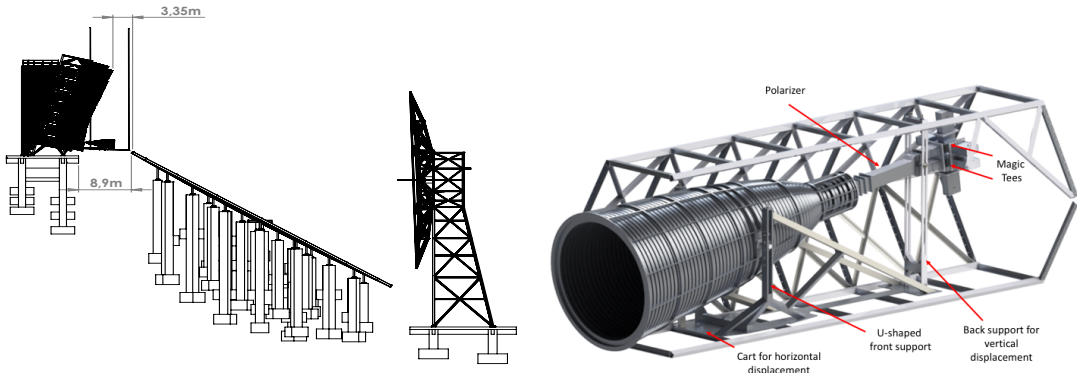


FIGURE 3.1: Left: A diagram of the telescope showing the primary and secondary reflectors, as well as the structure where the horns will be located. Right: The hexagonal cage for allocating each individual horn. The horn position can be displaced by $\pm 15\text{cm}$, $\pm 30\text{cm}$ from the center of the cage. Source: Wuensche et al., 2021a.

common visible (baryonic) element of the Universe, the HI distribution is a reliable tracer of the matter distribution itself. BINGO belongs to a new generation of telescopes based on the 21cm IM technique. Other remarkable examples are MeerKAT (Santos et al., 2017), Tianlai (Chen, 2012), CHIME (Bandura et al., 2014), HIRAX (Newburgh et al., 2016), HERA (DeBoer et al., 2017), as well as the SKA (Bacon et al., 2020).

The main scientific goal of BINGO is cosmology. The major problems in this field relate to the Dark-Sector (Dark Energy and Dark Matter). For instance, whether DE is a constant or a dynamical cosmological quantity and whether it interacts with DM are still topics to be solved (Wang et al., 2016a). BINGO will be a powerful tool to study these problems (Abdalla and Marins, 2020). Particularly, BINGO will be one of the first experiments to measure BAO in the radio band. BAO are known to be a powerful probe of DE properties and so far they have only been measured in the optical band. The IM observations will be complementary to those in the optical band, since each technique is susceptible to its own systematic errors. Although IM offers more effectiveness and less cost, it also brings new challenges. The 21cm signal is relatively weak and it is overwhelmed by both galactic and extra-galactic foreground radio emission at the same frequency. Therefore, an appropriate foreground removal technique is necessary (Fornazier, Abdalla et al., 2021). In addition to cosmology, BINGO is an experiment which is versatile enough to target other scientific goals, such as galactic science, as well as the study of transient objects. Some examples of transient objects to be detected are the FRBs (Fast Radio Bursts), bright bursts of radio photons of still unknown origin, and pulsars, which are rapidly spinning and highly magnetized neutron stars. The capability of detection of these transients are under study by the collaboration (Abdalla, Ferreira et al., 2021).

BINGO is a fixed transit telescope composed of a system of two mirrors working as a single dish radiometer. The telescope is currently under construction in the small village of Aguiar, in the state of Paraíba, Brazil. This site, which is a remote rural area, was chosen for presenting a very low Radio Frequency Interference (RFI) contamination. The telescope structure is North-South aligned and the primary reflector points to $DEC = -15^\circ$. The standard horn arrangement is made of 28 horns (detectors) distributed in the focal plane of the instrument. In this configuration, BINGO's instantaneous FoV (field-of-view) will be $14.75^\circ \times 6.0^\circ$ (DEC, RA), covering a 14.75° -wide declination strip as the sky drifts across the instrument's FoV. Each horn will be positioned inside a hexagonal cage and pointed to the secondary mirror. This hexagonal structure allows the horn to be positioned in the center of the cage or to be vertically displaced by $\pm 15\text{cm}$, $\pm 30\text{cm}$ with respect to the center in the longitudinal direction of the arrangement (i.e.: x-axis in fig. 3.3). These displacements were designed in order for the horn position to be able to be shifted a couple of times during the survey's lifetime, avoiding gaps in the sky coverage. A detailed explanation of the optical system and beams simulations is provided in the next section.

3.2 The optical System

The BINGO system is composed of two mirrors: one paraboloid, which is called primary mirror, and one hyperboloid, the secondary mirror. The primary one is pointed to the sky at an angle of 7.95° with respect to the local vertical axis. In the BINGO site ($Lat : 7^\circ 2' 27.6'' S$; $Lon : 38^\circ 16' 4.8'' W$) it corresponds to a declination of -15° in celestial coordinates. The light coming from the sky first hits the primary mirror, then, it is reflected in the secondary mirror surface, which is positioned at an angle of 85° with respect to the primary mirror. Finally, it reaches a set of detectors arranged and calibrated in order to maximize the received intensity. The system can be better visualized in figure (3.2), while figure (3.3) shows some possible arrangements of detectors we have analyzed. The axes in fig. (3.2) are in the *global coordinate system*, whose origin is placed in the center of the paraboloid. In this coordinate system, the surface of the primary reflector is given by

$$z = \frac{x^2 + y^2}{4f} \quad (3.1)$$

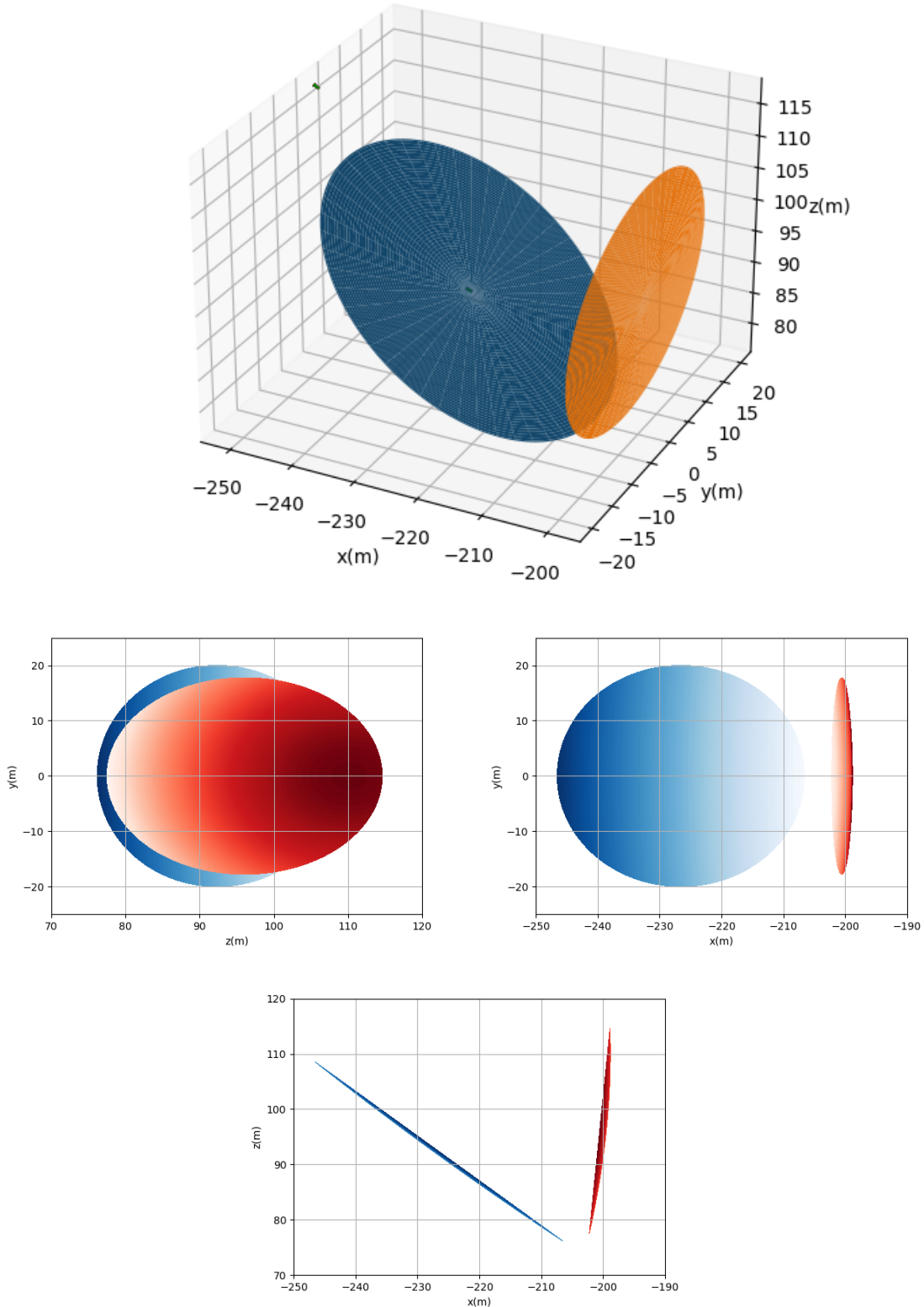


FIGURE 3.2: The BINGO optical system in 3D (top) and 2D perspectives: $x = 0$ (middle left), $z = 0$ (middle right), $y = 0$ (bottom). It is displayed in blue the primary reflector (paraboloid) and in red/orange the secondary reflector (hyperboloid). The center of the optical plane is represented by a green dot in the 3D plot.

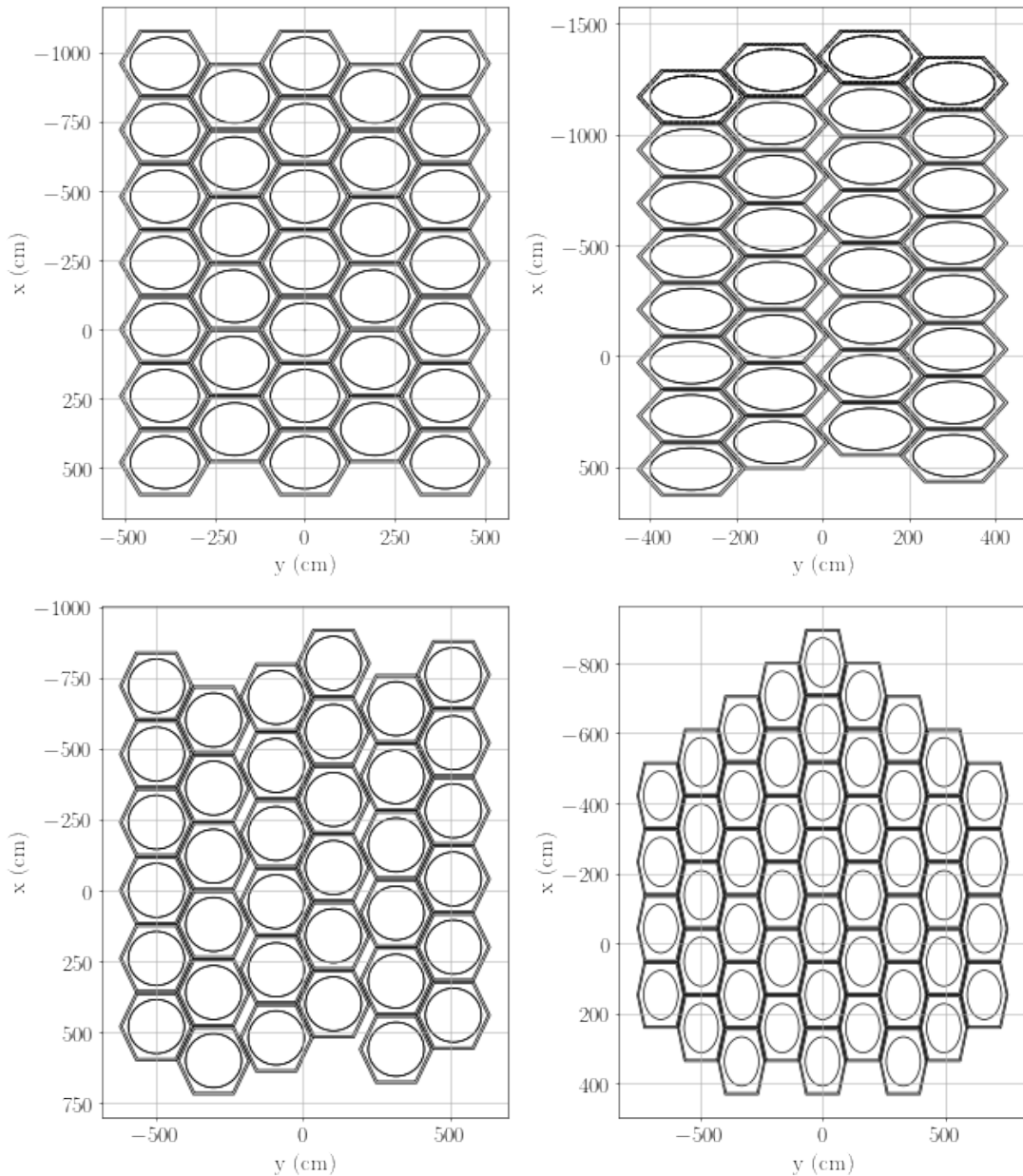


FIGURE 3.3: Four arrangements of detectors (horns) positioned along the optical plane. The *Rectangular arrangement* (upper left), *Double-Rectangular arrangement* (upper right), *Triple-Rectangular arrangement* (bottom left) and *Hexagonal arrangement* (bottom right). Source: (Abdalla, Marins, Motta et al., 2021).

and an elliptical contour that defines the rim (edges) of the dish is

$$\frac{(x - x_c)^2}{\alpha^2} + \frac{(y - y_c)^2}{\beta^2} = 1, \quad (3.2)$$

where $f = 140\text{m}$ is the focus of the paraboloid, $x_c = -226.54\text{m}$, $y_c = 0$ are the coordinates of the center of the dish, and $\alpha = \beta = 20\text{m}$ are the semi-axes of the dish. The secondary reflector, on the other hand, is defined at the coordinate system centered in the focus of the parabola $(0, 0, 140\text{m})$ and rotated by the Euler angles of $(180^\circ, 95^\circ, 0)$. We call this frame *subcoordinate system*. The hyperboloid equation is

$$z = c + \frac{a}{b} (b^2 + x^2 + y^2)^{\frac{1}{2}} ; \quad b = \sqrt{c^2 - a^2}, \quad (3.3)$$

where $a = 148.24\text{m}$ is the vertex distance and $c = 252\text{m}$ is the foci distance to the center of the hyperboloid. Moreover, the rim of the secondary reflector has center at $(x_c = 26.29\text{m}, y_c = 0)$, and semi-axes given by $\alpha = 18.34\text{m}$ and $\beta = 17.78\text{m}$, where x_c, y_c, α, β are the parameters of the ellipse (3.2) now defined in the *subcoordinate system*. Finally, we define the *feed coordinate system*. It is located in the position $(0, 0, 252\text{m})$ of the *subcoordinate system* (i.e.: in the foci of the hyperboloid), and rotated by $(0, 153.27^\circ, 180^\circ)$. In this frame we represent the positions of the detectors (3.3). The z coordinate, as well as the angular position, are free parameters that were set up by the optimization procedure described below.

3.2.1 Optimization of the optical plane

In this section, we describe how we define the optimal surface $z = z(x, y)$, $\hat{\theta} = \hat{\theta}(x, y)$, $\hat{\phi} = \hat{\phi}(x, y)$ in order to calibrate the best Cartesian and angular position of the detectors. For the simulation of the beam profile we used the GRASP student edition², a software dedicated to design and analysis of reflector antenna systems. We implemented the configurations of the BINGO optical system described above (section 3.2). For a given position (Cartesian and angular) of the detector, the software propagates a monochromatic, Gaussian and linearly polarized beam through the optical system, and provides the response as a 2-dimensional complex electrical field in $u - v$ coordinates over the sphere. The current follows the inverse direction of the light path, so the output simulates the beam measured by the detector after the successive reflections of the optical system, while the input (Gaussian) beam represents what would be measured when the sources are pointed directly to the horn. The appropriate width of the Gaussian was

²<https://www.ticra.com/software/grasp-student-edition/>

fitted according to measurements made at LIT (Laboratory of Integration and Tests) facilities at INPE (See Abdalla, Marins, Motta et al., 2021 and Wuensche et al., 2021a). In summary, the optimization procedure can be described as follows:

1. We selected several points over the XY plane of the *feed coordinate system*, covering the area where the horn arrangements are distributed (Fig. 3.3);
2. For each point (x, y) , we run GRASP for a horizontally polarized beam at 1100MHz , for some different values of (z, θ, ϕ) . We run the software as many times as needed to find the best (z, θ, ϕ) , i.e. the coordinates where the intensity peak reaches its maximum value;
3. From the results of the previous step, we fitted the functions $z = z(x, y)$, $\hat{\theta} = \hat{\theta}(x, y)$, $\hat{\phi} = \hat{\phi}(x, y)$, obtaining the optimal optical plane. We tested two different fitting methods: Least Square Method and Dense Neural Network (DDN). See (Abdalla, Marins, Motta et al., 2021);
4. Finally, we applied the fitting results to the coordinates (x, y) given by the horn arrangements of figure (3.3).

3.2.2 Beam analysis

In this section we compare the beams of the different arrangements and analyze some beam features such as polarization and spectrum. This same discussion was also exposed in our collaboration paper (Abdalla, Marins, Motta et al., 2021). The content of this section is similar to this reference since it constitutes my main contribution to the paper.

We compute the beams for all the horn positions using the GRASP software, where we set up the z, θ, ϕ according to the results of the Least Square fitting. We simulated the beams for both horizontally and vertically polarized cases in order to better study the beam polarization and to be able to simulate the response of an unpolarized beam. The same fitting was also used to compute the beams for frequencies other than 1100MHz , when necessary.

Even though the GRASP outputs are in $u - v$ coordinates, we chose to present them in celestial coordinates (RA, DEC). Given the transit nature of the telescope, these beams will rotate around the sky in RA at a fixed DEC. Therefore, the reader can infer how the beams sweep the sky. For this purpose, we perform a linear interpolation of the data in those coordinates according to the sequence of transformations defined below. First of all, we transform to standard

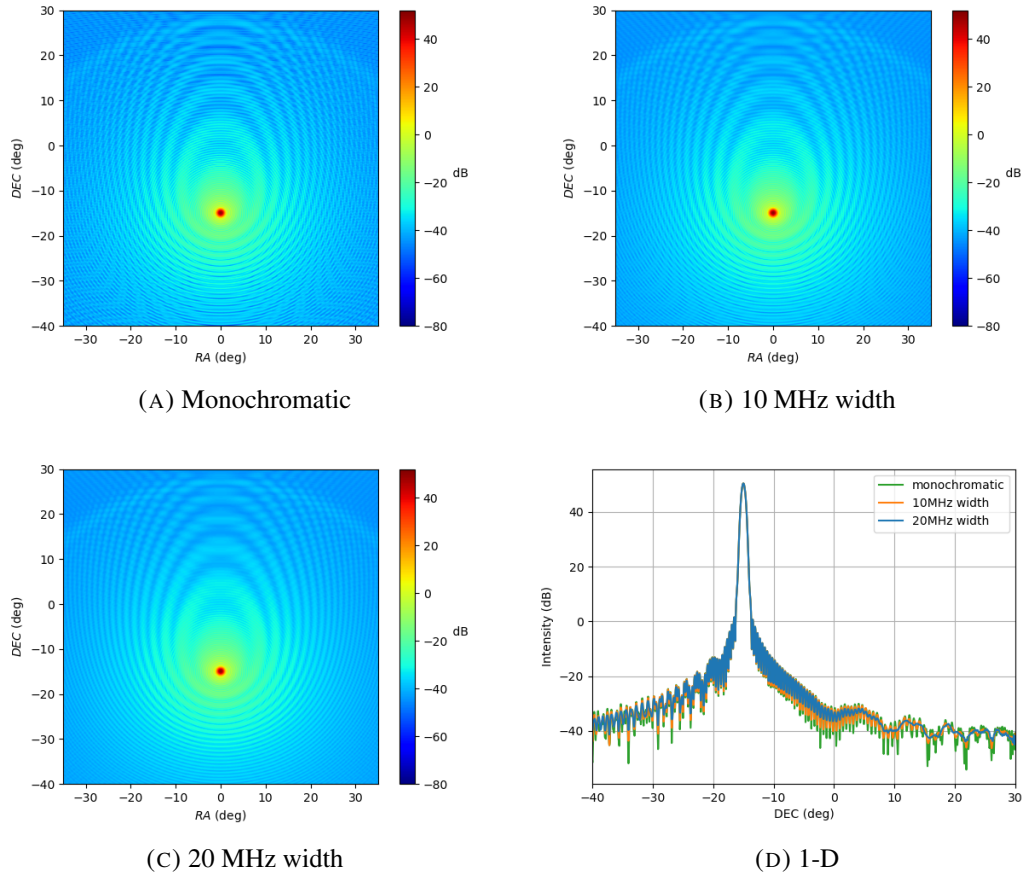


FIGURE 3.4: The side lobes of BINGO’s central beam present a moiré effect due to the two-mirror configuration of the instrument (figure 3.4a). We found that this effect attenuates when integrating the beam over the frequency. Figures (3.4b) and (3.4c) show integrated beams over widths of 10 MHz and 20 MHz respectively, computed in the ranges of 1105 – 1115 MHz and 1100 – 1120 MHz, with displacements of 1 MHz, and normalized by the number of steps. The attenuation effect is also clearer in fig. (3.4d), that portrays a 1-dimensional cut of those three results combined.

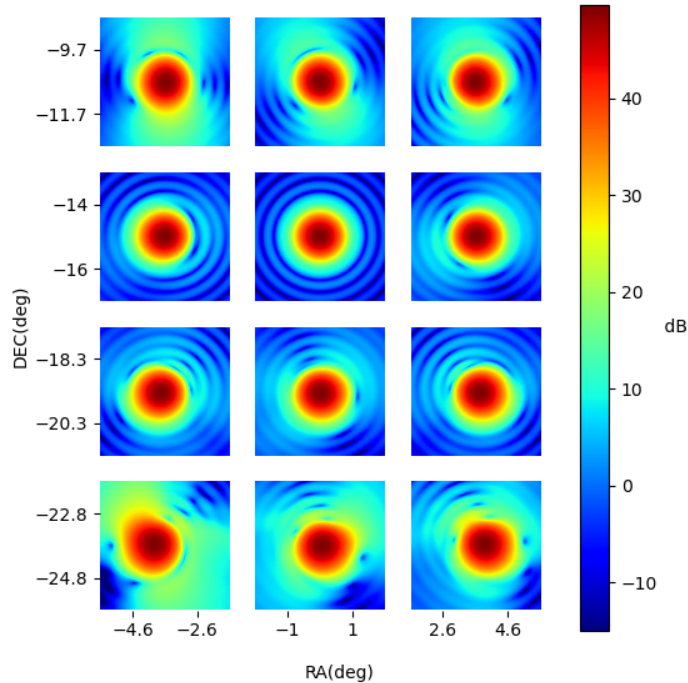


FIGURE 3.5: We present here the optical aberrations for the final beams of the horns located at different places within the focal plane. The focus of the telescope is placed at -15 DEC and has a beam which is devoid of aberrations, while the aberrations are increasingly large as we move away from the focal center of the telescope (we note here that the focal plane chosen in all configurations has a focus at -15 DEC, but given its asymmetry, the center of the focal plane is always at a lower declination). We can see, however, that the peak of the beam is relatively well maintained in this range of locations chosen, and that the aberrations remain at a level around 30 dB below that of the main beam. This gives us confidence that the optical aberrations within the field-of-view chosen by this work can be well modelled when the final survey is produced.

Cartesian coordinates (x, y, z) on the unit sphere

$$x = u, \quad (3.4)$$

$$y = v, \quad (3.5)$$

$$z = \sqrt{1 - u^2 - v^2}. \quad (3.6)$$

The $u - v$ coordinates can be understood as a plane tangent to the sphere at the center of the beam, which is at $x = y = 0$ and $z = 1$ in this system. In order to transform to Celestial

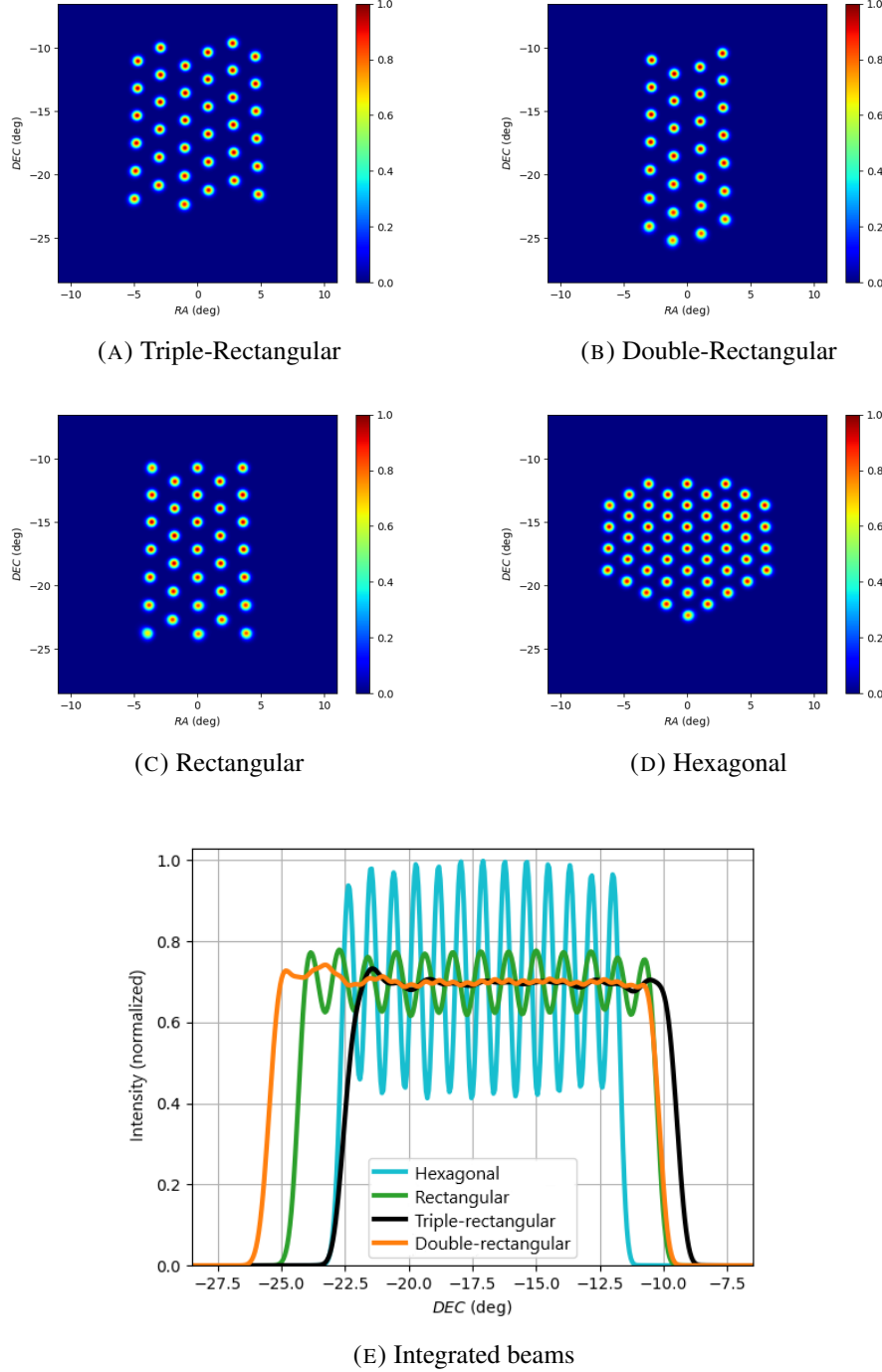


FIGURE 3.6: (3.6a), (3.6b), (3.6c), (3.6d): Beam responses (intensities) for, respectively, the Triple-Rectangular, Double-Rectangular, Rectangular and Hexagonal arrangements, normalized by the intensity of the central horn (see Eq. (3.11)). Fig. (3.6e): Response function of the beams, integrated in RA, for selected columns (corresponding to a declination range) and different horn arrangements. Results are normalized to the response of the central horn, according to Eq. (3.12). For the Triple-Rectangular and Double-Rectangular arrangements, the beam average also took into account the five displacements of 0, $\pm 15\text{cm}$, $\pm 30\text{cm}$. For the Rectangular arrangement, the five displacements were 0, $\pm 21\text{cm}$, $\pm 42\text{cm}$.

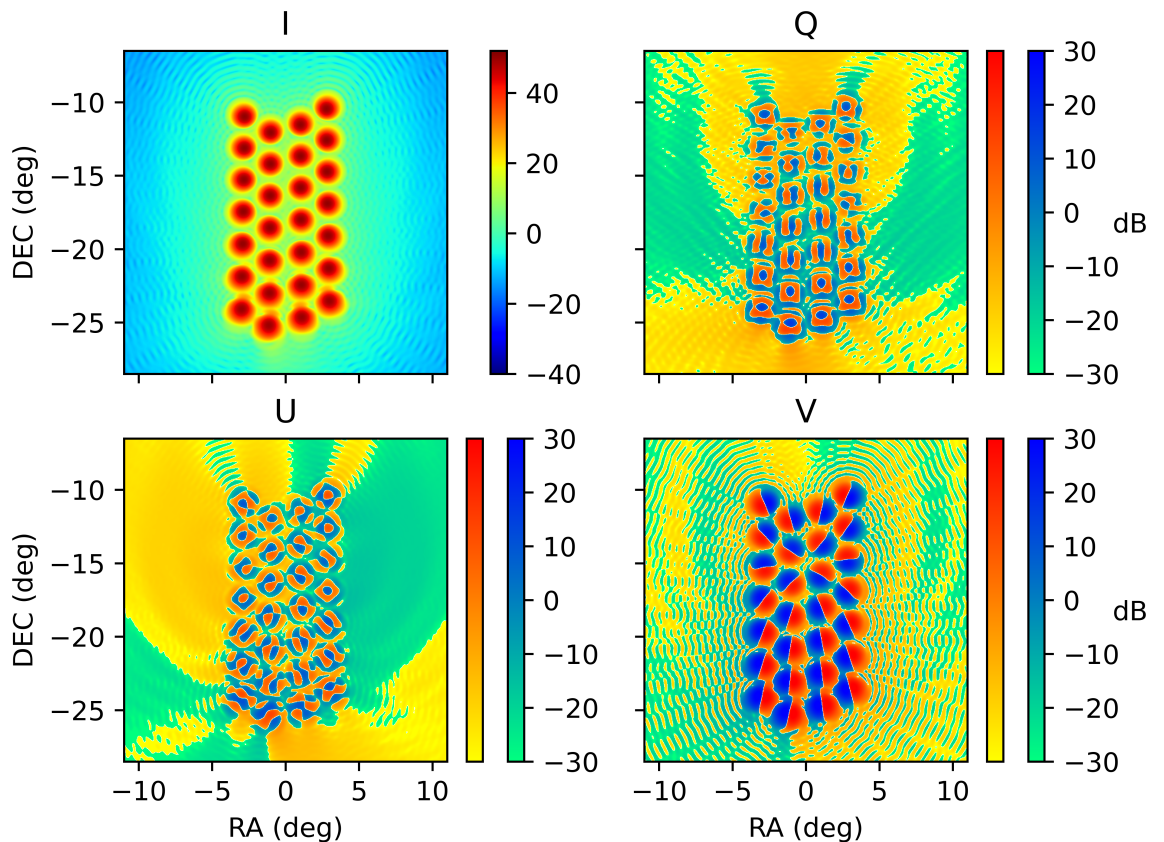


FIGURE 3.7: The Stokes parameters I, Q, U, V summed over for the beams of the Double-Rectangular arrangement, and transformed into dB units, i.e. $X_{dB} = 10 \log_{10}(\pm X)$. The two color bars indicate the positive (red) and negative (blue) values for the Q, U and V parameters. Each beam was previously averaged between the responses of each linearly polarized state.

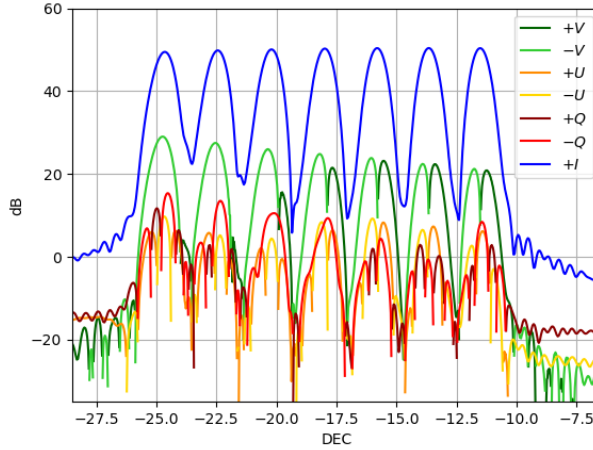


FIGURE 3.8: A one-dimensional cut of the Stokes parameters presented in Fig. (3.7) for the Double-Rectangular arrangement. The cut is over $\text{RA} = \text{RA}_{\text{peak}}$, where RA_{peak} is the coordinate of the peak intensity. We see that V is at least 25 dB lower than I on the peaks, while Q and U are even lower.

coordinates, however, it is helpful to define a new Cartesian system such that the z -axis points to the Celestial North pole. We choose to rotate the center of the focal plane so that it is located at a declination of -15° of the Celestial Equatorial plane. Therefore, we are required to perform a rotation of 105° from the celestial pole, which is where GRASP was set up to produce our beam:

$$\begin{pmatrix} x' \\ y' \\ z' \end{pmatrix} = \begin{pmatrix} \cos 105^\circ & 0 & \sin 105^\circ \\ 0 & 1 & 0 \\ -\sin 105^\circ & 0 & \cos 105^\circ \end{pmatrix} \begin{pmatrix} x \\ y \\ z \end{pmatrix}. \quad (3.7)$$

The definitions of the Celestial coordinates follow straightforwardly

$$\text{DEC} = \arcsin(z'), \quad (3.8)$$

$$\text{RA} = \text{arctan2}(y', x') = 2 \arctan \left(\frac{y'}{\sqrt{(x'^2 + y'^2)} + x'} \right). \quad (3.9)$$

In fig. (3.4) we can see the response due only to BINGO's central horn. The quantity being plotted is the intensity $I_{\text{dB}} = 10 \log_{10}(I)$, where the intensity I (in watt) is defined by the sum of squares of the two orthogonal components of the electric field

$$I = |E_{\text{co}}|^2 + |E_{\text{ex}}|^2, \quad (3.10)$$

where E_{co} is the electric field measured in linear polarization and E_{cx} is the electric field measured in cross polarization. We further take an average of the intensities resulting from each linearly polarized beam.

Furthermore, for the sake of comparing the different configurations, we define a total intensity for the arrangement, normalized by the intensity peak of the central horn, according to

$$p_{\text{arr}}^{\nu}(\text{RA}, \text{DEC}) = \frac{\sum^{\text{horn}} I_{\text{horn}}^{\nu}(\text{RA}, \text{DEC})}{I^{1100 \text{ MHz}}(0, -15^{\circ})}, \quad (3.11)$$

and its one-dimensional version

$$P_{\text{arr}}^{\nu}(\text{DEC}) = f \times \frac{\int d\text{RA} \sum^{\text{horn}} I_{\text{horn}}^{\nu}(\text{RA}, \text{DEC})}{\int d\text{RA} I^{1100 \text{ MHz}}(\text{RA}, -15^{\circ})}, \quad (3.12)$$

where the RA dependence is removed by integration, in the same way as in Fig. (3.4). These equations were applied to the four proposed horn arrangements, namely: Hexagonal, Retangular, Double-Retangular and Triple-Retangular. The results of applying Eq. (3.11) to the Double-Rectangular, Triple-Rectangular, Rectangular and Hexagonal arrangements are shown in Figures (3.6a, 3.6b, 3.6c and 3.6d), respectively, while the results of applying Eq. (3.12) are depicted in Fig. (3.6e). Although the sum in Eq. (3.11) is performed over *all* horns, in Eq. (3.12) we select columns of the arrangement in order to avoid the superposition of horns with the same declination. The selection covers the central columns of the horns and also one column adjacent to the central one for the Rectangular and Hexagonal arrangements. For the Double and Triple-Rectangular, however, we select all the columns, since their particular geometry does not create overlaps. For this reason, in Eq. (3.12) we set $f = 1/2$ for the Double-Rectangular, $f = 1/3$ for the Triple-Rectangular, and $f = 1$ for the others, since for the Double (Triple)-Rectangular the beams are summed over twice (triple) the numbers of columns. This has been chosen so that the contents of Fig. (3.6e) reflect the integrated beam while the sky sweeps across the focal plane.

Additionally, the results presented for the Rectangular, Double-Rectangular and Triple-Rectangular arrangements in Fig. (3.6e) were averaged over the five displacements of $0, \pm 15\text{cm}$, $\pm 30\text{cm}$ (Double and Triple-Rectangular) and $0, \pm 21\text{cm}, \pm 42\text{cm}$ (Rectangular). This average produces a smoother intensity profile for those arrangements, although the Double (and Triple)-Rectangular smoothness is also, in part, due to the non-redundant geometry of the arrangement. We conclude that this smoothness will most likely lead to a sky coverage which avoids gaps.

Finally, the configuration that best achieves smoothness with the minimum number of horns is the Double rectangular arrangement, and this is the configuration which we adopt as standard

for the project.

The beam polarization

We investigate the polarization by computing the four Stokes parameters for each beam and by summing them over for each arrangement. We apply the following definitions

$$I = |E_{\text{co}}|^2 + |E_{\text{cx}}|^2 = |E_a|^2 + |E_b|^2 = |E_{\text{rhc}}|^2 + |E_{\text{lhc}}|^2, \quad (3.13)$$

$$Q = |E_{\text{co}}|^2 - |E_{\text{cx}}|^2, \quad (3.14)$$

$$U = |E_a|^2 - |E_b|^2, \quad (3.15)$$

$$V = |E_{\text{rhc}}|^2 - |E_{\text{lhc}}|^2, \quad (3.16)$$

where the subscripts refer to three different bases of the space of Jones vectors, used to define the polarization of light. The $(e_{\text{co}}, e_{\text{cx}})$ are the standard Cartesian bases, lying in the direction of the (u, v) coordinates. Then, (e_a, e_b) are Cartesian bases rotated by 45° with respect to $(e_{\text{co}}, e_{\text{cx}})$, and $(e_{\text{lhc}}, e_{\text{rhc}})$ are the circular bases (left-hand side and right-hand side), defined as follows

$$e_{a/b} = \frac{1}{\sqrt{2}} (\pm e_{\text{co}} + e_{\text{cx}}), \quad (3.17)$$

$$e_{\text{lhc/rhc}} = \frac{1}{\sqrt{2}} (e_{\text{co}} \pm ie_{\text{cx}}). \quad (3.18)$$

The responses of each perfectly linearly polarized beam are still highly (although not perfectly) polarized, presenting either highly positive or highly negative Q values. Aiming to simulate the polarization gained through the optical system by an originally unpolarized beam, and assuming that ‘originally unpolarized’ refers to the simulated input signal, we average the response of both orthogonal polarized beams. In opposition to Q and U , that are highly dependent of these initial states, the I and V values are nearly the same for the two polarized states. Nevertheless, this method enables us to subtract any effects due to the initial state of polarization.

The results of the Stokes parameters for the Double-Rectangular arrangement are shown in Fig. (3.8), as well as a 1-dimensional cut in Fig. (3.8). Each parameter is summed over all the beams of the configuration, computed in the frequency of 1100 MHz. Of course Q , U , V are allowed to be either positive or negative, and the variation in their sign reveals a balance between the field directions. It is also instructive to compare the magnitude of the parameters. In Fig. (3.8) we see that V is at least 25 dB lower than I in the peaks, and the difference is even higher for the Q and U parameters.

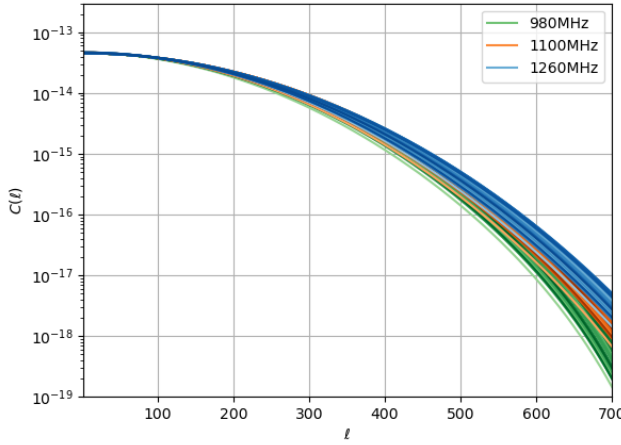


FIGURE 3.9: Auto angular power spectra for the Double-Rectangular arrangement beams. Low frequency beams reach low values in the spectra for high ℓ . Since we have previously normalized the intensity, the spectra is adimensional.

The power spectrum of the beams

In this section we compute the power spectra of the beams to investigate the effect they will have in modifying the final power spectrum of the 21-cm radiation under study. This estimation is important, since any strong features in the beam could be misinterpreted as a feature measured in the 21cm power spectrum.

In order to compute the beam spectrum, our first step was to convert our data to HEALPi \times format. We linearly interpolated the values of intensity of each beam from the original $u - v$ coordinates to the coordinates of the centers of the pixels of a HEALPi \times pixelated sphere with $N_{\text{side}} = 1024$. This N_{side} value was set in order to make the new resolution compatible with that of our GRASP simulations. Also, we set as zero the intensity outside the area where the simulations were performed, since it is expected to be very low far from the beam's center. Afterwards, we computed the projections into harmonic space and all the angular power spectra by

$$C_\ell = \sum_{m=-\ell}^{\ell} a_{\ell m}^* a_{\ell m}. \quad (3.19)$$

The intensities of each map were previously normalized by their sum over the pixels. The spectra of the beams of the Double-Rectangular arrangement are shown in Fig. (3.9) for the frequencies of 980 MHz, 1100 MHz and 1260 MHz. We see that these spectra reach lower

values for high ℓ in lower frequencies.

We draw the conclusion that the beams are smooth and concentrated enough as to not add any significant effects to the measurements of the power spectrum of the 21-cm in the angular scales relevant to BINGO. Furthermore, such modelling can be used in order to produce a more realistic fit to the beams, so that this can be used for map-making. However, due to the under illumination of the secondary mirror, the beams are very close to Gaussian in the center of the field, with only minor optical aberrations shown in Fig. (3.5).

Chapter 4

Angular Power Spectra: theory, measurements and covariance

Angular power spectrum is one of the most important tools to quantify anisotropies in large scale structures. In order to recover cosmological parameters from it, we need to compare an APS theory to measurements. In this chapter we explore the theory of APS and how we estimate it from 2-dimensional maps. Next, we discuss APS covariance. We present both a theoretical model and a building method from lognormal simulations.

4.1 The theoretical APS

We introduced APS in chapter 2 together with other correlators. Here the discussion is more technical, since we aim to show the equations that are implemented. In the code, the 3D matter power spectrum $P(k)$ from CLASS is transformed into APS for a set of redshift bins. This section explains this procedure.

4.1.1 Projection on the sky

For a given 3-dimensional cosmological field (e.g: galaxy field, HI temperature, CMB temperature, etc), we aim to define a 2-dimensional function over the sky. For that purpose, we slice the fields in thin spherical shells centered at the observer, and we remove the radial dependence by integration. For instance, for a galaxy density field $\delta_g(\chi(z)\hat{\mathbf{n}}, z)$, we can define

$$\delta_g(\hat{\mathbf{n}}) = \int dz n(z) \delta_g(\chi(z)\hat{\mathbf{n}}, z), \quad (4.1)$$

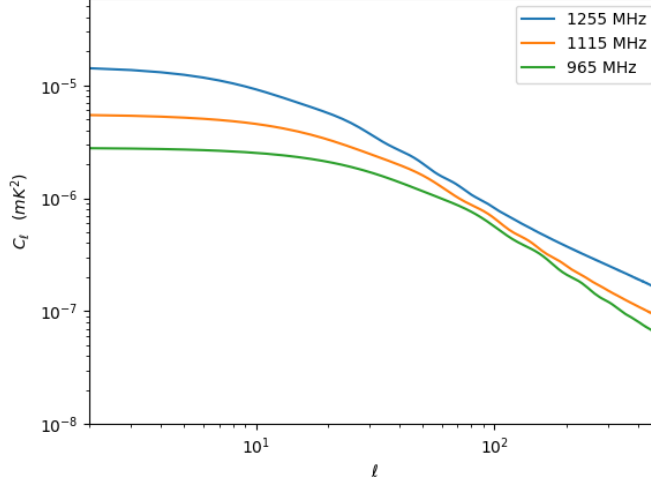


FIGURE 4.1: Angular Power Spectrum computed with the UCLCL code of the HI IM temperature for the lowest, an intermediate one, and the highest redshift bins for the BINGO setting: 30 channels of $\Delta\nu = 10\text{MHz}$ in the range of 960MHz to 1260MHz. We account both RSD and non-linear effects.

where $n(z)$ is a normalized redshift-dependent selection function. In the same way, we may define a projected HI temperature perturbation as

$$\delta T_{HI}(\hat{\mathbf{n}}) = \int dz \bar{W}(z) \bar{T}_{HI}(z) \delta_{HI}(\chi(z) \hat{\mathbf{n}}, z), \quad (4.2)$$

where $\bar{W}(z)$ is the window function, that we take to be constant; $\bar{T}_{HI}(z)$ is the mean temperature at a given redshift; and δ_{HI} is the HI overdensity (Olivari et al., 2017).

From now on, we follow a similar treatment to the one presented in (Loureiro et al., 2019) or (Padmanabhan et al., 2007) for the angular power spectrum formalism. First, let us make a Fourier decomposition followed by a wave plane decomposition in spherical harmonics (A.8) to get, for the galaxy field,

$$\begin{aligned} \delta_g(\hat{\mathbf{n}}) &= \int dz n(z) \int \frac{d^3\mathbf{k}}{(2\pi)^3} \delta_g(\mathbf{k}, z) e^{-i\mathbf{k}\cdot\chi\hat{\mathbf{n}}} \\ &= 4\pi \sum_{\ell,m} i^\ell \int dz n(z) \int \frac{d^3\mathbf{k}}{(2\pi)^3} \delta_g(\mathbf{k}, z) Y_{\ell m}^*(\hat{\mathbf{k}}) Y_{\ell m}(\hat{\mathbf{n}}). \end{aligned} \quad (4.3)$$

Therefore, using $\delta_g(\mathbf{k}, z) = b_g(z) D(z) \delta(\mathbf{k})$, where $b_g(z)$ is the bias of the galaxy field with respect to the matter field $\delta(\mathbf{k})$, and $D(z)$ is the growth function, and writing the galaxy field as

a decomposition in terms of spherical harmonics, i.e., $\delta_g(\hat{\mathbf{n}}) = \sum_{\ell,m} \delta_{g,\ell m} Y_{\ell m}(\hat{\mathbf{n}})$, we find

$$\delta_{g,\ell m} = 4\pi i^\ell \int \frac{d^3 k}{(2\pi^3)} W_{g,\ell}(k) \delta(\mathbf{k}) Y_{\ell m}^*(\mathbf{k}), \quad (4.4)$$

where we collect all redshift-dependence in the window function

$$W_{g,\ell}(k) = \int dz n(z) b(z) D(z) j_\ell(k \chi(z)). \quad (4.5)$$

Reproducing the previous steps (equations 4.3 - 4.5) for the HI temperature fluctuation (4.2), we find the HI Intensity Mapping window as

$$W_{IM,\ell}(k) = \int dz \bar{T}(z) \bar{W}(z) b_{HI}(z) D(z) j_\ell(k \chi(z)), \quad (4.6)$$

where b_{HI} is the bias of the HI with respect to the matter overdensity. Notice that, by similar arguments, one may also find the window function that satisfies equation (4.4) for any other field that relates to the matter overdensity. It constitutes a unified formalism to compute the Angular Power Spectra $\langle a_{\ell m}^i a_{\ell' m'}^{j*} \rangle$ for any fields a^i, a^j in terms of the 3-dimensional matter power spectrum. Using $\langle \delta(\mathbf{k}) \delta(\mathbf{k}') \rangle = (2\pi)^3 \delta^3(\mathbf{k} - \mathbf{k}') P(k)$ and the orthonormality relation for the spherical harmonics (A.5), we have

$$\begin{aligned} C_\ell^{ij} &\equiv \langle a_{\ell m}^i a_{\ell' m'}^{j*} \rangle \\ &= (4\pi)^2 \int \frac{d^3 k}{(2\pi^3)} \frac{d^3 k'}{(2\pi^3)} W_\ell^i(k) W_{\ell'}^{j*}(k') Y_{\ell m}^*(\mathbf{k}) Y_{\ell' m'}(\mathbf{k}') \langle \delta(\mathbf{k}) \delta(\mathbf{k}') \rangle \\ &= (4\pi)^2 \int d\Omega_k Y_{\ell m}^*(\mathbf{k}) Y_{\ell' m'}(\mathbf{k}') \int \frac{dk}{(2\pi)^3} k^2 W_\ell^i(k) W_{\ell'}^j(k) P(k) \\ &= \frac{2}{\pi} \int dk k^2 P(k) W_\ell^i(k) W_{\ell'}^j(k). \end{aligned} \quad (4.7)$$

Since $P(\mathbf{k})$ can be easily evaluated with codes like CLASS (Lesgourges, 2011a) or CAMB (Lewis and Challinor, 2011), the main task for computing the APS becomes computing the window functions of our interest. The superscripts i, j may stand for either different redshift bins of the same survey or of different surveys. C_ℓ^{ii} ($i = j$) is called an *auto- C_ℓ* , and C_ℓ^{ij} for $i \neq j$ is called a *cross- C_ℓ* . In figure (4.1) we show some of the auto- C_ℓ for the BINGO survey. While the auto- C_ℓ are always positive by definition, the cross- C_ℓ are allowed to be either positive or negative. We are also taking into account Redshift Space Distortion (RSD) and non-linear effects that are explained in the following subsections.

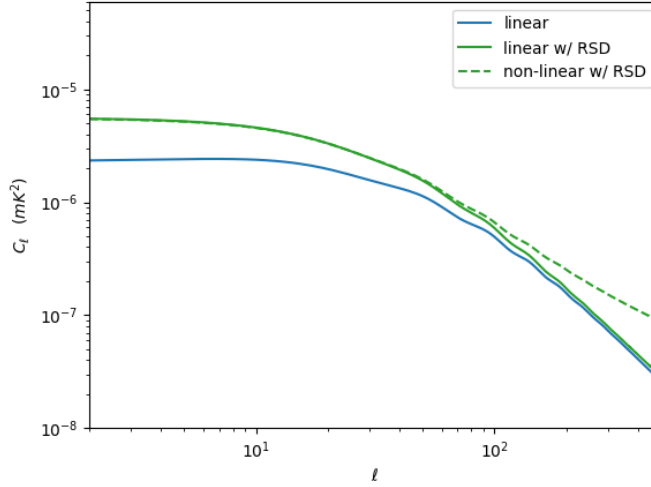


FIGURE 4.2: Angular Power Spectrum computed with UCLCL code for the HI IM temperature with $\Delta\nu = 10\text{MHz}$ centered at 1115MHz . We show three cases: linear, linear accounting for RSD, and non-linear accounting for RSD. The effect of the RSD is an increase of the APS in low ℓ and the effect of non-linearities is a decrease of the APS in high ℓ .

4.1.2 Redshift Space Distortion

The above discussion neglected the effect of peculiar velocities in the modelling of APS. However, this creates an illusion that the objects moving towards us appear to be closer, while the ones moving away from us appear to be further away. Therefore, we should account for this effect when modelling our window functions. Here, we follow the method also discussed in, e.g. (Padmanabhan et al., 2007). Letting $s = \chi + \mathbf{v} \cdot \hat{\mathbf{n}}$ be the redshift distance, we write

$$1 + \delta_g(\hat{\mathbf{n}}) = \int d\chi n(s) [1 + \delta_g(\chi, \chi \hat{\mathbf{n}})] . \quad (4.8)$$

Then, an expansion in Taylor Series,

$$n(s) \approx n(\chi) + \frac{dn}{d\chi} (\mathbf{v}(\chi \hat{\mathbf{n}}) \cdot \hat{\mathbf{n}}) , \quad (4.9)$$

allows us to write the total field as $\delta_g = \delta_g^0 + \delta_g^{RSD}$, where the zeroth-order term is the field without Redshift Space Distortion and the first-order term is the RSD correction term. Now, we

use the fact that

$$v(\mathbf{k}) = -i\beta\delta(\mathbf{k})\frac{\mathbf{k}}{k^2}, \quad (4.10)$$

where $\beta = (\mathrm{d} \ln D(z) / \mathrm{d} \ln a) / b(z) \approx \Omega_m^\gamma(z) / b(z)$. Making a Fourier decomposition and rearranging the terms, we find

$$\begin{aligned} \delta_g^{RSD} &= \int d\chi \frac{dn}{d\chi} (\mathbf{v}(\chi \hat{\mathbf{n}})) \\ &= \int d\chi \frac{dn}{d\chi} \int \frac{d^3\mathbf{k}}{(2\pi)^3} (\mathbf{v}(\mathbf{k}) \cdot \hat{\mathbf{n}} e^{-i\mathbf{k} \cdot \hat{\mathbf{n}}\chi}) \\ &= -i\beta \int d\chi \frac{dn}{d\chi} \int \frac{d^3\mathbf{k}}{(2\pi)^3} \delta(\mathbf{k}) \frac{\mathbf{k} \cdot \hat{\mathbf{n}}}{k^2} \exp(-i\mathbf{k} \cdot \hat{\mathbf{n}}\chi) \\ &= i\beta \int d\chi \frac{dn}{d\chi} \int \frac{d^3\mathbf{k}}{(2\pi)^3} \frac{\delta(\mathbf{k})}{k} \frac{d}{d(k\chi)} \exp(-i\mathbf{k} \cdot \hat{\mathbf{n}}\chi). \end{aligned} \quad (4.11)$$

By the plane wave expansion in Spherical Harmonics (A.8), we have

$$\delta_{\ell m}^{RSD} = 4\pi i^\ell \int \frac{d^3\mathbf{k}}{(2\pi)^3} W_\ell^{RSD}(\mathbf{k}) \delta(\mathbf{k}) Y_{\ell m}^*(\mathbf{k}), \quad (4.12)$$

where the RSD window function is given by

$$W_\ell^{RSD} = \frac{\beta}{k} \int d\chi \frac{dn}{d\chi} j'_\ell(k\chi). \quad (4.13)$$

Therefore, it is straightforward from equations (4.12) and (4.9) that Eq. (4.13) is the first-order correction term for the window function:

$$W_\ell^{tot}(k) = W_\ell^0(k) + W_\ell^{RSD}(k). \quad (4.14)$$

Although we presented the proof for a galaxy field, one should notice that this can be generalized for an IM field by replacing the galaxy selection function $n(z)$ by the mean temperature $\bar{T}(z)$. The effect of the RSD corrections on the APS is an increase in large scales $\ell < 60$, as you can see in figure (4.2). One application is that RSD can be used to constrain the dynamics of the Dark Sector, as in (Costa et al., 2017) for example.

4.1.3 Non-linearities

Here, we aim to show how we account for non-linearities in the window functions. We can define the ratio between the matter overdensity in the non-linear and linear theory as

$$R_{NL} \equiv \frac{\delta_{NL}(k, \chi)}{\delta_L(k, \chi)} = \left(\frac{P_{NL}(k, \chi)}{P_L(k, \chi)} \right)^{1/2}. \quad (4.15)$$

This ratio can be extracted from the CLASS code, where the non-linear overdensity is computed with the modified Takahashi Halofit (Takahashi et al., 2012). The non-linear 3d matter power spectrum relates to the linear 3d matter power spectrum by

$$\begin{aligned} P_{NL}(k\chi) &= R_{NL}^2(k\chi)P_L(k, \chi) \\ &= R_{NL}^2(k\chi)P_L(k, \chi). \end{aligned} \quad (4.16)$$

If the redshift bin is thin enough, we may assume that the ratio is roughly constant over z and we just compute it at the center of the bin,

$$R_{NL}(k, z) = R_{NL}(k, \bar{z}^i). \quad (4.17)$$

The window function should, therefore, be corrected by

$$W_{NL,\ell}^i(k) = R_{NL}(k, \bar{z}^i)W_{L,\ell}^i(k). \quad (4.18)$$

4.1.4 UCLCL code

In our work, we use the *Unified Cosmological Library for C_ℓ* (UCLCL), a library for calculating the Angular Power Spectrum of cosmological fields. The C_ℓ are computed from equation (4.7). The matter power spectrum $P(k)$ is extracted from the CLASS code, and we compute the window functions using equations (4.5) and (4.6). We can include RSD effects via equation (4.13). Moreover, non-linearities can be included, as explained in subsection 4.1.3.

4.2 Cut sky formalism

So far, we have computed APS assuming fields in the whole sphere. However, for comparison with real data, we need to take into account that the data is mostly available in only a portion of the sky. Therefore we introduce the angular mask function $W(\hat{\mathbf{n}})$ that takes into account the

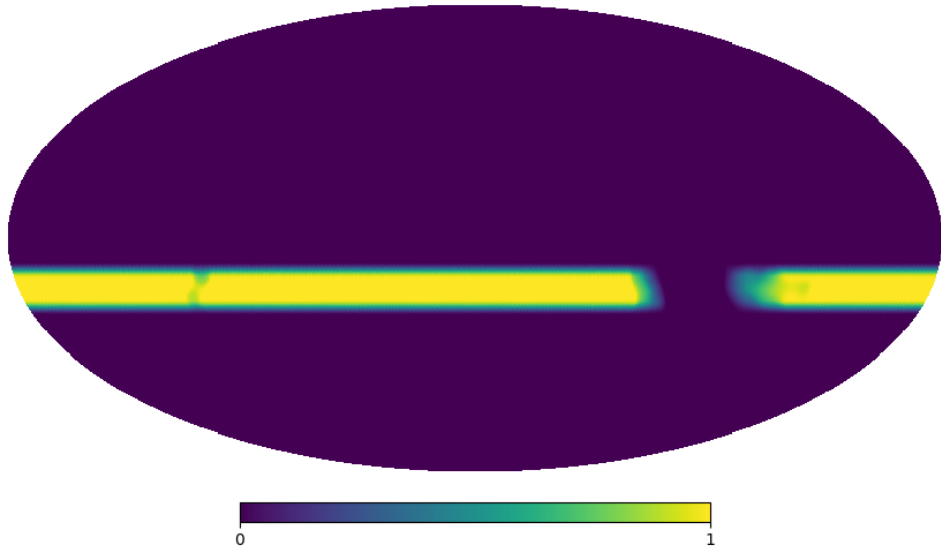


FIGURE 4.3: Mask for the BINGO experiment. Since the galaxy is a source of contamination, it also takes into account the location of the galaxy, in addition to the observation coverage itself. The mask is also apodized in the borders in order to avoid optical effects in the pixels at the border of the survey, due the wave nature of light.

area of observation and other instrumental effects, and we show how it corrects the APS. Local relations on real space lead to non-local relations in Harmonic space, giving rise to the coupling kernel $R_{\ell\ell'}$, that we will refer to as the mixing matrix.

The simplest way of defining a mask is to assign ‘one’ for the points that belong to the observation area, and ‘zero’ for the points outside the observation area. However, a weighted mask is frequently used, as, for instance, in the BINGO pipeline (Fornazier, Abdalla et al., 2021). In this case, the mask reflects not only the area of observation, but also the regions of the sky with high contamination. The mask is weighted (apodized) to control optical aberrations in the borders of the survey due to the wave nature of light. This is the mask we use in the BINGO simulations. Therefore, the formalism presented here considers the fact that the mask is allowed to assume any real number in the $[0, 1]$ interval, and the binary case can be regarded as a particular case. We follow mainly (Hivon et al., 2002; Dahlen and Simons, 2008; Scharf et al., 1992).

4.2.1 The projection operator

A scalar field defined in the whole sky can be projected on Spherical Harmonics by

$$f(\hat{\mathbf{n}}) = \sum_{\ell,m} f_{\ell m} Y_{\ell m}(\hat{\mathbf{n}}), \quad (4.19)$$

where the coefficients can be found through the Spherical Harmonics orthonormality relation (A.5) as

$$f_{\ell m} = \int_{\Omega} d\Omega f(\hat{\mathbf{n}}) Y_{\ell m}^*(\hat{\mathbf{n}}). \quad (4.20)$$

However, in the partial sky scenario, the coefficients must be corrected by the corresponding angular mask function $W(\hat{\mathbf{n}})$. Let us find how the coefficients computed when the mask is taken into account relates to the full sky coefficients of the Harmonic expansion. Including the mask $W(\hat{\mathbf{n}})$ in Eq. (4.20), we find

$$\begin{aligned} f_{\ell m}^{PS} &= \int_{\Omega} d\Omega W(\hat{\mathbf{n}}) f(\hat{\mathbf{n}}) Y_{\ell m}^*(\hat{\mathbf{n}}) \\ &= \int_{\Omega} d\Omega W(\hat{\mathbf{n}}) Y_{\ell m}^*(\hat{\mathbf{n}}) \sum_{\ell',m'} f_{\ell',m'} Y_{\ell'm'}(\hat{\mathbf{n}}) \\ &= \sum_{\ell'm'} D_{\ell m, \ell' m'} f_{\ell' m'}, \end{aligned} \quad (4.21)$$

where

$$D_{\ell m, \ell' m'} \equiv \int_{\Omega} d\Omega W(\hat{\mathbf{n}}) Y_{\ell m}^*(\hat{\mathbf{n}}) Y_{\ell' m'}(\hat{\mathbf{n}}) \quad (4.22)$$

is the projection operator.

Properties of the projection operator

Let us establish some useful properties of the projection operator. A straightforward one is

$$D_{\ell m, \ell' m'}^* = D_{\ell' m', \ell m}, \quad (4.23)$$

which can be seen by applying the complex conjugation directly to the definition (4.22). Another useful formula is

$$\begin{aligned} \sum_{p,q} D_{\ell m,pq} D_{pq,\ell' m'} &= \sum_{p,q} \int_{\Omega\Omega'} d\Omega d\Omega' W(\hat{\mathbf{n}}) W(\hat{\mathbf{n}}') Y_{\ell m}^*(\hat{\mathbf{n}}) Y_{pq}(\hat{\mathbf{n}}) Y_{pq}^*(\hat{\mathbf{n}}') Y_{\ell' m'}(\hat{\mathbf{n}}') \\ &= \int_{\Omega} d\Omega W^2(\hat{\mathbf{n}}) Y_{\ell m}^*(\hat{\mathbf{n}}) Y_{\ell' m'}(\hat{\mathbf{n}}) . \end{aligned} \quad (4.24)$$

Notice the appearance of a power of the mask function. Since $W(\hat{\mathbf{n}})$ can be a weighted mask, we cannot neglect its exponent in this formula. Next, let us define the following quantities

$$I_{\ell m} \equiv \int_{\Omega} d\Omega W(\hat{\mathbf{n}}) Y_{\ell m}^* , \quad J_{\ell m} \equiv \int_{\Omega} d\Omega W^2(\hat{\mathbf{n}}) |Y_{\ell m}|^2 . \quad (4.25)$$

The first definition is the mask projected on Harmonic space. The mask APS is therefore

$$\mathcal{W}_{\ell} = \frac{1}{2\ell + 1} \sum_{m=-\ell}^{\ell} |I_{\ell m}|^2 . \quad (4.26)$$

The second definition together with the result (4.24) allows us to write

$$J_{\ell m} = \sum_{p,q} D_{\ell m,pq} D_{pq,\ell m} = \sum_{p,q} D_{\ell m,pq} D_{\ell m,pq}^* = \sum_{p,q} |D_{\ell m,pq}|^2 . \quad (4.27)$$

The last relevant result is the projection on the 00 multipole. We have

$$D_{\ell m,00} = \frac{1}{\sqrt{4\pi}} \int_{\Omega} d\Omega W Y_{\ell m}^* = \frac{I_{\ell m}}{\sqrt{4\pi}} . \quad (4.28)$$

4.2.2 The pseudo-APS

We have, so far, defined a projection operator that relates the full sky coefficient of an expansion in Spherical Harmonics $f_{\ell m}$ to its partial sky equivalent $f_{\ell m}^{PS}$. What we want here is to find the partial sky equivalent of the APS. The definition of APS itself does not apply to partial sky because the Spherical Harmonics are only orthonormal in the whole sphere. Therefore, we define a *pseudo* Angular Power Spectrum, which has some different properties, by equation

$$S_{\ell_1}^{ij} \equiv \frac{1}{2\ell_1 + 1} \sum_{m_1=-\ell_1}^{\ell_1} \langle f_{\ell_1 m_1}^{PSi} f_{\ell_1 m_1}^{PSj*} \rangle . \quad (4.29)$$

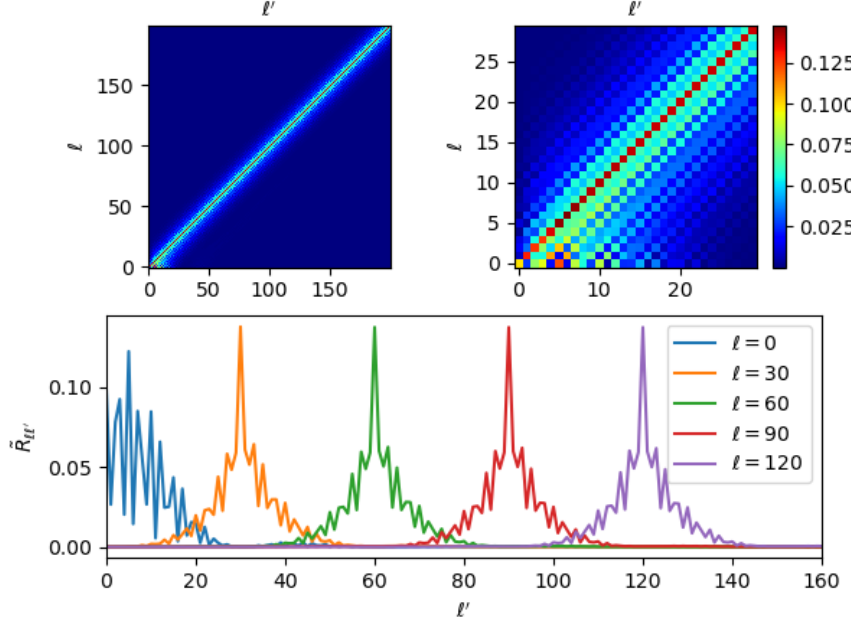


FIGURE 4.4: Mixing matrix computed for a binary BINGO mask. On the upper left and right we show 2D plots in different ℓ ranges, while on the bottom, 1D cuts of the matrix are shown.

We use (4.21) to relate it to the full sky APS through the projection operator

$$\begin{aligned} S_{\ell_1}^{ij} &= \frac{1}{2\ell_1 + 1} \sum_{m_1=-\ell_1}^{\ell_1} \sum_{\ell_2, m_2, \ell_3, m_3} D_{\ell_1 m_1, \ell_2 m_2} D_{\ell_1 m_1, \ell_3 m_3}^* \langle f_{\ell_2 m_2}^i f_{\ell_3 m_3}^{j*} \rangle \\ &= \frac{1}{2\ell_1 + 1} \sum_{m_1=-\ell_1}^{\ell_1} \sum_{\ell_2, m_2} |D_{\ell_1 m_1, \ell_2 m_2}|^2 C_{\ell_2}^{ij}. \end{aligned} \quad (4.30)$$

Renormalization

The pseudo-APS defined in (4.29) is biased with respect to the area of the sky. We can check this effect by testing a constant APS $C_\ell = C$ in equation (4.30). In light of equation (4.27), we can renormalize the pseudo-APS in terms of $J_{\ell m}$. The simplest definition is

$$\tilde{S}_\ell^{ij} \equiv \frac{1}{2\ell + 1} \sum_{m=-\ell}^{\ell} \frac{\langle f_{\ell m}^{PSi} f_{\ell m}^{PSj*} \rangle}{J_{\ell m}}. \quad (4.31)$$

However, (Peebles, 1973) and Hauser and Peebles, 1973) propose a modified formula

$$\tilde{S}_\ell^{ij} \equiv \frac{\sum_m \langle f_{\ell m}^{PSi} f_{\ell m}^{PSj*} \rangle}{\sum_m J_{\ell m}} = \frac{1}{f_{sky}(2\ell + 1)} \sum_{m=-\ell}^{\ell} \langle f_{\ell m}^{PSi} f_{\ell m}^{PSj*} \rangle, \quad (4.32)$$

where we defined $f_{sky} = (4\pi)^{-1} \int d\Omega W^2$. The second equality in Eq. (4.32) follows from simplifying the denominator in light of the addition theorem (A.7). The reason for defining this modified formula is that when $\ell \gg 1$ and $m \sim \ell$, the $Y_{\ell m}$ are very small at high latitude, and they give maximum weight to objects at low latitude. Since the small values of $Y_{\ell m}$ are compensated by the small values of $J_{\ell m}$ in Eq. (4.31), it would be unwise to give the $m \sim \ell$ multipoles the same weight as the ones with low m , as it would concentrate weights at low latitude. Further discussion can be found in (Peebles, 1973). Equation (4.32) is referred to as the Peebles modified weighted formula.

4.2.3 The mixing matrix

We have seen that the pseudo-APS relates to the full sky APS through (4.30). However, we want to simplify this equation in order to derive a more explicit formula. Let us start writing the projection operator in terms of the Wigner symbols. Expanding the mask in Spherical Harmonics ($W(\hat{n}) = \sum_{\ell m} I_{\ell m} Y_{\ell m}(\hat{n})$), and solving the Gaunt integral (A.10), we find

$$\begin{aligned} D_{\ell_1 m_1, \ell_2 m_2} &= \sum_{\ell_3 m_3} I_{\ell_3 m_3} \int d\Omega Y_{\ell_1 m_1}(\Omega) Y_{\ell_1 m_1}^*(\Omega) Y_{\ell_3 m_3}(\Omega) \\ &= \sum_{\ell_3 m_3} I_{\ell_3 m_3} (-1)^{-m_2} \left[\frac{(2\ell_1 + 1)(2\ell_3 + 1)(2\ell_3 + 1)}{4\pi} \right]^{1/2} \\ &\quad \times \begin{pmatrix} \ell_1 & \ell_2 & \ell_3 \\ 0 & 0 & 0 \end{pmatrix} \begin{pmatrix} \ell_1 & \ell_2 & \ell_3 \\ m_1 & -m_2 & m_3 \end{pmatrix}. \end{aligned} \quad (4.33)$$

We can replace Eq. (4.33) into Eq. (4.30), getting

$$\begin{aligned} S_{\ell_1}^{ij} &= \sum_{\ell_2} \frac{2\ell_2 + 1}{4\pi} C_{\ell_2}^{ij} \sum_{\ell_3, m_3, \ell_4, m_4} I_{\ell_3 m_3} I_{\ell_4 m_4} [(2\ell_3 + 1)(2\ell_4 + 1)]^{1/2} \\ &\quad \times \begin{pmatrix} \ell_1 & \ell_2 & \ell_3 \\ 0 & 0 & 0 \end{pmatrix} \begin{pmatrix} \ell_1 & \ell_2 & \ell_4 \\ 0 & 0 & 0 \end{pmatrix} \sum_{m_1 m_2} \begin{pmatrix} \ell_1 & \ell_2 & \ell_3 \\ m_1 & -m_2 & m_3 \end{pmatrix} \begin{pmatrix} \ell_1 & \ell_2 & \ell_4 \\ m_1 & -m_2 & m_3 \end{pmatrix} \end{aligned} \quad (4.34)$$

This equation can be simplified using the orthogonality of the Wigner 3-j symbols (A.12) and the mask APS (4.26). Therefore, the final expression reads

$$S_{\ell_1}^{ij} = R_{\ell_1 \ell_2} C_{\ell_2}^{ij}, \quad (4.35)$$

where

$$R_{\ell_1 \ell_2} \equiv \frac{(2\ell_2 + 1)}{4\pi} \sum_{\ell_3} \mathcal{W}_{\ell_3} \begin{pmatrix} \ell_1 & \ell_2 & \ell_3 \\ 0 & 0 & 0 \end{pmatrix}^2. \quad (4.36)$$

The method for including the partial sky in the APS constitutes of multiplying (convolving) it by the *mixing matrix* defined in equation (4.36), which contains the information of the mask function through its power spectrum. Equation (4.35) is a non-local relation in Harmonic space, so the multipoles are no longer independent for the pseudo-APS.

Renormalization revisited

One should note that the mixing matrix (4.36) was derived from the non-renormalized pseudo-APS. However, if we start from (4.32) instead, it is easy to see that the mixing matrix absorbs the f_{sky} factor

$$\tilde{R}_{\ell_1 \ell_2} \equiv \frac{1}{f_{sky}} R_{\ell_1 \ell_2} = \frac{(2\ell_2 + 1)}{4\pi f_{sky}} \sum_{\ell_3} \mathcal{W}_{\ell_3} \begin{pmatrix} \ell_1 & \ell_2 & \ell_3 \\ 0 & 0 & 0 \end{pmatrix}^2. \quad (4.37)$$

Nevertheless, if we start from (4.31), i.e. the *non*-modified weighted formula, we can no longer apply the orthonormality of Wigner Symbols in the previous steps, and the expression of the Mixing Matrix gets a bit more complicated. This alternative derivation can be found in (Postiglione, 2017). Several authors (e.g: Blake, Ferreira and Borrill, 2004; Blake et al., 2007; Thomas, Abdalla and Lahav, 2011b) use, however, the mixing matrix (4.37) together with definition (4.31). As observed by (Postiglione, 2017), Eq. (4.37) should be seen, in that case, as an approximated rather than an exact solution. Nonetheless, this possible inconsistency is solved if one decides to use the Peebles modified weighted formula.

4.3 Pseudo-APS estimate

The APS defined in (4.7), and therefore the pseudo-APS $\tilde{S}_\ell^{ij} = \tilde{R}_{\ell \ell'} C_{\ell'}^{ij}$, are quantities defined by an ensemble average. We call pseudo-APS estimate a quantity that can be defined for a single

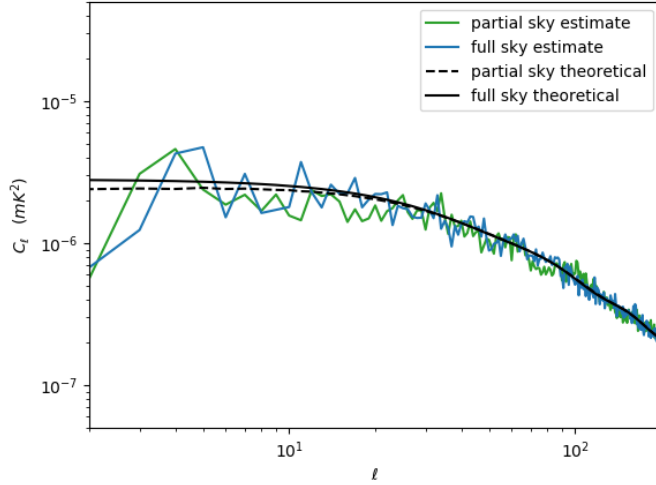


FIGURE 4.5: Comparison between theoretical (pseudo) APS and the measured (pseudo) APS estimate. The full sky theoretical one corresponds to the dashed line of figure (4.2) and the partial sky theoretical one was convolved with the mixing matrix shown in figure (4.4). The estimates were computed with the PseudoPower code on simulations created with the FLASK code.

realization, and its ensemble average is expected to follow its theoretical counterpart. Starting from definition (4.32), we shall define the estimate as

$$\hat{S}_\ell^{ij} = \frac{1}{(2\ell + 1)f_{sky}} \sum_{m=-\ell}^{\ell} |d_{\ell m}^i d_{\ell m}^{j*}| , \quad (4.38)$$

where

$$d_{\ell m} = \sum_p \Delta\Omega_p Y_{\ell m}^*(p) d(p) . \quad (4.39)$$

Here, we are considering the data written on a pixelated sphere. $d(p)$ stands for the data at pixel p , and $Y_{\ell m}(p)$ is the Harmonic computed for the coordinates of the centre of the pixel. In our work, we use HEALPIX (Gorski et al., 2005) to process data on the pixelated sphere.

Furthermore, one may also define a full sky APS estimate \hat{C}_ℓ^{ij} for data available on the whole sphere. It can be seen as the particular case of the partial sky problem, for which $f_{sky} = 1$.

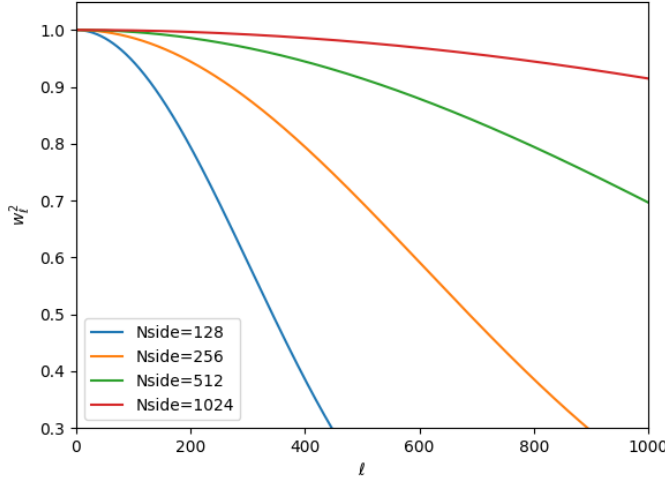


FIGURE 4.6: The pixel window function squared for some values of N_{side} , computed with HEALPix library. It decreases more quickly for lower resolutions.

4.3.1 The pixel window function

Since high ℓ means small scales, we expect pixelation to affect the shape of the spectrum in high multipoles. The pixel window function is a tool for correcting this effect.

Looking at Eq. (4.39), we see that we had to assume that the Spherical Harmonic is constant over the area of the pixel. Therefore, the $d_{\ell m}$ is biased by

$$w_{\ell m}^p = \frac{\int_p d\Omega Y_{\ell m}(\hat{\mathbf{n}})}{\Delta\Omega_p Y_{\ell m}(p)} \quad (4.40)$$

Averaging over p, m in quadrature, we get

$$w_{\ell}^2 = \frac{\sum_{p,m} |w_{\ell m}^p|^2}{N_{\text{pix}}(2\ell + 1)}. \quad (4.41)$$

Equation (4.41) defines what we call a pixel window function. It can be computed directly with HEALPix (read the HEALPix manual¹ for more details). In figure 4.6, we plot w_{ℓ}^2 for some values of N_{side} , a HEALPix resolution parameter that relates to the number of pixels by $N_{\text{pix}} = 12N_{\text{side}}^2$.

¹<https://healpix.sourceforge.io/>

In order to remove the pixelation effect, we should divide the (pseudo-)APS estimate by w_ℓ^2 , in such a way that the corrected estimate reads

$$\hat{S}_\ell^{ij} = \frac{1}{w_\ell^2(2\ell+1)f_{sky}} \sum_{m=-\ell}^{\ell} |d_{\ell m}^i d_{\ell m}^{j*}| . \quad (4.42)$$

4.3.2 Generalizing the estimate for fields with non-zero mean

We have, so far, implicitly assumed a field with zero-mean, i.e. $\langle f(\hat{\mathbf{n}}) \rangle = 0$. The full-sky APS is, for $\ell > 0$, independent of the field's mean. However, we should be careful about this in the partial sky case. Equation (4.42), for instance, is dependent of the field's mean due to the presence of the masked points. Therefore, this equation should be only applied to zero-mean fields. If we are dealing with fields that have a non-zero mean, e.g. galaxy counts, we can either transform them to a zero-mean field or use an estimate which is unbiased with respect to the mean. In this section we are going to formulate this estimate. The discussion here is mainly adapted from (Peebles, 1973).

Let $f(\hat{\mathbf{n}})$ be a cosmological field. If $f(\hat{\mathbf{n}})$ is isotropic, then $\langle f(\hat{\mathbf{n}}) \rangle$ is constant. Denoting $\mathcal{N} = \langle f(\hat{\mathbf{n}}) \rangle$, the ensemble average of the Spherical Harmonics expansion coefficients (4.20) is

$$\langle f_{\ell m} \rangle = (4\pi)^{1/2} \mathcal{N} \delta_{\ell 0} . \quad (4.43)$$

However, averaging equation (4.21) yields

$$\langle f_{\ell m}^{PS} \rangle = \sum_{\ell' m'} D_{\ell m, \ell' m'} \langle f_{\ell' m'} \rangle = \mathcal{N} I_{\ell m} . \quad (4.44)$$

Therefore, the following quantity is unbiased with respect to \mathcal{N}

$$h_{\ell m} = f_{\ell m}^{PS} - \mathcal{N}_a I_{\ell m} . \quad (4.45)$$

Here, we replaced the ensemble average \mathcal{N} by the average over the surface \mathcal{N}_a , given by

$$\mathcal{N}_a = \frac{N_a}{\Delta\Omega} = \frac{\sqrt{4\pi} f_{00}^{PS}}{\Delta\Omega} , \quad (4.46)$$

where

$$N_a = \int_{\Omega} d\Omega W(\hat{\mathbf{n}}) f(\hat{\mathbf{n}}) \quad \Delta\Omega = \int_{\Omega} d\Omega W(\hat{\mathbf{n}}) . \quad (4.47)$$

Moreover, we can find that it relates to the full sky Spherical Harmonics coefficients by

$$h_{\ell m} = \sum_{\ell' m'} K_{\ell m, \ell' m'} f_{\ell' m'} \quad \text{where} \quad K_{\ell m, \ell' m'} = D_{\ell m, \ell' m'} - \frac{I_{\ell m} I_{\ell' m'}}{\Delta\Omega}, \quad (4.48)$$

therefore,

$$\langle h_{\ell m} h_{\ell m}^* \rangle = \sum_{p, q, p', q'} K_{\ell m, pq} K_{\ell m, p' q'}^* \langle f_{pq} f_{p' q'}^* \rangle = \sum_{p, q} |K_{\ell m, pq}|^2 C_p. \quad (4.49)$$

Thus, we can check how it affects the renormalization. We see that an extra factor appears, but it is negligible if the survey covers an appreciable part of the sky,

$$\begin{aligned} \sum_{p, q} |K_{\ell m, pq}|^2 &= \sum_{p, q} |D_{\ell m, pq}|^2 + \frac{|I_{\ell m}|^2}{\Delta\Omega^2} \sum_{p, q} |I_{pq}|^2 - \sum_{p, q} \frac{1}{\Delta\Omega} [D_{\ell m, pq} I_{\ell m} I_{pq} + D_{pq, \ell m} I_{pq} I_{\ell m}] \\ &= J_{\ell m} - 2 \frac{|I_{\ell m}|^2}{\Delta\Omega} + \frac{|I_{\ell m}|^2}{\Delta\Omega} = J_{\ell m} \left[1 + \frac{|I_{\ell m}|^2}{\Delta\Omega J_{\ell m}} \right] \approx J_{\ell m}. \end{aligned} \quad (4.50)$$

Therefore, the pseudo-APS estimate can be generalized for a non-zero mean field by

$$\hat{S}_{\ell}^{ij} = \frac{1}{w_{\ell}^2 (2\ell + 1)} \sum_{m=-\ell}^{\ell} \frac{|(d_{\ell m}^i - \mathcal{N}_a I_{\ell m})(d_{\ell m}^{j*} - \mathcal{N}_a I_{\ell m})|}{J_{\ell m}}. \quad (4.51)$$

Moreover, the Peebles modified weighting formula becomes

$$\hat{S}_{\ell}^{ij} = \frac{1}{w_{\ell}^2 (2\ell + 1) f_{sky}} \sum_{m=-\ell}^{\ell} |(d_{\ell m}^i - \mathcal{N}_a I_{\ell m})(d_{\ell m}^{j*} - \mathcal{N}_a I_{\ell m})|. \quad (4.52)$$

4.4 Building a covariance

The covariance matrix is a key point to estimate the uncertainties of the observables and further estimating the cosmological parameters. In our case, the observables are the APS of HI Intensity Maps. Building a covariance requires a huge number of simulations. If \hat{S}_{ℓ}^{ij} is the APS measured for each simulation, the covariance of a set of N_s simulations is

$$\mathcal{C}_{\ell \ell'}^{ij} = \frac{1}{N_s - 1} \sum_{s=1}^{N_s} \left(\hat{S}_{\ell}^{ij} - \langle \hat{S}_{\ell}^{ij} \rangle \right) \left(\hat{S}_{\ell'}^{ij} - \langle \hat{S}_{\ell'}^{ij} \rangle \right)^T. \quad (4.53)$$

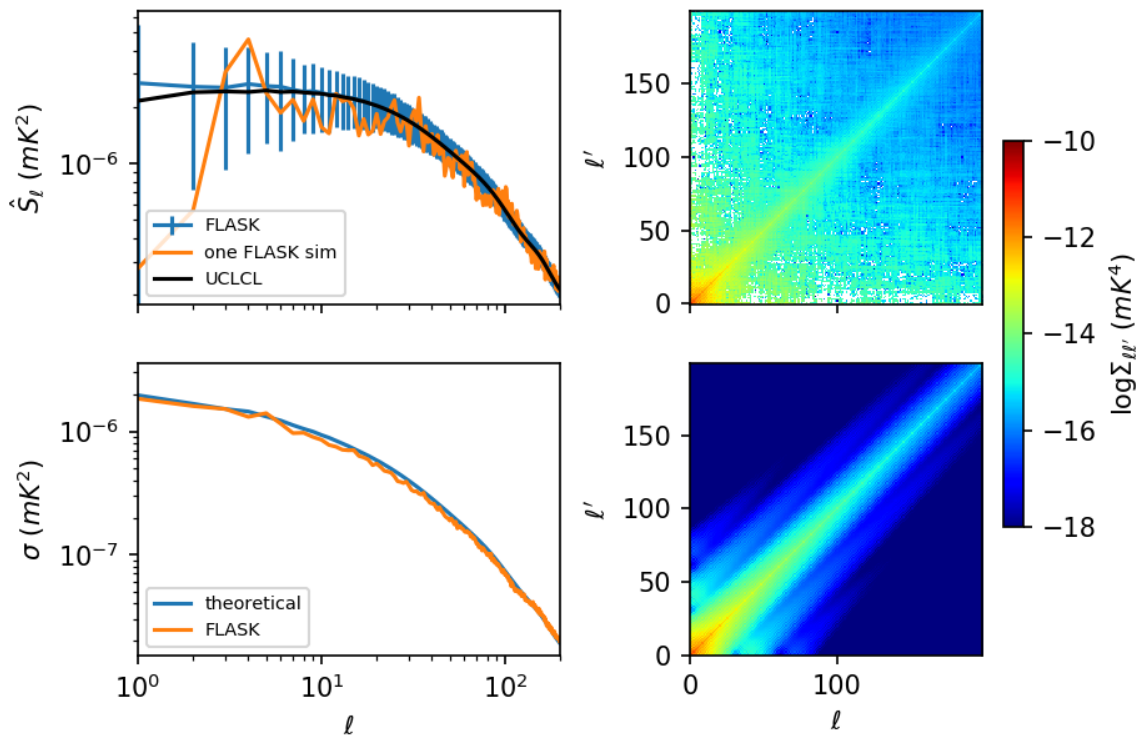


FIGURE 4.7: This figure shows the consistency of the FLASK simulations with respect to the theoretical pseudo-APS and to the theoretical covariance for one of the BINGO channels (965MHZ). Upper left: In blue, average and variance (error-bars) of 500 FLASK simulations. The error bars are given by the variance $\sigma(\ell) = \sqrt{\Sigma_{\ell\ell}}$. In yellow, one of those simulations, and in black, the theoretical UCLCL convolved with the BINGO mixing matrix. Lower left: comparison between FLASK variance and theoretical variance. Upper right: the FLASK covariance. Lower right: the theoretical covariance.

4.4.1 Lognormal covariance

It is a common practice in cosmology to simulate the fields related to the Large Scale Structure as multivariate lognormal variables. This distribution model is more suitable to describe matter tracers than, for instance, the Gaussian distribution, avoiding non-physical ($\delta < -1$) densities. In our work, we compute a lognormal covariance from 500 realizations. The covariance for a typical BINGO channel can be seen in figure (4.7, upper right) and comparison with UCLCL can be seen in figure (4.7, upper left). Below, we provide a description of the FLASK code, used for computing the lognormal simulations.

FLASK code description

The Full-sky Lognormal Astro-fields Simulation Kit (FLASK) (Xavier, Abdalla and Joachimi, 2016) is a publicly available code able to produce two-dimensional tomographic realizations (spherical shells around the observer, positioned at the center) of an arbitrary number of random astrophysical fields, reproducing the desired cross-correlations between them. Such realizations can follow not only a multivariate Gaussian distribution, but also, and specially, a multivariate lognormal distribution, the latter being more appropriate to reproduce the behaviour of matter and tracer density fields.

FLASK takes as input the angular auto- and cross-APS, C_ℓ^{ij} , previously calculated for each of the i and j fields and redshift slices aimed for the code to simulate. The process for simulating lognormal fields consists of first generating Gaussian fields and then taking the exponential. First of all, FLASK takes the input $C_{\ln,\ell}^{ij}$, and computes the APS $C_{g,\ell}^{ij}$ of the associated Gaussian variables (2.137). Then, it performs a Cholesky decomposition in lower triangular matrices

$$C_{g,\ell}^{ij} = \sum_k T_{ik,\ell} T_{jk,\ell}. \quad (4.54)$$

One should notice that although multipoles with different ℓ and m are independent, multipoles with the same ℓ and m , but for different fields or redshift slices, may be correlated. The above decomposition allows the code to generate correlated Gaussian variables as a combination of independent Gaussian variables $Z_{k,\ell m}^0$ of zero mean and unit variance

$$Z_{i,\ell m} = \sum_k T_{ik}(\ell) Z_{k,\ell m}^0, \quad (4.55)$$

satisfying

$$\langle Z_{i,\ell m} Z_{j,\ell' m'} \rangle = C_{g,\ell}^{ij}. \quad (4.56)$$

Moreover, it is worth mentioning that such decomposition is only possible if the matrix $C_{g,\ell}^{ij}$ is positive-definite, i.e. all eigenvalues are non-negative. If it is not, FLASK handles this problem by introducing small deviations such that it becomes positive-definite. This process is called regularization. The two methods of regularization implemented on FLASK are

1. To set the negative eigenvalues to zero;
2. To apply successive fractional changes to the elements of the matrix in the $N \times N$ -dimensional direction of the greatest change in the negative eigenvalues. In other words, in the direction of the gradient of the negative eigenvalues' sum.

Notice that this problem can appear in the $C_{g,\ell}^{ij}$ calculated, even though the original $C_{ln,\ell}^{ij}$ is positive-definite, possibly due to numerical errors or fundamental limitations associated to the modeling of correlated data by lognormal variables (a detailed explanation is found in Xavier, Abdalla and Joachimi, 2016).

Finally, the lognormal maps are generated from the Gaussian ones by the local transformation,

$$X_i(\hat{\mathbf{n}}) = e^{\mu_i} e^{Z_i(\hat{\mathbf{n}})} - \lambda_i, \quad (4.57)$$

where the μ_i and σ_i are computed by

$$\sigma_i^2 = \sum_{\ell_{min}}^{\ell_{max}} \frac{2\ell+1}{4\pi} C_{g,\ell}^{ii}, \quad (4.58)$$

$$e^{\mu_i} = (\langle X_i \rangle + \lambda_i) e^{-\sigma_i^2/2}. \quad (4.59)$$

4.4.2 Theoretical covariance

In this section, we follow the formalism presented in (Dahlen and Simons, 2008; Loureiro et al., 2019) to show how we can model, under some assumptions, the APS covariance from a purely theoretical perspective. A theoretical model of covariance is useful for comparison with the data covariance and, therefore, allows us to validate our analysis of parameter estimation. Any method for building a covariance, e.g. FLASK or others, is susceptible to errors intrinsic to the algorithm used to generate realizations. It is then helpful to compare the different approaches

and cross-check the results. Moreover, the theoretical model is helpful to explain the physics of the covariance matrix, for instance, the amplitude of the mixed modes.

We shall introduce to the reader the so called *pixel basis representation*. Any function $f(\hat{\mathbf{n}})$ over a region of the sphere is, in this representation, given by an N_{pix} -dimensional column vector $\mathbf{f} = (f_1, \dots, f_{N_{pix}})^T$, where N_{pix} is the total number of equally sized pixels in which the mask does not vanish, and $f_i = f(\hat{\mathbf{n}}_i)$ is the value of \mathbf{f} at pixel i .

Let us recall that the auto-APS estimate in spatial basis is

$$\begin{aligned}\hat{S}_\ell &= \frac{1}{f_{sky}(2\ell+1)} \sum_m \left| \int d\Omega d(\hat{\mathbf{n}}) Y_{\ell m}^*(\hat{\mathbf{n}}) \right|^2 \\ &= \frac{1}{f_{sky}(2\ell+1)} \int d\Omega d\Omega' d^*(\hat{\mathbf{n}}) d(\hat{\mathbf{n}}') \sum_m Y_{\ell m}(\hat{\mathbf{n}}) Y_{\ell m}^*(\hat{\mathbf{n}}') ,\end{aligned}\quad (4.60)$$

where $d(\hat{\mathbf{n}})$ denotes the data as a function of the angular position $\hat{\mathbf{n}}$, and the integral is performed over the mask. In pixel basis representation, this becomes

$$\hat{S}_\ell = \frac{\Delta\Omega_p^2}{f_{sky}(2\ell+1)} \mathbf{d}^T \mathbf{P}_\ell \mathbf{d} ,\quad (4.61)$$

where we defined, in pixel space, the matrix \mathbf{P}_ℓ , of size $N_{pix} \times N_{pix}$ and elements given by

$$[\mathbf{P}_\ell]_{ij} = \sum_m Y_{\ell m}(\hat{\mathbf{n}}_i) Y_{\ell m}^*(\hat{\mathbf{n}}_j) ,\quad (4.62)$$

and $\Delta\Omega_p$ is the area of the pixel. Denoting $\text{cov}(x_1, x_2) = \langle x_1 x_2 \rangle - \langle x_1 \rangle \langle x_2 \rangle$, the APS covariance reads

$$\Sigma_{\ell\ell'} = \frac{\Delta\Omega_p^4}{f_{sky}^2(2\ell+1)(2\ell'+1)} \text{cov}(\mathbf{d}^T \mathbf{P}_\ell \mathbf{d}, \mathbf{d}^T \mathbf{P}_{\ell'} \mathbf{d}) .\quad (4.63)$$

This equation can be simplified using an identity due to (Isserlis, 1916), which holds assuming Gaussian variables:

$$\text{cov}(d_1 d_2, d_3 d_4) = \text{cov}(d_1, d_3) \text{cov}(d_2, d_4) + \text{cov}(d_1, d_4) \text{cov}(d_2, d_3) .\quad (4.64)$$

Therefore, the APS covariance becomes

$$\Sigma_{\ell\ell'} = \frac{\Delta\Omega_p^4}{f_{sky}^2(2\ell+1)(2\ell'+1)} 2 \text{tr}(\mathbf{C} \mathbf{P}_\ell \mathbf{C} \mathbf{P}_{\ell'}) .\quad (4.65)$$

The factor of 2 arises because the two terms in the right-hand side of Isserlis identity are, in our case, identical. Since the physical data cannot be truly Gaussian, we should understand this step as an approximation to Gaussian fields.

Moreover, we should notice that the real space covariance $\mathbf{C} = \text{cov}(\mathbf{d}^T, \mathbf{d})$ can be decomposed in terms of the \tilde{S}_ℓ using the \mathbf{P}_ℓ matrix,

$$C_{ij} = \sum_{\ell, m, \ell', m'} \langle d_{\ell m} d_{\ell' m'}^* \rangle Y_{\ell m}(\hat{\mathbf{n}}_i) Y_{\ell' m'}^*(\hat{\mathbf{n}}_j) = \sum_{\ell, m} \tilde{S}_\ell Y_{\ell m}(\hat{\mathbf{n}}_i) Y_{\ell m}^*(\hat{\mathbf{n}}_j) \Rightarrow \quad (4.66)$$

$$\mathbf{C} = \sum_\ell \tilde{S}_\ell \mathbf{P}_\ell. \quad (4.67)$$

Replacing eq. (4.67) in eq. (4.65), we find

$$\Sigma_{\ell\ell'} = \frac{2\Delta\Omega_p^4}{f_{sky}^2 (2\ell+1)(2\ell'+1)} \sum_{\ell'', \ell'''} \tilde{S}_{\ell''} \tilde{S}_{\ell'''} \sum_{i,j,k,h}^{N_{pix}} [\mathbf{P}_\ell]_{ij} [\mathbf{P}_{\ell''}]_{jk} [\mathbf{P}_{\ell''''}]_{kh} [\mathbf{P}_{\ell'}]_{hi} \quad (4.68)$$

$$= \frac{2}{f_{sky}^2 (2\ell+1)(2\ell'+1)} \sum_{\ell'', \ell'''} \tilde{S}_{\ell''} \tilde{S}_{\ell'''} \sum_{m,m',m'',m'''} D_{\ell m, \ell' m'} D_{\ell' m', \ell''' m'''} D_{\ell''' m''', \ell'' m''} D_{\ell'' m'', \ell' m'}. \quad (4.69)$$

In the step between equations (4.68) and (4.69) we should transform from pixel basis back to spatial basis, in such a way that the sums over the pixels become four integrals over the surface, and we apply the definition of the projection operator.

The full sky case yields $D_{\ell m, \ell' m'} = \delta_{\ell m, \ell' m'}$, and we find a quite simple solution,

$$\Sigma_{\ell\ell'}^{FS} = \frac{2\delta_{\ell,\ell'}}{(2\ell+1)^2} C_\ell^2 \sum_{m,m'} \delta_{m,m'} = \frac{2\delta_{\ell,\ell'}}{(2\ell+1)} C_\ell^2. \quad (4.70)$$

The partial sky case, however, is a bit more complicated to solve, since the $\tilde{S}_{\ell''} \tilde{S}_{\ell'''}$ term does not come out of the sum. We shall, then, assume a moderately colored spectra, such that $\tilde{S}_{\ell''} \approx \tilde{S}_{\ell'''} \approx \sqrt{\tilde{S}_\ell \tilde{S}_{\ell'}}$. This approximation is better for a larger non-masked area (i.e. higher f_{sky}) than for a smaller area, since a larger area means a weaker coupling with the mask. We are also neglecting the effect of a weight in the mask, i.e. it is a non-binary mask. Thus, we can

simplify the projection operator terms. With these assumptions, the covariance becomes

$$\Sigma_{\ell\ell'} = \frac{2}{f_{sky}^2 (2\ell + 1) (2\ell' + 1)} \tilde{S}_\ell \tilde{S}_{\ell'} \sum_{m,m'} |D_{\ell m, \ell' m'}|^2 \quad (4.71)$$

$$= \frac{2\tilde{R}_{\ell\ell'}}{f_{sky} (2\ell' + 1)} \tilde{S}_\ell \tilde{S}_{\ell'} . \quad (4.72)$$

Expression (4.72), derived for auto-APS, can be generalized for cross-APS by replacing $\tilde{S}_\ell \tilde{S}_{\ell'} \rightarrow (\tilde{S}_\ell^{ij} \tilde{S}_{\ell'}^{ij} + \tilde{S}_\ell^{ii} \tilde{S}_{\ell'}^{jj}) / 2$ (Rassat et al., 2007). Moreover, if we want to include noise and pixel window function, we should also replace $\tilde{S}_\ell^{ij} \rightarrow D_\ell^{ij} = w_\ell^2 \tilde{S}_\ell^{ij} + \delta_{ij} N_\ell$ (Loureiro et al., 2019), and the final expression of the theoretical covariance should read

$$\Sigma_{\ell\ell'}^{ij} = \frac{\tilde{R}_{\ell\ell'}}{f_{sky} (2\ell' + 1)} \left[(w_\ell^2 \tilde{S}_\ell^{ij} + \delta_{ij} N_\ell) (w_{\ell'}^2 \tilde{S}_{\ell'}^{ij} + \delta_{ij} N_{\ell'}) + (w_\ell^2 \tilde{S}_\ell^{ii} + \delta_{ii} N_\ell) (w_{\ell'}^2 \tilde{S}_{\ell'}^{jj} + \delta_{jj} N_{\ell'}) \right] . \quad (4.73)$$

Although in full sky the multipoles are uncorrelated, i.e. the off-diagonal terms vanish in Eq. (4.72), in partial sky the $\tilde{R}_{\ell\ell'}$ term appears as a coupling term between the multipoles, and the covariance is no longer diagonal.

Figure (4.7 lower right) shows the theoretical covariance computed by the implementation of equation (4.73) for the noiseless case. This covariance is not identical to the FLASK data covariance (4.7 upper right) mostly in the areas away from the main diagonal. This discrepancy is reasonable given the limitations of the theoretical modeling, such as the Gaussian assumptions, since our FLASK simulations follow a Lognormal distribution. The consistency of both covariances in the main diagonal is confirmed in figure (4.7 lower left).

Chapter 5

Cosmological parameter estimation

In this chapter we apply the tools discussed in the previous chapter (e.g. APS estimate, APS covariance) to a Monte Carlo algorithm in order to place constraints in the cosmological parameters. In section 5.1 we explain the HIR4 mocks of the Intensity Mapping signal from which we extract the APS estimate, and we aim to recover the cosmological parameters. In section 5.2 we present the Monte Carlo algorithm based on the *nested sampling* method. Then, in section 5.3 we show the results of the parameter estimation.

5.1 HIR4 mock description

Besides FLASK lognormal simulations, a more realistic way of generating HI Intensity Maps is through N-body simulations. The HI maps simulated using N-body simulations are more precise, especially in small scales, for describing non-linearities in the formation of the Large Scale Structures and affect the *Finger-of-God* in RSD (Redshift Space distortion). The technique consists in populating HI mass in dark matter halos of the N-body *Horizon-Run 4* (HR4) simulation. Since the computational cost of generating such simulations with the appropriate resolution is very high, this method is less convenient for covariance building. In our work, we use the HIR4 mocks as the data for the Monte Carlo fitting and constraining of the cosmological parameters, while using FLASK lognormal realizations for the covariance matrix estimation. This section provides a brief description of the HIR4 mock building. A detailed explanation can be found in (Zhang, Motta, Novaes et al., 2021).

Horizon Runs (HRs) is a series of massive N-body and hydrodynamic simulations developed for studying cosmology, galaxy evolution and formation, and evolution of the Large Scale Structure. We used the 4th release, the *Horizon Run 4* (Kim et al., 2015), which used 6300^3 particles gravitating in a box of size $3150h^{-1}Mpc$. They adopted a WMAP5 Λ -CDM cosmology, where $\Omega_m = 0.26$, $\Omega_\Lambda = 0.74$, $\sigma_8 = 0.79$ and $n_s = 0.96$. These values were chosen probably by

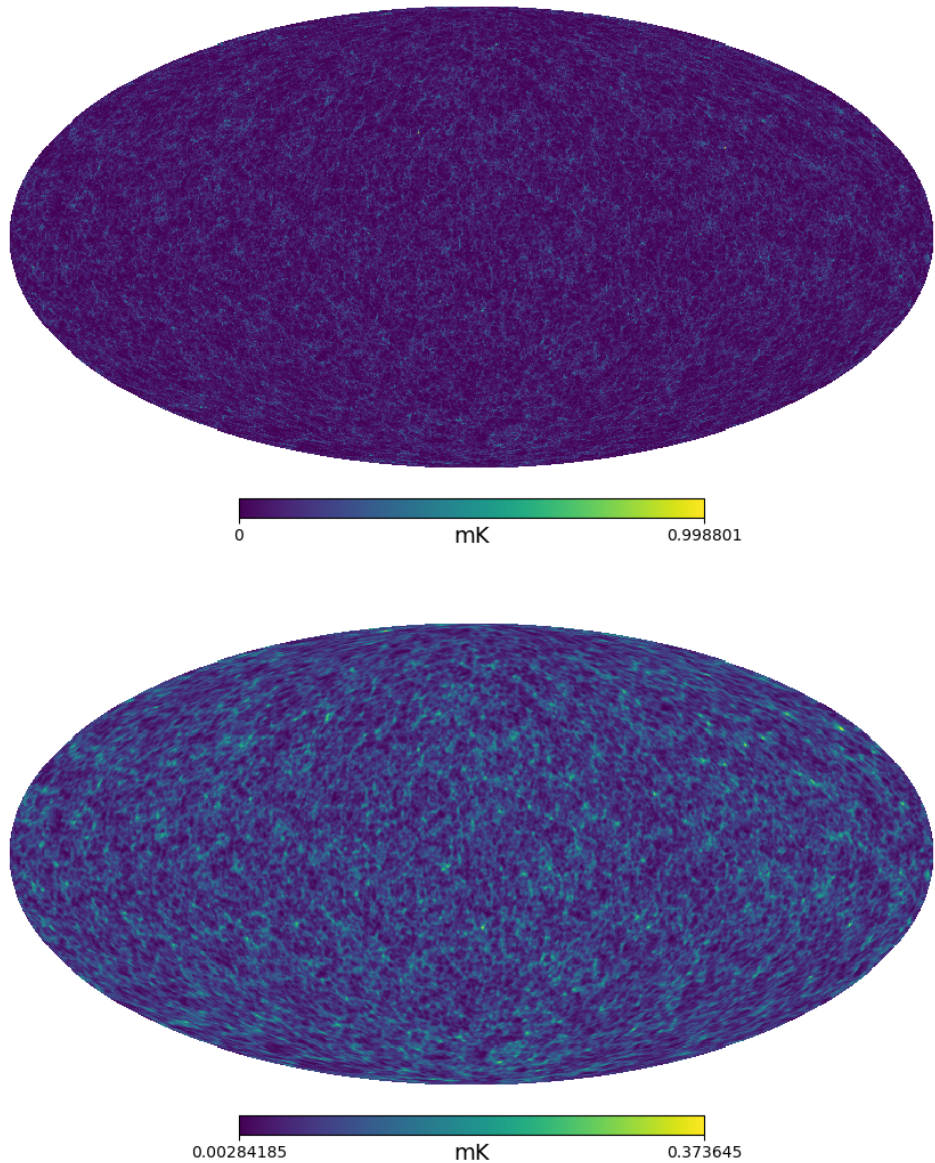


FIGURE 5.1: Top: HIR4 mock for one of the BINGO channels, $\nu = 965\text{MHz}$, $\Delta\nu = 10\text{MHz}$, computed for the HOD distribution. Bottom: The same situation, but after convolving with a Gaussian kernel FWHM = 40 arcmin, in order to mimic the BINGO beam.

historical reasons, since they are outdated compared to the recent Planck constraints. However, this is the cosmology we should recover when applying a Monte Carlo method on the mocks.

In summary, there are three steps in the construction of the mock map:

1. To populate HI gas in the galaxy (halo) catalog and to calculate the HI density distribution ρ , using either Abundance Matching or the HOD model;
2. To transform the density map into a brightness temperature map by

$$T_b(\hat{\mathbf{n}}, z) = 189h \frac{H_0(1+z)^2}{H(z)} \frac{\rho_{HI}(\hat{\mathbf{n}}, z)}{\rho_c} \text{mK}, \quad (5.1)$$

where ρ_c is the critical density of the Universe (Villaescusa-Navarro et al., 2018);

3. To smooth the brightness temperature map with a Gaussian kernel FWHM = 40 arcmin, which is due to the BINGO's beam.

Abundance Matching

Halo Abundance Matching (HAM) and Sub-Halo Abundance Matching (SHAM) are widely used methods for linking dark halos to galaxies in observations. Here, we use an Abundance Matching method to link HI mass to galaxies. The HI is allocated to the HR4 galaxies, according to the HI mass function, measured from the ALFALFA catalog (Martin et al., 2010),

$$\phi(m_{HI}) = \frac{dn}{d \log_{10}(m_{HI})} = \ln(10)\phi_* \left(\frac{m_{HI}}{m_*}\right)^{\alpha+1} \exp\left(-\frac{m_{HI}}{m_*}\right) , \quad (5.2)$$

where

$$\phi_* = 0.0048 , \quad (5.3)$$

$$\alpha = -1.33 , \quad (5.4)$$

$$m_* = 10^{9.96} \left(\frac{0.7}{h}\right)^2 , \quad (5.5)$$

and m_{HI} is the HI mass in unities of M_\odot/h and $n = n(m_{HI})$ is the number of galaxies hosting a mass m_{HI} of HI. Equation (5.2) gives the galaxy distribution in terms of the hosted HI mass. The galaxy catalog is the one developed by (Hong, Park and Kim, 2016). All the catalog is sorted by mass, so the larger galaxies (in mass) receive the higher amount of HI. Then, the catalog is sliced in 30 redshift bins in the BINGO range, the HI density is computed using the

HEALPix pixelation scheme (Gorski et al., 2005) in $N_{side} = 256$. Finally, the HI density is transformed into brightness temperature (5.1).

One problem about this approach of Abundance Matching is that equation (5.2) was fitted from ALFALFA catalog at redshift $z = 0$, while we are applying it to the redshift range of 0.13 to 0.48. Moreover, it has some limitations, like the assumption that the HI mass is an increasing function with respect to the galaxy mass, the difficulty of measuring the $b_{HI}(z)$ in this model, and the fact that it requires a galaxy catalog instead of just a halo catalog.

Halo Occupation Distribution (HOD)

In this approach, we link the HI mass to the HR4 dark halos according to the mass of the host halos. We use a formula fitted from the ELUCID SAM catalog (Wang et al., 2016b):

$$\log_{10}(m_{HI}) = a \log_{10}(m) + b + ce^{-(\log_{10}(m)-d)^2/f^2}, \quad (5.6)$$

$$a = 0.78 - 0.030z, \quad (5.7)$$

$$b = -0.23 + 0.68z, \quad (5.8)$$

$$c = 0.92 - 0.32z, \quad (5.9)$$

$$d = 11 + 0.038z, \quad (5.10)$$

$$f = 0.79 + 0.18z, \quad (5.11)$$

where z is the redshift, m_{HI} is the HI mass in unities of M_\odot/h , and m is the halo mass in unities of M_\odot/h . Then, the catalog is sliced in 30 bins, pixelated with HEALPix in $N_{side} = 256$ and transformed from HI overdensity into brightness temperature. In this model, the bias can be measured directly from the mocks by the weighted average of the halo bias

$$b_{HI}(z) = \frac{\int dm n(m, z)m_{HI}(m, z)b(m, z)}{\int dm n(m, z)m_{HI}(m, z)}. \quad (5.12)$$

The halo bias $b(m, z)$ can be calculated by empirical formula calibrated by N-body simulations (Tinker et al., 2010). The bias computed by eq. (5.12) will be referred by us as the true value when compared to what is measured with the Monte Carlo methods. In figure (5.1), we show an example of a mock map build using the HOD model.

5.2 Parameter estimation algorithm

5.2.1 Bayesian statistics

Bayesian statistics is a common framework in cosmology and astrophysics to tackle problems of statistical analysis, such as parameter estimation and model selection. Such methods have increased in popularity in the 21st century due to advancements in the availability of high performance computational resources.

At first, we shall mention that Bayesian statistics relies on the Bayes theorem. Given two random variables A and B , let us denote by $P(A)$ the probability of A , and by $P(A|B)$ the conditional probability of A given that B is true. The Bayes theorem states that:

$$P(A|B) = \frac{P(B|A)P(A)}{P(B)}. \quad (5.13)$$

The proof comes from the product rule $P(A, B) = P(A|B)P(B)$, where $P(A, B)$ denotes the joint probability of A and B . Notice that by inverting A and B in this equation, we get $P(B, A) = P(B|A)P(A)$, and because $P(A, B) = P(B, A)$, we can equate the right-hand side of both equations obtaining the result (5.13).

Let us say that we have some observational dataset \mathcal{D} and we wish to estimate a vector of free parameters Θ of the cosmological model. In the language of conditional probability, what we want to find is the distribution of $P(\Theta|\mathcal{D})$. Applying Bayes theorem, we have

$$P(\Theta|\mathcal{D}) = \frac{P(\mathcal{D}|\Theta)P(\Theta)}{P(\mathcal{D})} = \frac{\mathcal{L}(\Theta)\pi(\Theta)}{Z}. \quad (5.14)$$

The methods consist in sampling the parameter space in order to get $P(\Theta|\mathcal{D})$, which is called *posterior distribution*. Then, we need the *prior* probability $\pi(\Theta)$ and the *likelihood* function. The *prior* represents our initial believes of the parameters values, based in previous experiments. It is usually defined as a top-hat function, being equal to 1 inside a fair volume of the parameter space and 0 outside. Therefore, the prior defines the boundaries of the parameter space where the points are sampled. The *likelihood* is the probability of getting our data given that Θ is true. It depends on the covariance matrix, and there is more than one way of modelling it, frequently as a Gaussian function. Finally, we have the *evidence* Z , which normalizes the posterior distribution. It is given by

$$Z = \int \mathcal{L}(\Theta)\pi(\Theta)d\Theta. \quad (5.15)$$

From the posterior distribution one can compute the expected value of the parameters as

$$E[\Theta] = \int \Theta dP(\Theta|\mathcal{D}). \quad (5.16)$$

Other application of Bayesian methods is model selection. Suppose that we have two models \mathcal{M}_1 and \mathcal{M}_2 , and we wish to see which one is more consistent with our dataset. By Bayes theorem,

$$\frac{P(\mathcal{M}_1|\mathcal{D})}{P(\mathcal{M}_2|\mathcal{D})} = \frac{P(\mathcal{D}|\mathcal{M}_1)P(\mathcal{M}_1)}{P(\mathcal{D}|\mathcal{M}_2)P(\mathcal{M}_2)} = \frac{Z_1}{Z_2} \frac{P(\mathcal{M}_1)}{P(\mathcal{M}_2)}. \quad (5.17)$$

If we are considering just one dataset, we can simply impose $\frac{P(\mathcal{M}_1)}{P(\mathcal{M}_2)} = 1$, since there is no reason to favor one model over the other. Then, we see that the ratio Z_1/Z_2 indicates which model is preferred by the dataset: if this ratio is higher (lower) than one, the preferred model is \mathcal{M}_1 (\mathcal{M}_2). Moreover, if we want to take into account more than one dataset, we can put $\frac{P(\mathcal{M}_1)}{P(\mathcal{M}_2)}$ as the evidence ratio from other datasets, then the final value will be the product of the ratios.

5.2.2 UCLCL-PARAM-EST code description

The UCLCL - PARAMETER ESTIMATION (UCLCL-PARAM-EST for short) is a C++ code for cosmological parameter estimation related to the UCLCL library (subsection 4.1.4). The code samples the parameter space seeking the maximum likelihood region, comparing the theoretical APS with the data provided by the user. In summary, for each sampled point the code performs the following steps:

1. Computing of the UCLCL prediction for the APS, for this given set of parameters;
2. Convolution of the theoretical APS with the mixing matrix provided by the user;
3. Binning of the ℓ values of the convolved APS according to the bandwidth of the data. The binning formula is weighted by the number of spherical harmonic coefficients

$$\tilde{S}_b^{ij} = \frac{\sum_{\ell=\ell_0}^{\ell_0+\Delta\ell} (2\ell+1) \tilde{S}_\ell^{ij}}{\sum_{\ell=\ell_0}^{\ell_0+\Delta\ell} (2\ell+1)}; \quad (5.18)$$

4. Computing of the likelihood.

The likelihood can be computed by a few different models by choice of the user. The first one is the Gaussian likelihood

$$\mathcal{L}_G(\Theta) = \frac{1}{\sqrt{|2\pi\mathcal{C}|}} \exp\left(-\frac{1}{2}\chi^2(\Theta)\right), \quad (5.19)$$

where

$$\chi^2(\Theta) = \left[\hat{S}_b - \tilde{S}_b^{th}(\Theta) \right]^T \mathcal{C}^{-1} \left[\hat{S}_b - \tilde{S}_b^{th}(\Theta) \right]. \quad (5.20)$$

Here, \hat{S}_b and \mathcal{C} are the data and covariance matrix previously computed and provided as input, while $\tilde{S}_b^{th}(\Theta)$ is the theoretical spectrum calculated for each sampled point. The next model is a modified version of the Gaussian one, which was proposed by (Anderson, 2003; Hartlap, Simon and Schneider, 2007). They state that the inverse of the covariance is biased by the number of simulations, so it should be corrected by a factor of α in order to de-bias it, that is

$$\mathcal{C}^{-1} \rightarrow \alpha \mathcal{C}^{-1}, \quad \alpha = \frac{N_s - p - 2}{N_s - 1}, \quad (5.21)$$

where N_s is the number of simulations and p is the length of the data vector. Finally, we have the likelihood due to (Sellentin and Heavens, 2015). It is a more recent proposal of de-biasing the Gaussian likelihood. They show that, when the estimate covariance is marginalized over the true covariance, it becomes a t-distribution instead of a Gaussian distribution

$$\begin{aligned} \mathcal{L}_{SH}(\Theta) &= \frac{\bar{c}_p}{|\mathcal{C}|^{1/2}} \left[1 + \frac{\chi^2(\Theta)}{N_s + 1} \right]^{-\frac{N_s}{2}}, \\ \text{where } \bar{c}_p &= \Gamma(N_s/2) / [\pi(N_s - 1)]^{p/2} \Gamma\left(\frac{N_s - p}{2}\right). \end{aligned} \quad (5.22)$$

If the number of simulations is not high enough, let us say, not much higher than p , even the Hartlap rescaling would not be a good approximation, and this model should be preferred.

Pliny: a nested sampling implementation

An efficient sampling method is essential for a Bayesian analysis. *Nested sampling* (Skilling, 2004) is a modern alternative to the classical Monte Carlo Markov Chain (MCMC) methods, like the standard Metropolis–Hastings algorithm and its variants such as Gibbs’ or Hamiltonian sampling. Initially developed for the calculation of the evidence integral, the *nested sampling* method has been proved to be also very powerful for parameter estimation problems (Feroz

and Hobson, 2008). The classical MCMC often becomes inefficient in situations with multimodal posterior distribution, or large (curving) degeneracies between parameters, particularly in high dimensions. UCLCL-PARAM-EST accepts some different implementations of the *nested sampling* algorithm, namely: POLYCHORD (Handley, Hobson and Lasenby, 2015), MULTINEST (Feroz, Hobson and Bridges, 2009) and PLINY (Rollins, 2015). Although the first two are more widely used, we chose to use the third one, which developed a more efficient parallel scheme suitable for high-performance computers.

The *nested sampling* algorithm is based on the concept of *live-points*: a set of points in the parameter space that are treated as an iso-likelihood contour. New points are randomly sampled inside this volume, and then the live-points are iteratively re-defined, traveling through nested likelihood shells, and towards the high-likelihood region. The algorithm starts with an initial set \mathcal{S} of live-points that are randomly chosen in the prior-space. Let \mathcal{L}_* be the critical likelihood, i.e. the minimum likelihood of the live-points, and $\Theta_* \in \mathcal{S}$ the point with $\mathcal{L}(\Theta_*) = \mathcal{L}_*$. A new point Θ is sampled. If it satisfies $\mathcal{L}(\Theta) > \mathcal{L}_*$, it is added to \mathcal{S} , while Θ_* is removed. Also, Θ_* is assigned to a chain \mathcal{C} with its likelihood value and a weight ω corresponding to the change in the remaining prior space. The same procedure is repeated over and over again until some convergence criteria is met. At the end, the chain \mathcal{C} constitutes a fair sample of the parameter space and can be used to infer the evidence and, therefore, the posterior distribution. The evidence integral (5.15) becomes a weighted sum over the chain

$$Z = \sum_{\Theta_i \in \mathcal{C}} \omega_i \mathcal{L}_i, \quad (5.23)$$

where, in Pliny, the weight is given in terms of the step i and the number N of live-points by

$$\omega_i = e^{-i/N} \sinh(1/N). \quad (5.24)$$

The weight becomes smaller for higher steps, meaning that the density of points increases as the points are sampled closer to the maximum likelihood. The PLINY convergence occurs after the step I , when the contribution of the live-points to the evidence reaches a ratio given by a user input tolerance t

$$\frac{e^{-\frac{I}{N}}}{N} \sum_{\Theta_j \in \mathcal{S}} \mathcal{L}_j < t \sum_{\Theta_i \in \mathcal{C}} \omega_i \mathcal{L}_i. \quad (5.25)$$

Moreover, each implementation has its own algorithm to ensure a reasonable acceptance rate, i.e. the ratio of accepted *live-points* over the total of sampled points. PLINY, similarly as

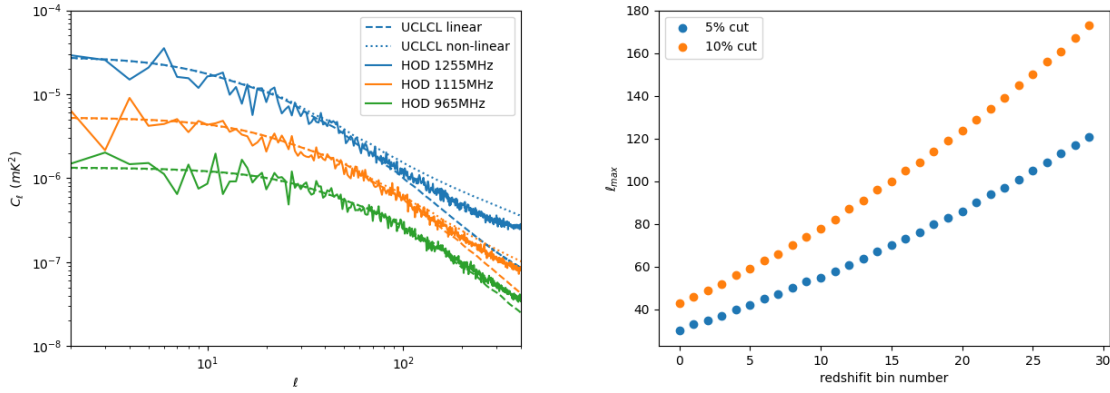


FIGURE 5.2: Left: Comparison between the APS estimate from the HOD mock and the theoretical UCLCL in linear and non-linear theory. We show the spectra for three frequencies: 1255MHz, 1115MHz, and 965MHz, which are amplified by 2, 1, and 0.5, respectively, for better visualization. Lower frequencies have a larger range of multipoles in the linear regime and, therefore, greater agreement between theory and data. Right: 5% and 10% of discrepancy between linear and non-linear UCLCL computations. These values were used to define the multipole range for the Monte Carlo analysis.

MULTINEST, fits one or more ellipsoids that together bound all the *live-points*, so the new points are sampled inside them. However, PLINY implemented a more efficient method for finding the minimum-volume covering ellipsoid (MVCE), which minimizes the rate of rejected points. Also, PLINY presents a more efficient parallel scheme, with no master process and minimal exchange of information between processors. A more detailed description can be found in (Rollins, 2015).

5.3 Results of parameter estimation

In this section we show the analysis performed via the nested sampling method using the UCLCL-PARAM-EST code. The cosmological model is assumed to be Λ CDM. We use the HIR4 mocks simulated via the HOD method to mimic the BINGO data. A first look at the APS measured from these mocks shows that they agree only in the linear range of what is expected from the UCLCL computations (Fig. 5.2-left). This is because the non-linearity in UCLCL comes from the Takahashi fitting, while in the mock it comes from the dark matter N-body simulation and HI distribution in halos. Therefore, we need to choose a suitable interval ℓ that takes into account this effect. Figure (5.2-right) shows the maximum ℓ where the UCLCL

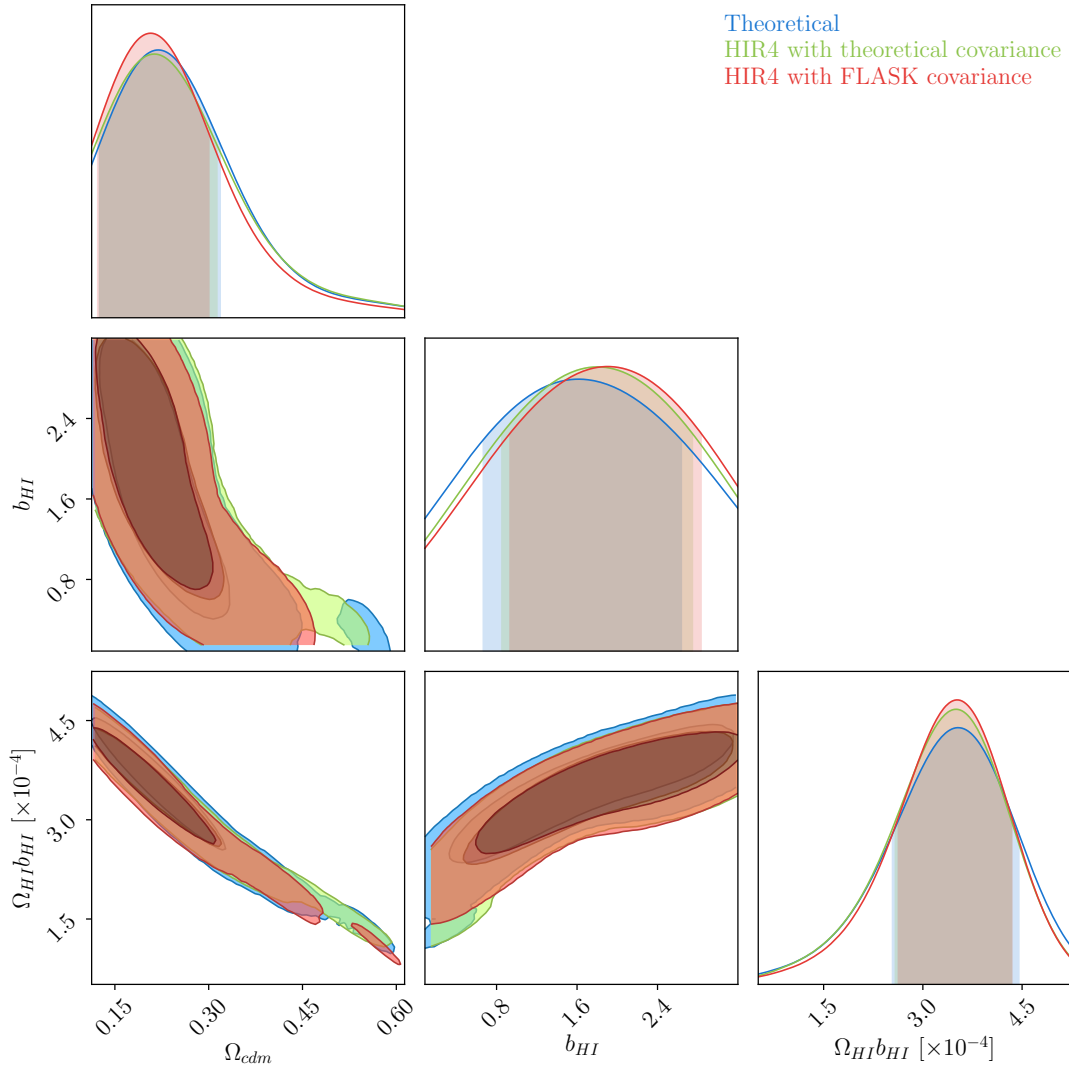


FIGURE 5.3: The (red) contours obtained using the HIR4 HOD mock spectrum as data vector and the covariance from FLASK are compared to (green) contours obtained using the same data vector but with the theoretical covariance implemented as explained in the text, and also to a fully theoretical description (in blue), where the data vector is also theoretical. The similarity of the contours shows the consistency of the methods. All three cases correspond to a redshift bin of 10MHz centered at 965MHz, and bandwidth of $\Delta\ell = 11$.

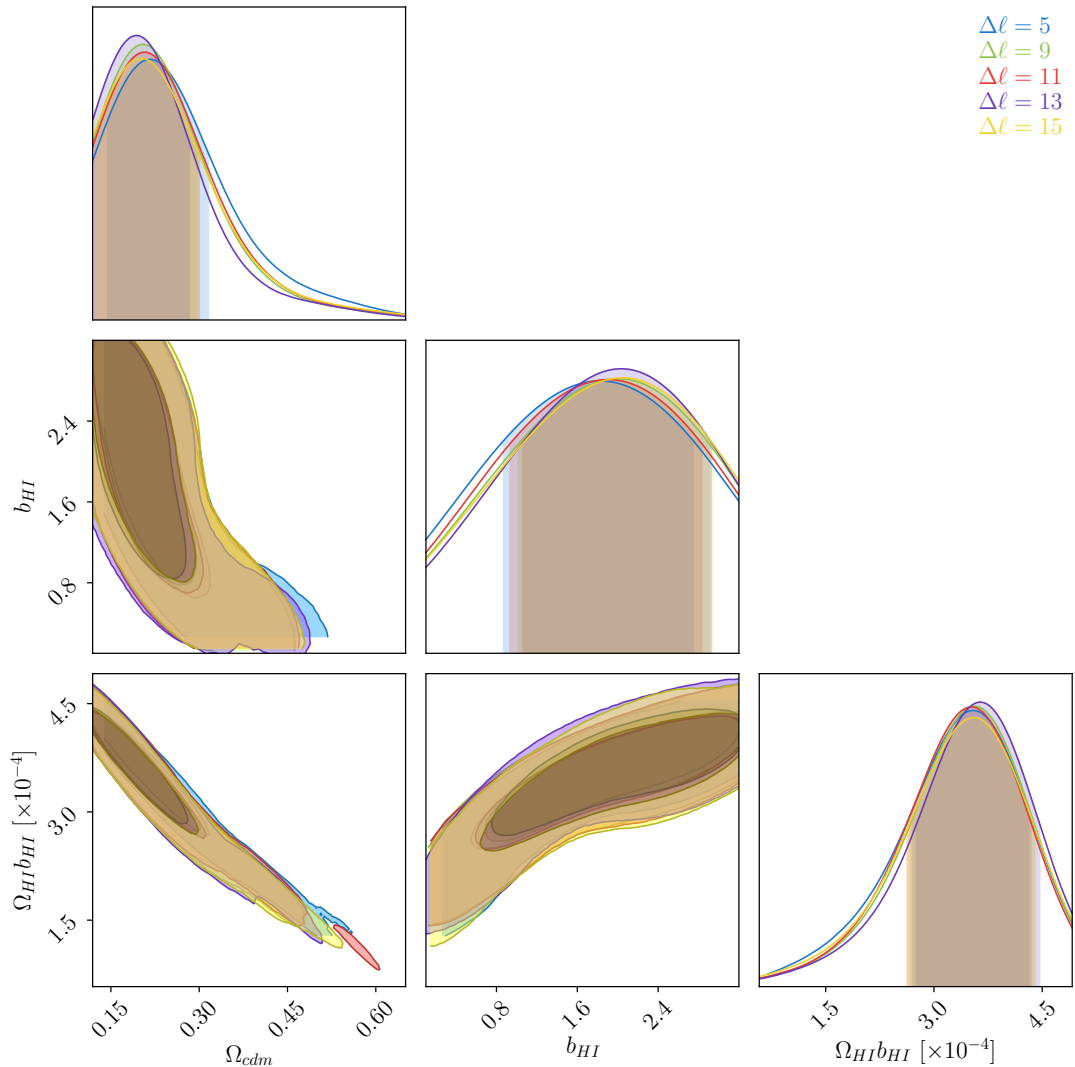


FIGURE 5.4: Comparison of cosmological constraints for different $\Delta\ell$ values. We are using the spectrum of the HIR4 HOD mock in the redshift bin centered at 965MHz and the FLASK covariance. The contours for different $\Delta\ell$ are very consistent.

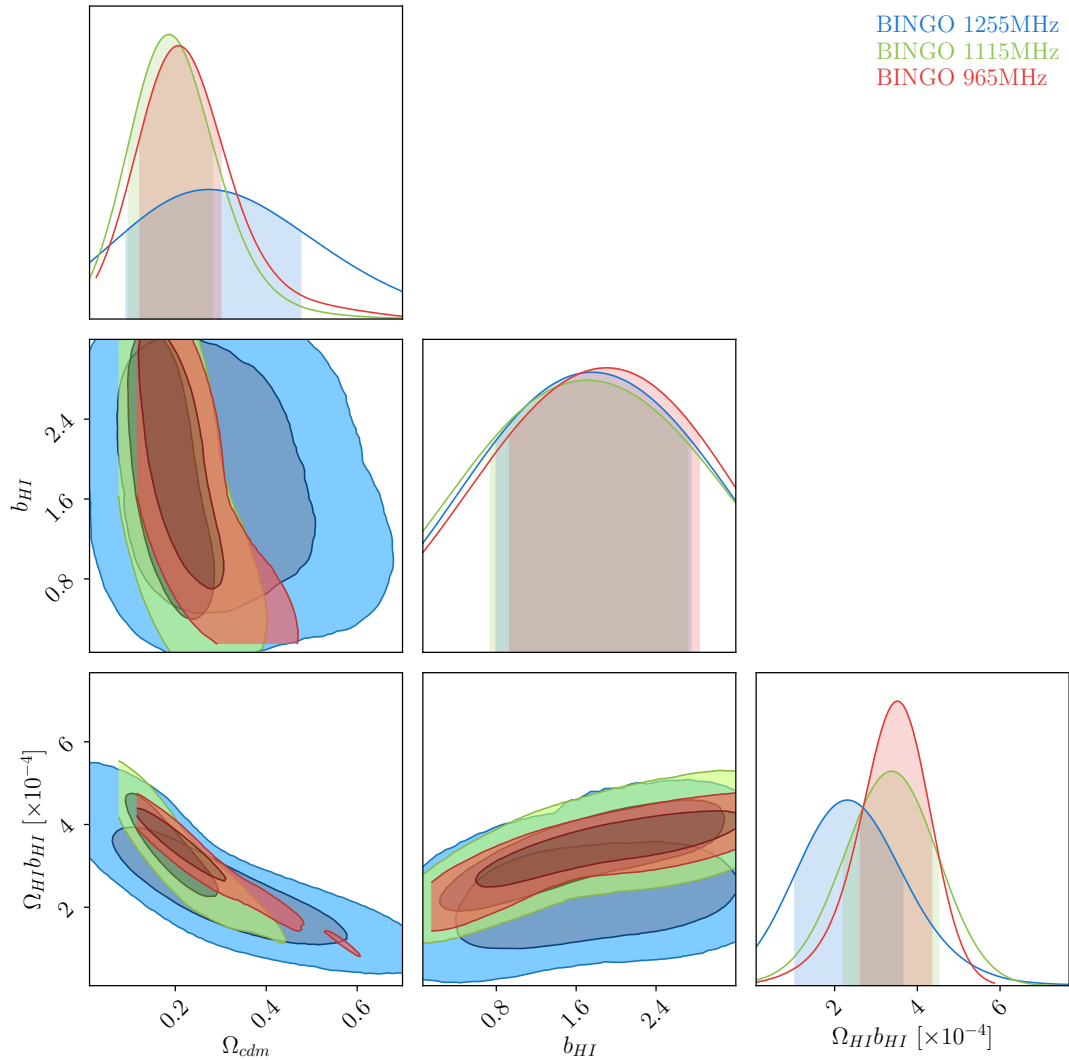


FIGURE 5.5: Comparison of cosmological constraints for different redshift bins. We are fitting the HIR4 HOD mock for the redshift bins centered at 1255MHz, 1115Mhz and 965MHz, respectively, using a FLASK covariance and a bandwidth binning of $\Delta\ell = 11$. The constraints are stronger for lower frequency (higher redshift) due to the larger ℓ_{max} .

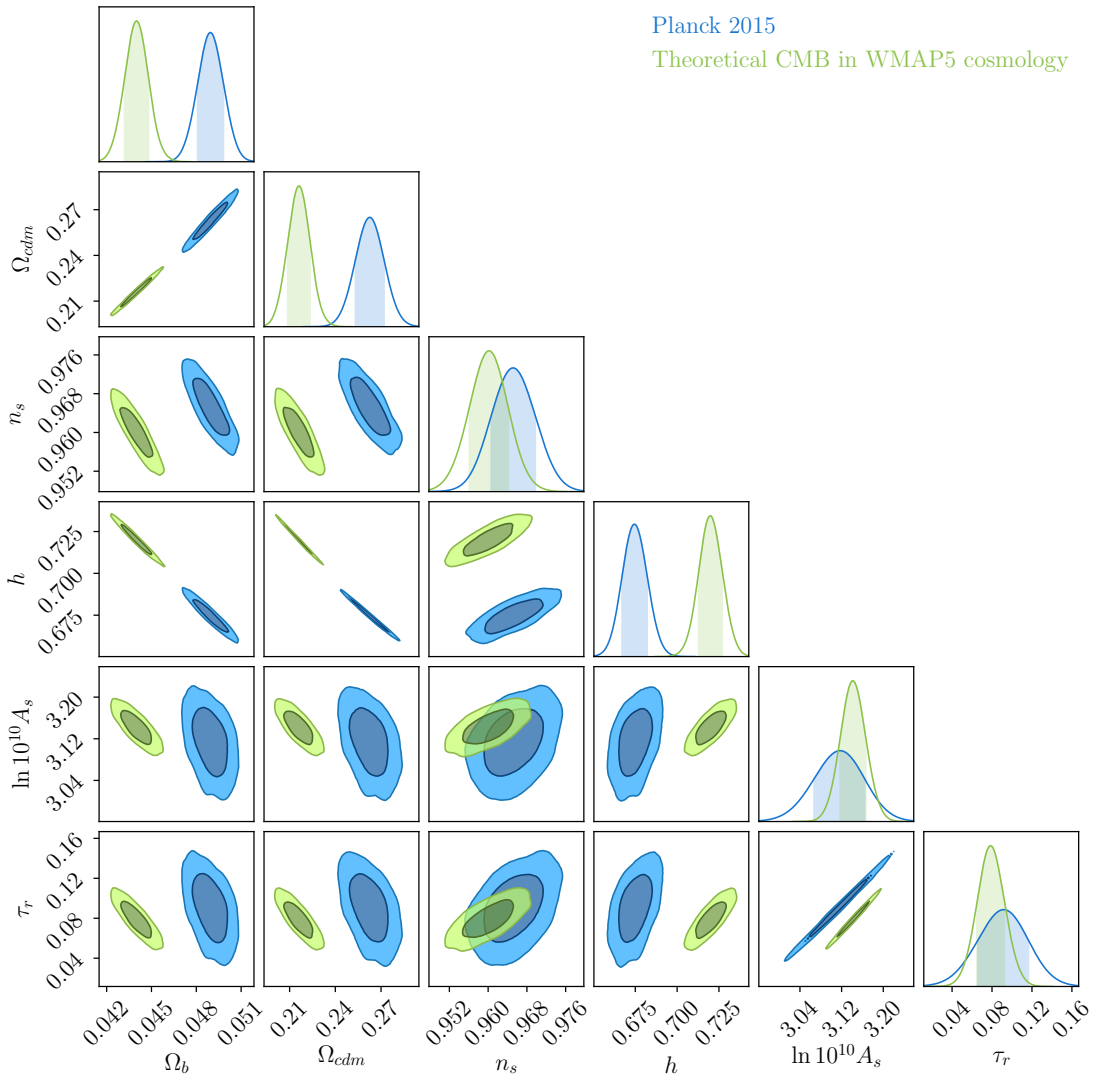


FIGURE 5.6: Comparison of cosmological constraints for the Planck 2015 data and a theoretical CMB likelihood defined at fiducial cosmology given by the WMAP5 results. Notice that the contours do not overlap for most of the parameters.

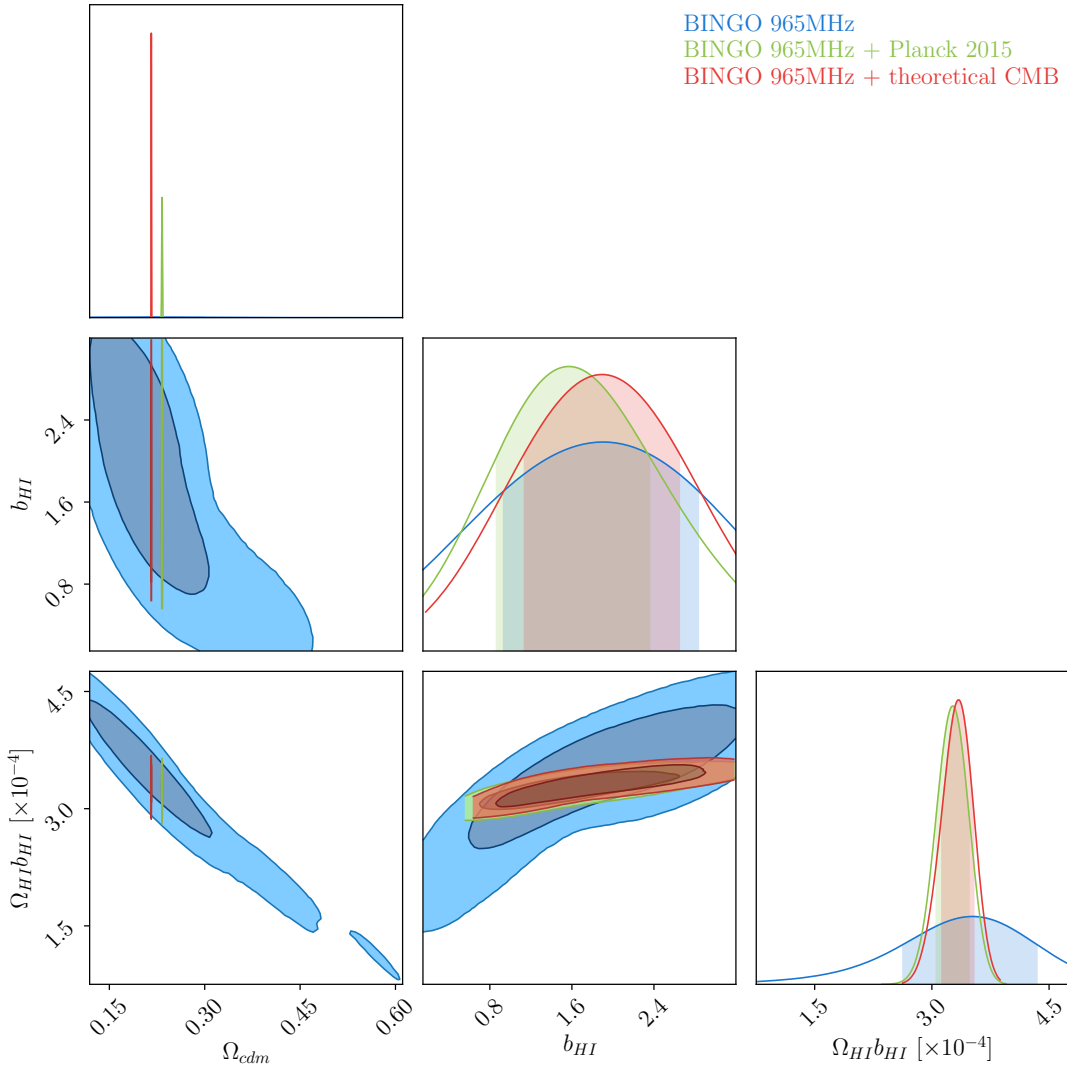


FIGURE 5.7: Comparison of cosmological constraints for BINGO 965MHz alone, BINGO 965MHz combined with Planck 2015 data, BINGO 965MHz combined with theoretical CMB likelihood. In all cases, it was used HIR4 HOD mock, FLASK covariance, and a bandwidth binning of $\Delta\ell = 11$. When combining with CMB (either Planck 2015 or theoretical), the constraints in $\Omega_{HI}b_{HI}$ are much stronger due to the measurement of the Ω_{cdm} . When using theoretical CMB likelihood, the constraint in $\Omega_{HI}b_{HI}$ is shifted in the direction of the correct value.

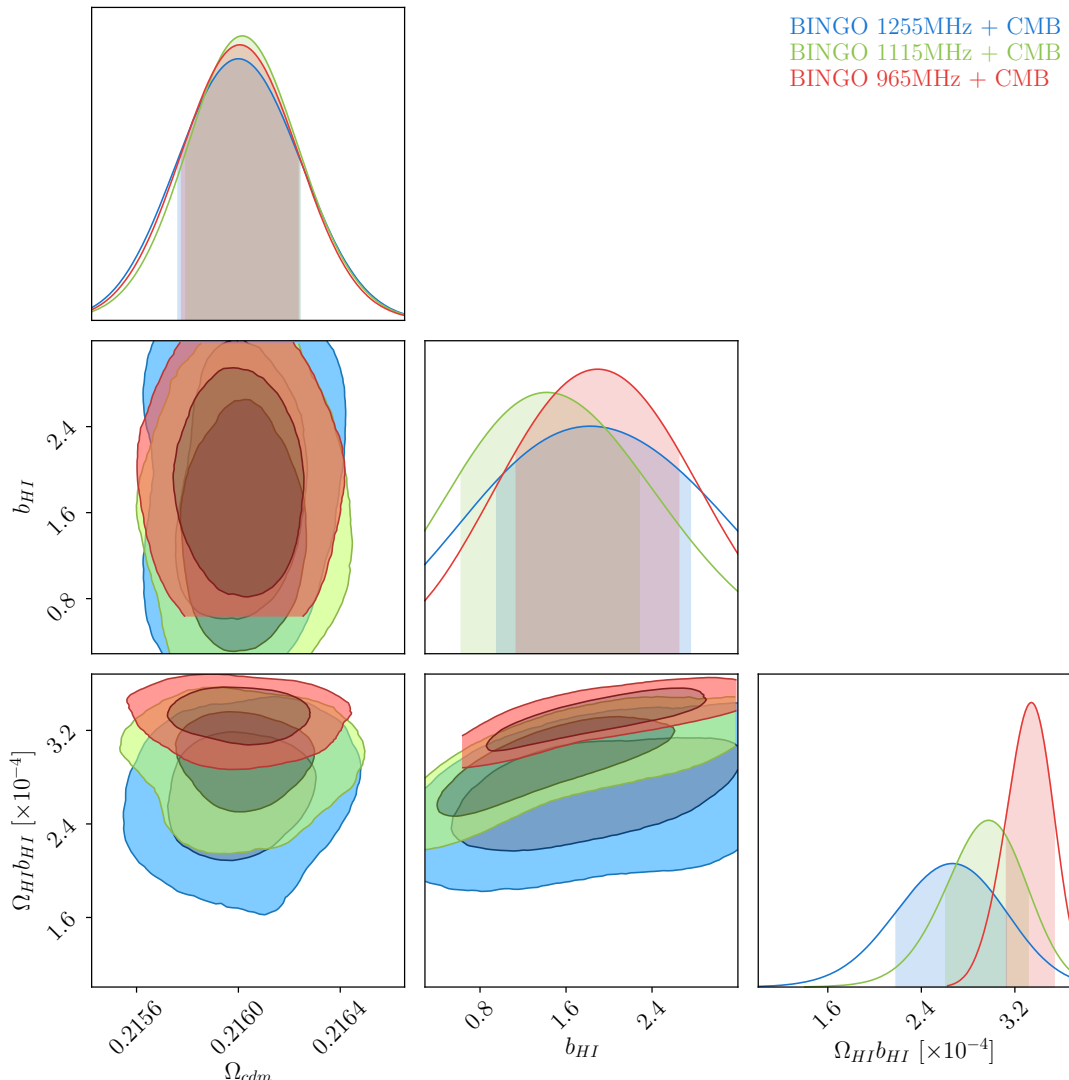


FIGURE 5.8: Comparison of cosmological constraints for BINGO 965MHz + CMB, BINGO 1115MHz + CMB, BINGO 1255MHz + CMB, where CMB stands for the theoretical CMB likelihood with fiducial cosmology according to WMAP5. We are using the HIR4 mock spectrum and the FLASK covariance with a bandwidth binning of $\Delta\ell = 11$. $\Omega_{HI}b_{HI}$ presents better constraints in all cases compared to BINGO alone. Also, the constraints are stronger for lower frequencies (higher redshift). The bias (b_{HI}) parameter, on the other hand, is not constrained even with CMB.

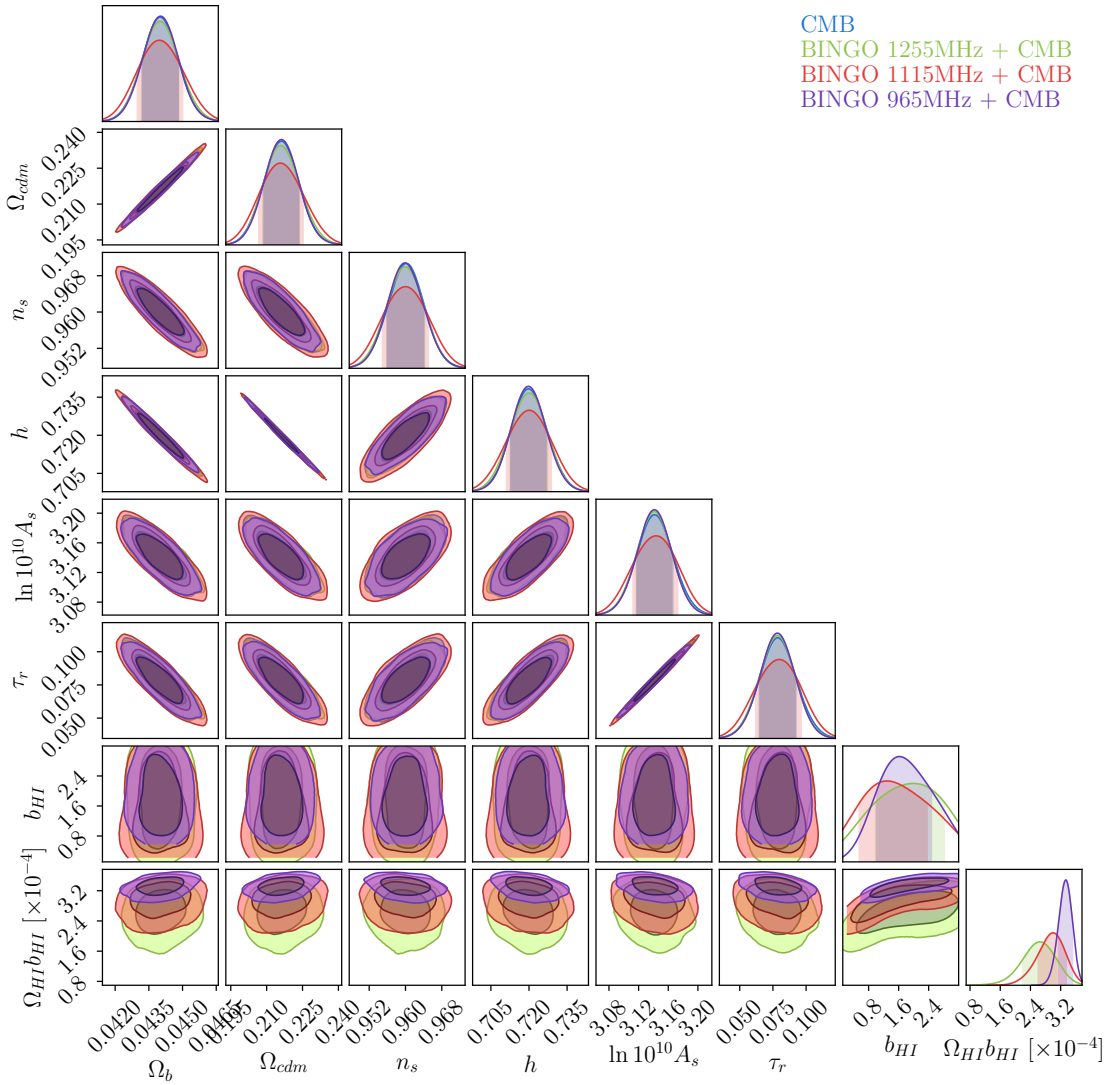


FIGURE 5.9: Constraints for six parameters of Λ CDM model plus two parameters of HI history. We compare the contours obtained for BINGO 965MHz + CMB, BINGO 1115MHz + CMB, BINGO 1255MHz and CMB alone. The data vectors, covariance and bandwidth binning are the same as in figure (5.8). We did not find a significant improvement compared to CMB alone.

linear APS diverges in more than 5% and 10% from the non-linear UCLCL description. Following (Loureiro et al., 2019), we applied the 10% values to the upper limit of the multipole range in the Monte Carlo analysis. The bin numbers in figure (5.2-right) correspond to 30 bins (channels) of redshift, defined in the frequency range of 960MHz to 1260MHz, where each bin correspond to a width of 10MHz. We first show the results for the bin of lowest frequency (highest redshift), i.e. centered at 965MHz, that has the largest multipole range being fitted, and therefore we expect stronger constraints in the parameter estimation. Later, we expand the analysis to the bins centered at 1115MHz and 1255MHz, which correspond to a central bin and the bin of highest frequency (lowest redshift).

The pseudo-APS estimate of the mock maps were computed by Eq. (4.42), after applying the BINGO mask (Fig. 4.3) to the full-sky maps. This estimate takes into account the sky fraction and pixel window function effects. However, since the mock maps were previously convolved with a Gaussian kernel to mimic the BINGO beam, we also need to correct this effect. This is done by multiplying the measured spectrum by $1/B_\ell^2$, where B_ℓ is the Gaussian beam window function (e.g. White and Srednicki, 1994). This term can be computed with the function HEALPY.SPHTFUNC.GAUSS_BEAM¹ of HEALPY. Moreover, we perform a bandwidth binning by:

$$\hat{S}_b^{ij} = \frac{\sum_{\ell=\ell_0}^{\ell_0+\Delta\ell} (2\ell+1) \hat{S}_\ell^{ij}}{\sum_{\ell=\ell_0}^{\ell_0+\Delta\ell} (2\ell+1)}. \quad (5.26)$$

So, if, for instance, $\Delta\ell = 11$, the first bin is $2 \leq \ell \leq 12$, the second is $13 \leq \ell \leq 23$, and so on. This binning acts in a way that removes the correlation between the mixed modes that arise due to the effect of the mixing matrix on the true spectrum (Loureiro et al., 2019). Therefore, the choice of $\Delta\ell$ can be based on the shape of the mixing matrix, i.e. smaller sky coverage requires a bigger $\Delta\ell$ for the BINGO mask (fig . 4.4). We checked that $\Delta\ell = 11$ is a number that would make the mixing matrix roughly diagonal.

The covariance was computed with 500 FLASK simulations. The APS input for FLASK was computed via UCLCL code, with cosmological parameters set up according to the WMAP5 cosmology, and bias and Ω_{HI} according to the HIR4 mock. The Pseudo-APS estimate and the further bandwidth binning were computed for each FLASK realization in the same way as done for the HIR4 mock. The covariance matrix (Eq. 4.53) was then computed for the binned spectra. In order to compare this covariance with the theoretical one (Eq. 4.73), we defined a

¹https://healpy.readthedocs.io/en/1.5.0/generated/healpy.sphtfunc.gauss_beam.html

bandwidth binning for the theoretical covariance by

$$\Sigma_{bb'}^{ij} = \frac{1}{\sum_{\ell,\ell'} (2\ell+1)(2\ell'+1)} \sum_{\ell,\ell'} (2\ell+1)(2\ell'+1) \Sigma_{\ell\ell'}^{ij}. \quad (5.27)$$

The contours obtained in each sampling are portrayed in figures (5.3 to 5.9). Also check the table of the prior ranges (table 5.1), and the tables of the recovered parameters (tables 5.3, 5.2). Figure (5.3) compares the FLASK covariance with the theoretical covariance, and also the constraints estimated with the HIR4 mock spectrum with constraints using a theoretical spectrum (UCLCL APS with BINGO mixing matrix). We get similar results in all three cases, indicating that we recover the correct parameters with 68% level of confidence and with consistent contours for both covariance models. Next, Fig. (5.4) shows similar constraints for bandwidths of different $\Delta\ell$. We found that the choice of the $\Delta\ell$ value does not have significant impact in the contours. In figure (5.5), we compare constraints for three different redshift bins and for the same free parameters of the other figures. We see that the constraints are better for lower frequencies (higher redshift), which is explained by the way we are cutting the multipole range (Fig. 5.2-right). However, we recover the expected values with 68% level of confidence in all three cases. Notice that the true value of the bias and Ω_{HI} are redshift dependent, as you can see in table (5.3).

Next, we study the combination of BINGO data with CMB data in order to place stronger constraints. The Planck experiment is the one with the most precise measurements. So, when Bingo's real data is available, we intend to combine the Planck data with BINGO. However, the HIR4 is WMAP5 cosmology, which is an older experiment, and the centered values are displaced from the current values. Therefore, to be consistent with the mocks, we use a theoretical CMB likelihood in order to mimic the Planck constraints, but with a fiducial cosmology defined by the WMAP5 experiment. This likelihood function was built using a modelling of the CMB thermal noise (section 2.2 of (Abdalla and Rawlings, 2007)) according to the Planck experimental setup defined in (Planck et al., 2006). Figure (5.6) compares this theoretical likelihood with Planck 2015, and the recovered parameters are displayed in table (5.2). See that the contours, although not identical, are similar with respect to size and shape, with the theoretical one being a bit smaller. The fact that the contours do not overlap, reflects the choice of a WMAP5 (instead of a Planck) fiducial cosmology. Figures (5.7) show the constraints when combining with each of these two likelihoods. Both cases place stronger constraints when compared to BINGO alone. However, there are differences in the measurements. Since there is degeneracy in $\Omega_{cdm} \times \Omega_{HI} b_{HI}$, the theoretical likelihood shifts the measurement of $\Omega_{HI} b_{HI}$ towards the expected value from the HIR4 mock. Figure (5.8) shows three redshift bins of BINGO combined

TABLE 5.1: Prior range for the samplings. The line divides the parameters that were not used in all the jobs.

Parameter	Prior range
b_{HI}	0,3.2
$\Omega_{HI}b_{HI}$	1e-6,0.0008
Ω_{cdm}	0,0.7
<hr/>	
Ω_b	0.03,0.07
τ	0.01,0.2
n_s	0.87,1.07
h	0.55,0.91

TABLE 5.2: Recovered parameters from Planck 2015 and theoretical CMB likelihood. They correspond to the contours of fig. (5.6)

Parameter	Planck 2015	Theoretical CMB in WMAP5 cosmology
Ω_b	$(489.5 \pm 8.7) \times 10^{-4}$	$(440.0^{+8.1}_{-8.0}) \times 10^{-4}$
Ω_{cdm}	$(262.6^{+9.3}_{-9.5}) \times 10^{-3}$	$(216.2^{+7.2}_{-7.5}) \times 10^{-3}$
n_s	$(965.1^{+4.7}_{-4.5}) \times 10^{-3}$	$(960.2^{+3.9}_{-4.1}) \times 10^{-3}$
h	$(674.4^{+7.6}_{-7.4}) \times 10^{-3}$	$(719.7^{+7.3}_{-6.9}) \times 10^{-3}$
$\ln 10^{10} A_s$	$3.117^{+0.048}_{-0.050}$	$3.141^{+0.025}_{-0.024}$
τ_r	$0.092^{+0.025}_{-0.026}$	$0.078^{+0.014}_{-0.013}$

with the theoretical CMB likelihood. Again, we check that lower frequencies (higher redshift) present stronger constraints. Also, compared to BINGO alone, we can precisely measure the values of $\Omega_{HI}b_{HI}$ when combining with CMB. Finally, figure (5.9) shows the contours for BINGO + CMB when all cosmological parameters are set as free parameters in the sampling. Furthermore, the recovered parameters are shown in table (5.4). The contours are not significantly stronger than CMB alone.

TABLE 5.3: Recovered parameters and 68% level of confidence for Monte Carlo analysis done with limited number of free parameters: Ω_{cdm} , b_{HI} , $\Omega_{HI}b_{HI}$. Each sub-table corresponds to the set of contours portrayed in figures (5.4, 5.5, 5.7, 5.8), respectively.

Parameter	True	Theoretical	HIR4 with theo. cov.	HIR4 with FLASK cov.
Ω_{cdm}	0.216	$0.220^{+0.098}_{-0.095}$	$0.212^{+0.101}_{-0.086}$	$0.207^{+0.093}_{-0.085}$
$b_{HI(30)}$	1.17	$1.61^{+1.03}_{-0.94}$	$1.80^{+0.95}_{-0.94}$	$1.90^{+0.93}_{-0.97}$
$\Omega_{HI(30)}b_{HI(30)}$	35.5×10^{-5}	$(35.3^{+9.2}_{-9.9}) \times 10^{-5}$	$(35.0^{+8.4}_{-9.2}) \times 10^{-5}$	$(35.2^{+8.3}_{-8.9}) \times 10^{-5}$
Parameter	True	$\Delta\ell = 5$	$\Delta\ell = 9$	$\Delta\ell = 11$
Ω_{cdm}	0.216	$0.216^{+0.099}_{-0.072}$	$0.205^{+0.091}_{-0.083}$	$0.207^{+0.093}_{-0.085}$
$b_{HI(30)}$	1.17	$1.82^{+0.92}_{-0.95}$	$2.00^{+0.91}_{-0.98}$	$1.90^{+0.93}_{-0.97}$
$\Omega_{HI(30)}b_{HI(30)} \times 10^{-5}$	35.5	$(35.4^{+7.7}_{-8.3})$	$(35.7^{+8.2}_{-9.0})$	$(35.2^{+8.3}_{-8.9})$
Parameter	True	1255MHz	1115MHz	965MHz
Ω_{cdm}	0.216	$0.27^{+0.20}_{-0.18}$	$0.187^{+0.094}_{-0.090}$	$0.207^{+0.093}_{-0.085}$
$b_{HI(1)}$	1.01	$1.76^{+0.99}_{-0.96}$	—	—
$\Omega_{HI(1)}b_{HI(1)}$	29.0×10^{-5}	$(2.3 \pm 1.3) \times 10^{-4}$	—	—
$b_{HI(15)}$	1.08	—	$1.71^{+0.99}_{-0.97}$	—
$\Omega_{HI(15)}b_{HI(15)}$	32.3×10^{-5}	—	$(3.4^{+1.1}_{-1.2}) \times 10^{-4}$	—
$b_{HI(30)}$	1.17	—	—	$1.90^{+0.93}_{-0.97}$
$\Omega_{HI(30)}b_{HI(30)}$	35.5×10^{-5}	—	—	$(35.2^{+8.3}_{-8.9}) \times 10^{-5}$
Parameter	True	965MHz	965MHz + Planck 15	965MHz + theo-CMB
Ω_{cdm}	0.216	$0.207^{+0.093}_{-0.085}$	$(2328.6^{+5.5}_{-5.4}) \times 10^{-4}$	$(2108.2 \pm 2.1) \times 10^{-4}$
$b_{HI(30)}$	1.17	$1.90^{+0.93}_{-0.97}$	$1.57^{+0.79}_{-0.71}$	$1.86^{+0.77}_{-0.70}$
$\Omega_{HI(30)}b_{HI(30)}$	35.5×10^{-5}	$(35.2^{+8.3}_{-8.9}) \times 10^{-5}$	$(32.7 \pm 2.1) \times 10^{-5}$	$(33.4^{+1.9}_{-2.1}) \times 10^{-5}$
Parameter	True	1255MHz + CMB	1115MHz + CMB	965 MHz + CMB
Ω_{cdm}	0.216	$(2160.0^{+2.4}_{-2.3}) \times 10^{-4}$	$(2160.1^{+2.3}_{-2.2}) \times 10^{-4}$	$(2160.1 \pm 2.3) \times 10^{-4}$
$b_{HI(1)}$	1.01	$1.82^{+0.93}_{-0.87}$	—	—
$\Omega_{HI(1)}b_{(1)}$	29.0×10^{-5}	$(26.7^{+4.6}_{-4.9}) \times 10^{-5}$	—	—
$b_{HI(15)}$	1.08	—	$1.43^{+0.85}_{-0.80}$	—
$\Omega_{HI(15)}b_{(15)}$	32.3×10^{-5}	—	$(29.8^{+3.3}_{-3.7}) \times 10^{-5}$	—
$b_{HI(30)}$	1.17	—	—	$1.89^{+0.76}_{-0.75}$
$\Omega_{HI(30)}b_{(30)}$	35.5×10^{-5}	—	—	$(33.4^{+1.9}_{-2.1}) \times 10^{-5}$

TABLE 5.4: Recovered parameters and 68% level of confidence for six Λ CDM parameters plus b_{HI} and $\Omega_{HI}b_{HI}$. We compare three frequencies combined with CMB and CMB alone. They correspond to the contours of Fig. (5.9).

Parameter	True	CMB	1255MHz + CMB	1115MHz + CMB	965MHz + CMB
$\Omega_b \times 10^4$	440	$440.0^{+8.1}_{-8.0}$	$439.9^{+8.4}_{-8.1}$	$439.6^{+10.5}_{-9.6}$	$440.2^{+7.9}_{-7.8}$
$\Omega_{cdm} \times 10^3$	216	$216.2^{+7.2}_{-7.5}$	$216.0^{+7.7}_{-7.6}$	$215.8^{+9.5}_{-9.0}$	$216.1^{+7.3}_{-7.1}$
$n_s \times 10^3$	960	$960.2^{+3.9}_{-4.1}$	$959.9^{+4.1}_{-4.0}$	$959.9^{+5.1}_{-5.0}$	$959.9^{+4.1}_{-4.0}$
$h \times 10^3$	720	$719.7^{+7.3}_{-6.9}$	$720.0^{+7.3}_{-7.4}$	$720.1^{+8.7}_{-9.0}$	$719.9^{+6.7}_{-7.0}$
$\ln 10^{10} A_s$	3.1424	$3.141^{+0.025}_{-0.024}$	3.141 ± 0.024	$3.144^{+0.029}_{-0.031}$	3.141 ± 0.023
τ_r	0.079	$0.078^{+0.014}_{-0.013}$	$0.079^{+0.013}_{-0.014}$	$0.080^{+0.016}_{-0.018}$	0.079 ± 0.013
$b_{(1)}$	1.01	—	$1.99^{+0.82}_{-1.01}$	—	—
$\Omega_{HI(1)} b_{HI(1)} \times 10^5$	29.0	—	$26.6^{+4.4}_{-4.6}$	—	—
$b_{HI(15)}$	1.08	—	—	$1.29^{+1.06}_{-0.74}$	—
$\Omega_{HI(15)} b_{HI(15)} \times 10^5$	32.3	—	—	$30.0^{+3.4}_{-3.9}$	—
$b_{HI(30)}$	1.17	—	—	—	$1.62^{+0.86}_{-0.60}$
$\Omega_{HI(30)} b_{HI(30)} \times 10^5$	35.5	—	—	—	$33.3^{+1.8}_{-1.9}$

Chapter 6

Conclusion

BINGO is a new and exciting project with prediction of starting the operations this year. BINGO is expected to place constraints in a lot of cosmological scenarios, such as dynamical dark energy, dark energy and dark matter interaction, and modified gravity (Abdalla, Ferreira et al., 2021). The main goal of this thesis was to study cosmological constraints on BINGO from measurements of Angular Power Spectra (APS). Here, we considered Λ CDM model only, and we used HIR4 mocks to simulate the BINGO intensity maps. We used a Monte Carlo technique called *nested sampling*, combined with a likelihood function that depends on some objects, like the mixing matrix and the covariance matrix. Such objects were largely discussed in chapter (4), together with a discussion on the APS theory and estimates.

We also discussed some instrumental aspects of BINGO, in particular, the optical design in chapter (3). We simulated the beam for each horn position and we summed them up to predict the total beam for some possible configurations of horn arrangements. We found that the arrangement called *Double-Rectangular* was the one that presented the smoothest profile with the minimum number of horns. We also found that the beams displaced from the center of the optical plane have optical aberrations below 30dB of the peak of the beam. This means that the aberrations are acceptable and that the peaks of the beams are relatively well maintained. Also, we found that the Q , U , V polarization leakage is below 25dB compared to the Intensity I . All of this shows that this configuration is appropriate for the scientific goals of BINGO (Abdalla, Marins, Motta et al., 2021).

The results of the Monte Carlo analysis are presented in chapter (5). In summary, our findings are: i) The HIR4 mocks agree with UCLCL only in the linear regime, and therefore we should appropriately cut the multipole range for each redshift bin. In addition, the range is larger for lower frequencies (higher redshift); ii) We get similar contours using theoretical covariance or FLASK covariance, which means that the two descriptions are consistent; iii) The $\Delta\ell$ choice in the bandwidth binning does not have a significant impact on the contours for the tested cases; iv) We can find better contours for the lower frequencies than for the

higher frequencies due to the way we cut the multipole range; v) We successfully combined the BINGO likelihood with a CMB likelihood, placing better constraints in the parameters; vi) We successfully recovered the true parameters with confidence level of the order of $1\sigma_{68\%}$ or lower in all of our analyses; vii) Combining CMB with a single frequency of BINGO does not have a significant impact in constraining the Λ CDM parameters in comparison with CMB (mimicking Planck) only. In fact, in some cases we find a standard deviation higher than in CMB alone. This is due to the fact that we are fitting single frequencies instead of the whole set of redshift bins of BINGO. For higher frequencies, we have a small data vector with a high cosmic variance (encoded by the covariance matrix), and therefore not contributing to the Planck constraints. Moreover, BINGO is expected to play a more important role in cosmological models beyond Λ CDM, with non-standard dark energy models. Our results, that are Λ CDM only and single frequencies, seem to be compatible with the state of the art of BINGO forecasts (Costa, Landim et al., 2021).

The method presented here for cosmological constraints is an alternative for the Fisher matrix method, which was applied to BINGO forecasts in (Costa, Landim et al., 2021), and also in (Yohana, Li and Ma, 2019; Xiao, Costa and Wang, 2021). Since the Fisher matrix method produces the optimal scenario (Costa, Landim et al., 2021), it is helpful to compare it with our *nested sampling* method or even to the classical MCMC. As a next step, we aim to expand our analysis to the full set of 30 BINGO redshift bins and to obtain a realistic forecast analysis. This task is computationally expensive, and large computational clusters are required. We also need to take into account thermal noise and foreground removal, which will enlarge the covariance matrix.

Moreover, this is the first work of constraining cosmology from the BINGO HIR4 mocks (Zhang, Motta, Novaes et al., 2021). This is more challenging than using just a theoretical spectrum or even a FLASK simulation as data vector. In fact, the FLASK algorithm ensures that the realizations follow the theoretical spectrum given as input. In other words, it would be a very controlled pipeline. On the other hand, the HIR4 mock building is a map making process independent of our APS modelling (UCLCL). For instance, in UCLCL, we model b_{HI} and Ω_{HI} as constants over the redshift bin, while, in the HIR4 maps, they depend on z as a result of the distribution of HI in halos. Our results seem to validate the HIR4 HOD mock, and show that we can recover cosmology from them, although this still has to be confirmed in a full 30 bins analysis. In addition, the HIR4 HAM mock is left to be analyzed in the future.

In summary, our future works will be: i) To do the Monte Carlo analysis for the 30 redshift bins combined for the HIR4 HOD mock. This requires a total of 66 parameters if we assume one free parameter of b_{HI} and Ω_{HI} for each redshift bin. An alternative would be to use other

parametrizations, e.g. a quadratic function over the BINGO range; ii) To take into account thermal noise and foreground contamination; iii) To do the same for the HIR4 HAM mock; iv) To study non-standard cosmology. We will need to implement the UCLCL code to be able to compute the APS in those non-standard models. Also, HI mocks in non-standard cosmology are under development in the BINGO collaboration; v) To compare different covariance building methods. We have so far used a FLASK covariance and compared it to a theoretical model. However, we aim to compare it to other methods, such as L-PICOLA (Howlett, Manera and Percival, 2015) fast light cone halo catalog generation; vi) To combine our APS analysis with BAO and FRB in order to get better constraints.

Appendix A

Spherical Harmonics

The Spherical Harmonics $Y_{\ell m}(\theta, \phi)$ are defined as the eigenfunctions of the Laplace operator ∇^2 over the 2-sphere, with associated eigenvalues $-\ell(\ell + 1)$. In other words, they are the solution for the equation

$$\frac{1}{Y \sin \theta} \frac{\partial}{\partial \theta} \left(\sin \theta \frac{\partial Y}{\partial \theta} \right) + \frac{1}{Y \sin^2 \theta} \frac{\partial^2 Y}{\partial \phi^2} = -\ell(\ell + 1). \quad (\text{A.1})$$

Using separation of variables, one can find that they are given by

$$Y_{\ell m}(\theta, \phi) = X_{\ell m}(\theta) \exp(im\phi), \quad (\text{A.2})$$

$$X_{\ell m} = (-1)^m \left(\frac{2\ell + 1}{4\pi} \right)^{1/2} \left[\frac{(l-m)!}{(l+m)!} \right]^{1/2} P_{\ell m}(\cos \theta), \quad (\text{A.3})$$

$$P_{\ell m}(\mu) = \frac{1}{2^\ell \ell!} (1 - \mu^2)^{m/2} \left(\frac{d}{d\mu} \right)^{\ell+m} (\mu^2 - 1)^\ell, \quad (\text{A.4})$$

where $P_{\ell m}(\mu)$ are the associated Legendre functions of degree ℓ and order m . The integers ℓ, m satisfy $0 \leq \ell \leq \infty$ and $-\ell \leq m \leq \ell$, and they are also the angular degree and angular order of the Spherical Harmonics (e.g.: Edmonds, 1996).

The spherical harmonics form a complete orthonormal basis on the sphere

$$\int_{\Omega} d\Omega Y_{\ell m}^*(\hat{\mathbf{n}}) Y_{\ell' m'}(\hat{\mathbf{n}}) = \delta_{\ell\ell'} \delta_{mm'}, \quad (\text{A.5})$$

$$\sum_{\ell,m} Y_{\ell m}(\hat{\mathbf{n}}) Y_{\ell m}^*(\hat{\mathbf{n}}') = \delta(\hat{\mathbf{n}}, \hat{\mathbf{n}}'), \quad (\text{A.6})$$

where one should notice that the unitarity of the eigenfunctions in eq. (A.5-A.6) is ensured by the choice of the multiplicative factors in equations (A.2-A.3-A.4).

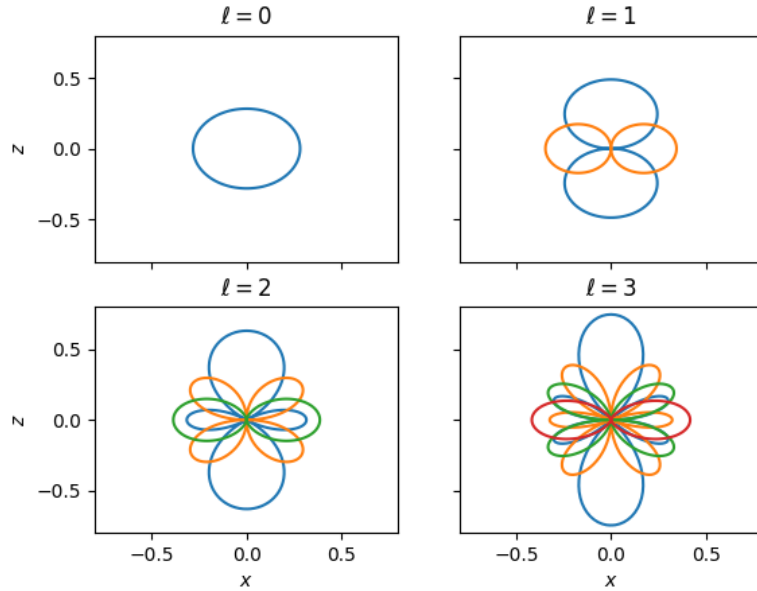


FIGURE A.1: The absolute values of Spherical Harmonics for $\ell = 0, 1, 2, 3$. Each colour represents a non-negative m value, i.e.: blue, orange, green and red stands for $m = 0, 1, 2, 3$, respectively. (The multipoles with $m < 0$ are not portrayed due to the symmetry property $Y_{\ell-m} = Y_{\ell m}^*$).

One useful relation is the so-called addition theorem

$$\sum_m Y_{\ell m}(\hat{\mathbf{n}}) Y_{\ell m}^*(\hat{\mathbf{n}}') = \frac{2\ell + 1}{4\pi} P_\ell(\hat{\mathbf{n}} \cdot \hat{\mathbf{n}}'), \quad (\text{A.7})$$

where $P_\ell = P_{\ell 0}$ is the Legendre polynomial of order ℓ .

We also should recall the decomposition of the plane wave Spherical Harmonics

$$\exp(i\mathbf{k} \cdot \chi \hat{\mathbf{n}}) = 4\pi \sum_{\ell, m} i^\ell j_\ell(k\chi) Y_{\ell m}^*(\hat{\mathbf{k}}) Y_{\ell m}(\hat{\mathbf{n}}), \quad (\text{A.8})$$

where j_ℓ is the spherical Bessel function.

A.1 Wigner 3-j Symbols

The product of two Spherical Harmonics can be written as a combination of Spherical Harmonics

$$Y_{\ell_1 m_1} Y_{\ell_2 m_2} = \sum_{\ell_3, m_3} \left[\frac{(2\ell_1 + 1)(2\ell_2 + 1)(2\ell_3 + 1)}{4\pi} \right]^{1/2} \begin{pmatrix} \ell_1 & \ell_2 & \ell_3 \\ 0 & 0 & 0 \end{pmatrix} \begin{pmatrix} \ell_1 & \ell_2 & \ell_3 \\ m_1 & m_2 & m_3 \end{pmatrix} Y_{\ell_3 m_3}^*, \quad (\text{A.9})$$

where the array of integers are the Wigner 3-j symbols. They are non-zero when i) the bottom row indices sum to zero, $m_1 + m_2 + m_3 = 0$ and ii) the top row indices satisfy the triangle inequality $|\ell_1 - \ell_3| \leq \ell_2 \leq \ell_1 + \ell_3$. Also, if $m_1 + m_2 + m_3 = 0$, the Wigner 3-j is non-zero only if $\ell_1 + \ell_2 + \ell_3$ is even [Edmonds, 1996].

From equation (A.9) arises an import result that we call Gaunt integral

$$\int_{\Omega} d\Omega Y_{\ell_1 m_1} Y_{\ell_2 m_2} Y_{\ell_3 m_3} = \left[\frac{(2\ell_1 + 1)(2\ell_2 + 1)(2\ell_3 + 1)}{4\pi} \right]^{1/2} \begin{pmatrix} \ell_1 & \ell_2 & \ell_3 \\ 0 & 0 & 0 \end{pmatrix} \begin{pmatrix} \ell_1 & \ell_2 & \ell_3 \\ m_1 & m_2 & m_3 \end{pmatrix}. \quad (\text{A.10})$$

Moreover, the Wigner 3-j symbols satisfy two useful orthonormality relations

$$\sum_{\ell_3 m_3} (2\ell_3 + 1) \begin{pmatrix} \ell_1 & \ell_2 & \ell_3 \\ m_1 & m_2 & m_3 \end{pmatrix} \begin{pmatrix} \ell_1 & \ell_2 & \ell_3 \\ m_4 & m_5 & m_3 \end{pmatrix} = \delta_{m_1 m_4} \delta_{m_2 m_5} \quad (\text{A.11})$$

$$\sum_{m_1 m_3} \begin{pmatrix} \ell_1 & \ell_2 & \ell_3 \\ m_1 & m_2 & m_3 \end{pmatrix}, \begin{pmatrix} \ell_1 & \ell_4 & \ell_3 \\ m_1 & m_4 & m_3 \end{pmatrix} = \frac{1}{2\ell_2 + 1} \delta_{\ell_2 \ell_4} \delta_{m_2 m_4}. \quad (\text{A.12})$$

Bibliography

- Abbott, Timothy et al. (2016). ‘The Dark Energy Survey: more than dark energy—an overview’. In: *Monthly Notices of the Royal Astronomical Society* 460.2, pp. 1270–1299.
- Abdalla, E., E. G. Ferreira et al. (2021). ‘The BINGO project I: Baryon Acoustic Oscillations from Integrated Neutral Gas Observations’. In: arXiv: 2107.01633 [astro-ph.CO].
- Abdalla, Elcio and Alessandro Marins (2020). ‘The Dark Sector Cosmology’. In: *arXiv e-prints*, arXiv–2010.
- Abdalla, F. B., A. Marins, P. Motta et al. (2021). ‘The BINGO project III: optical design and optimisation of the focal plane’. In: arXiv: 2107.01635 [astro-ph.IM].
- Abdalla, Filipe B and S Rawlings (2007). ‘Determining neutrino properties using future galaxy redshift surveys’. In: *Monthly Notices of the Royal Astronomical Society* 381.4, pp. 1313–1328.
- Adam, Rémi et al. (2016). ‘Planck 2015 results-I. Overview of products and scientific results’. In: *Astronomy & Astrophysics* 594, A1.
- Aghanim, Nabila et al. (2020). ‘Planck 2018 results-I. Overview and the cosmological legacy of Planck’. In: *Astronomy & Astrophysics* 641, A1.
- Amendola, Luca and Shinji Tsujikawa (2010). *Dark energy: theory and observations*. Cambridge University Press.
- Anderson, TW (2003). *An introduction to statistical multivariate analysis*.
- Asorey, Jacobo et al. (2020). ‘HIR4: cosmology from a simulated neutral hydrogen full sky using Horizon Run 4’. In: *Monthly Notices of the Royal Astronomical Society* 495.2, pp. 1788–1806.
- Bacon, David J et al. (2020). ‘Cosmology with phase 1 of the Square Kilometre Array Red Book 2018: Technical specifications and performance forecasts’. In: *Publications of the Astronomical Society of Australia* 37.
- Balaguera-Antolínez, A et al. (2018). ‘Extracting cosmological information from the angular power spectrum of the 2MASS Photometric Redshift catalogue’. In: *Monthly Notices of the Royal Astronomical Society* 476.1, pp. 1050–1070.

- Bandura, Kevin et al. (2014). ‘Canadian hydrogen intensity mapping experiment (CHIME) pathfinder’. In: *Ground-based and Airborne Telescopes V*. Vol. 9145. International Society for Optics and Photonics, p. 914522.
- Battye, RA et al. (2013). ‘H i intensity mapping: a single dish approach’. In: *Monthly Notices of the Royal Astronomical Society* 434.2, pp. 1239–1256.
- Battye, Richard et al. (2016). ‘Update on the BINGO 21cm intensity mapping experiment’. In: Battye, Richard A, Rod D Davies and Jochen Weller (2004). ‘Neutral hydrogen surveys for high-redshift galaxy clusters and protoclusters’. In: *Monthly Notices of the Royal Astronomical Society* 355.4, pp. 1339–1347.
- Blake, Chris, Pedro G Ferreira and Julian Borrill (2004). ‘The angular power spectrum of NVSS radio galaxies’. In: *Monthly Notices of the Royal Astronomical Society* 351.3, pp. 923–934.
- Blake, Chris et al. (2007). ‘Cosmological baryonic and matter densities from 600 000 SDSS luminous red galaxies with photometric redshifts’. In: *Monthly Notices of the Royal Astronomical Society* 374.4, pp. 1527–1548.
- Brown, Michael L, PG Castro and AN Taylor (2005). ‘Cosmic microwave background temperature and polarization pseudo-C estimators and covariances’. In: *Monthly Notices of the Royal Astronomical Society* 360.4, pp. 1262–1280.
- Burgess, CP (2016). *An Introduction to Big Bang Cosmology*. URL: <https://www.physics.mcmaster.ca/~cburgess/Notes/CosmologyNotesRevd.pdf>.
- Carroll, Sean M (2019). *Spacetime and geometry*. Cambridge University Press.
- Chen, Xuelei (2012). ‘The Tianlai project: a 21cm cosmology experiment’. In: *International Journal of Modern Physics: Conference Series*. Vol. 12. World Scientific, pp. 256–263.
- Costa, A. A., R. G. Landim et al. (2021). ‘The BINGO Project VII: Cosmological Forecasts from 21-cm Intensity Mapping’. In: arXiv: 2107.01639 [astro-ph.CO].
- Costa, André A et al. (2017). ‘Constraints on interacting dark energy models from Planck 2015 and redshift-space distortion data’. In: *Journal of Cosmology and Astroparticle Physics* 2017.01, p. 028.
- Dahlen, FA and Frederik J Simons (2008). ‘Spectral estimation on a sphere in geophysics and cosmology’. In: *Geophysical Journal International* 174.3, pp. 774–807.
- Dawson, Kyle S et al. (2012). ‘The Baryon oscillation spectroscopic survey of SDSS-III’. In: *The Astronomical Journal* 145.1, p. 10.
- DeBoer, David R et al. (2017). ‘Hydrogen epoch of reionization array (HERA)’. In: *Publications of the Astronomical Society of the Pacific* 129.974, p. 045001.
- Dodelson, Scott and Fabian Schmidt (2020). *Modern cosmology*. Academic Press.

- Dunkley, J et al. (2009). ‘Five-Year Wilkinson Microwave Anisotropy Probe* Observations: Likelihoods and Parameters from The Wmap Data’. In: *The Astrophysical Journal Supplement Series* 180.2, p. 306.
- Edmonds, Alan Robert (1996). *Angular momentum in quantum mechanics*. Princeton university press.
- Feroz, F, MP Hobson and M Bridges (2009). ‘MultiNest: an efficient and robust Bayesian inference tool for cosmology and particle physics’. In: *Monthly Notices of the Royal Astronomical Society* 398.4, pp. 1601–1614.
- Feroz, Farhan and Mike P Hobson (2008). ‘Multimodal nested sampling: an efficient and robust alternative to Markov Chain Monte Carlo methods for astronomical data analyses’. In: *Monthly Notices of the Royal Astronomical Society* 384.2, pp. 449–463.
- Fisher, Karl B, Caleb A Scharf and Ofer Lahav (1994). ‘A spherical harmonic approach to redshift distortion and a measurement of from the 1.2-Jy IRAS Redshift Survey’. In: *Monthly Notices of the Royal Astronomical Society* 266.1, pp. 219–226.
- Fornazier, K. S. F., F. B. Abdalla et al. (2021). ‘The BINGO Project V: Further steps in Component Separation and Bispectrum Analysis’. In: arXiv: 2107.01637 [astro-ph.CO].
- Gong, Yan et al. (2011). ‘Intensity mapping of the [C II] fine structure line during the Epoch of Reionization’. In: *The Astrophysical Journal* 745.1, p. 49.
- Gorski, Krzysztof M et al. (2005). ‘HEALPix: A framework for high-resolution discretization and fast analysis of data distributed on the sphere’. In: *The Astrophysical Journal* 622.2, p. 759.
- Hall, Alex, Camille Bonvin and Anthony Challinor (2013). ‘Testing general relativity with 21-cm intensity mapping’. In: *Physical Review D* 87.6, p. 064026.
- Hamilton, AJS (2001). ‘Formulae for growth factors in expanding universes containing matter and a cosmological constant’. In: *Monthly Notices of the Royal Astronomical Society* 322.2, pp. 419–425.
- Handley, WJ, MP Hobson and AN Lasenby (2015). ‘PolyChord: nested sampling for cosmology’. In: *Monthly Notices of the Royal Astronomical Society: Letters* 450.1, pp. L61–L65.
- Hartlap, J, Patrick Simon and P Schneider (2007). ‘Why your model parameter confidences might be too optimistic. Unbiased estimation of the inverse covariance matrix’. In: *Astronomy & Astrophysics* 464.1, pp. 399–404.
- Hauser, MG and PJE Peebles (1973). ‘Statistical analysis of catalogs of extragalactic objects. II. The Abell catalog of rich clusters’. In: *The Astrophysical Journal* 185, pp. 757–786.

- Hivon, Eric et al. (2002). ‘Master of the cosmic microwave background anisotropy power spectrum: a fast method for statistical analysis of large and complex cosmic microwave background data sets’. In: *The Astrophysical Journal* 567.1, p. 2.
- Ho, Shirley et al. (2012). ‘Clustering of Sloan Digital Sky Survey III photometric luminous galaxies: the measurement, systematics, and cosmological implications’. In: *The Astrophysical Journal* 761.1, p. 14.
- Hogg, David W (1999). ‘Distance measures in cosmology’. In: *arXiv preprint astro-ph/9905116*.
- Hong, Sungwook E, Changbom Park and Juhan Kim (2016). ‘The most bound halo particle–galaxy correspondence model: comparison between models with different merger timescales’. In: *The Astrophysical Journal* 823.2, p. 103.
- Howlett, Cullan, Marc Manera and Will J Percival (2015). ‘L-PICOLA: A parallel code for fast dark matter simulation’. In: *Astronomy and Computing* 12, pp. 109–126.
- Huterer, Dragan, Lloyd Knox and Robert C Nichol (2001). ‘The Angular Power Spectrum of Edinburgh/Durham Southern Galaxy Catalogue Galaxies’. In: *The Astrophysical Journal* 555.2, p. 547.
- Isserlis, L (1916). ‘On certain probable errors and correlation coefficients of multiple frequency distributions with skew regression’. In: *Biometrika* 11.3, pp. 185–190.
- Kim, Juhan et al. (2015). ‘Horizon Run 4 simulation: Coupled evolution of galaxies and large-scale structures of the Universe’. In: *arXiv preprint arXiv:1508.05107*.
- Kirk, Donnacha et al. (2015). ‘Optimizing spectroscopic and photometric galaxy surveys: same-sky benefits for dark energy and modified gravity’. In: *Monthly Notices of the Royal Astronomical Society* 451.4, pp. 4424–4444.
- Kolb, Edward (2018). *The Early Universe*. CRC Press.
- Kurki-Suonio, Hannu (2015). ‘Cosmological perturbation theory, part 1’. In: *Lecture Notes* 55, p. 56.
- Landy, Stephen D and Alexander S Szalay (1993). ‘Bias and variance of angular correlation functions’. In: *The Astrophysical Journal* 412, pp. 64–71.
- Lesgourgues, Julien (2011a). ‘The cosmic linear anisotropy solving system (CLASS) I: overview’. In: *arXiv preprint arXiv:1104.2932*.
- (2011b). ‘The Cosmic Linear Anisotropy Solving System (CLASS) III: Comparision with CAMB for LambdaCDM’. In: *arXiv preprint arXiv:1104.2934*.
- Levi, Michael et al. (2013). ‘The DESI Experiment, a whitepaper for Snowmass 2013’. In: *arXiv preprint arXiv:1308.0847*.
- Lewis, Antony and Anthony Challinor (2011). ‘Camb: Code for anisotropies in the microwave background’. In: *Astrophysics source code library*, ascl-1102.

- Liccardo, V., E. J. Mericia, C. A. Wuensche et al. (2021). ‘The BINGO projectIV: Simulations for mission performance assessment and preliminary component separation steps’. In: arXiv: 2107.01636 [astro-ph.CO].
- Lidz, Adam et al. (2011). ‘Intensity mapping with carbon monoxide emission lines and the redshifted 21 cm line’. In: *The Astrophysical Journal* 741.2, p. 70.
- Lima, Marcos (2019). ‘Lecture notes in physical cosmology’. unpublished.
- Loureiro, Arthur et al. (2019). ‘Cosmological measurements from angular power spectra analysis of BOSS DR12 tomography’. In: *Monthly Notices of the Royal Astronomical Society* 485.1, pp. 326–355.
- Luo, Yu et al. (2016). ‘Resolution-independent modelling of environmental effects in semi-analytic models of galaxy formation that include ram-pressure stripping of both hot and cold gas’. In: *Monthly Notices of the Royal Astronomical Society* 458.1, pp. 366–378.
- Ma, C and E Bertschinger (1995). ‘Cosmological perturbation theory in the synchronous and conformal Newtonian gauges’. In: *Astrophysical Journal* 455.1.
- Mangano, G et al. (2002). ‘A precision calculation of the effective number of cosmological neutrinos’. In: *Physics Letters B* 534.1-4, pp. 8–16.
- Marins, Alessandro Ribeiro (2018). ‘Observações na linha de 21 cm do hidrogênio: um ajuste fenomenológico para extração das oscilações acústicas de bárions do espectro de potência angular’. MA thesis. Universidade de São Paulo. DOI: 10.11606/D.43.2018.tde-18102018-191432.
- Martin, Ann M et al. (2010). ‘The Arecibo Legacy Fast ALFA Survey. X. The HI Mass Function and from the 40% ALFALFA survey’. In: *The Astrophysical Journal* 723.2, p. 1359.
- McLeod, Michael, Sreekumar T Balan and Filipe B Abdalla (2017). ‘A joint analysis for cosmology and photometric redshift calibration using cross-correlations’. In: *Monthly Notices of the Royal Astronomical Society* 466.3, pp. 3558–3568.
- Melo, Jordany Vieira de (2020). ‘Pipeline do projeto BINGO e não gaussianidade’. MA thesis. Universidade de São Paulo.
- Motta, Pablo (2018). ‘Hierarquia e cosmologia em modelo de Randall-Sundrum’. Available at <http://www.repositorio.ufc.br/handle/riufc/41172>. Bachelor’s Thesis. Universidade Federal do Ceará.
- Newburgh, LB et al. (2016). ‘Proc. SPIE Conf. Ser. Vol. 9906, Ground-based and Airborne Telescopes VI’. In: SPIE, Bellingham.
- Olivari, LC et al. (2017). ‘Cosmological parameter forecasts for H i intensity mapping experiments using the angular power spectrum’. In: *Monthly Notices of the Royal Astronomical Society* 473.3, pp. 4242–4256.

- Olivari, Lucas Collis (2018). *Intensity Mapping: A New Approach to Probe the Large-scale Structure of the Universe*. The University of Manchester (United Kingdom).
- Padmanabhan, Hamsa, Alexandre Refregier and Adam Amara (2019). ‘Impact of astrophysics on cosmology forecasts for 21 cm surveys’. In: *Monthly Notices of the Royal Astronomical Society* 485.3, pp. 4060–4070.
- Padmanabhan, Nikhil et al. (2007). ‘The clustering of luminous red galaxies in the Sloan Digital Sky Survey imaging data’. In: *Monthly Notices of the Royal Astronomical Society* 378.3, pp. 852–872.
- Peebles, PJE (1973). ‘Statistical analysis of catalogs of extragalactic objects. I. Theory’. In: *The Astrophysical Journal* 185, pp. 413–440.
- Perlmutter, Saul et al. (1999). ‘Measurements of Ω and Λ from 42 high-redshift supernovae’. In: *The Astrophysical Journal* 517.2, p. 565.
- Planck, Collaboration et al. (2006). ‘The Scientific programme of planck’. In: *arXiv preprint astro-ph/0604069*.
- Postiglione, Adriana (2017). ‘Cosmological analysis of the angular correlation properties of 2MPZ galaxies’. PhD thesis. Universita’ degli Studi Roma Tre.
- Rassat, Anaïs et al. (2007). ‘Cross-correlation of 2MASS and WMAP 3: implications for the integrated Sachs–Wolfe effect’. In: *Monthly Notices of the Royal Astronomical Society* 377.3, pp. 1085–1094.
- Ribeiro, Williams J. M. (2019). *Observational Constraints on the Dark Energy Equation of State*. arXiv: 1904.11068 [astro-ph.CO].
- Riess, Adam G et al. (1998). ‘Observational evidence from supernovae for an accelerating universe and a cosmological constant’. In: *The Astronomical Journal* 116.3, p. 1009.
- Rindler, Wolfgang (2012). *Essential relativity: special, general, and cosmological*. Springer Science & Business Media.
- Rollins, Richard Peter (2015). ‘Chemical and statistical models of interstellar medium and star-forming regions’. PhD thesis. University of London.
- Santos, Mario G et al. (2017). ‘MeerKLASS: MeerKAT large area synoptic survey’. In: *arXiv preprint arXiv:1709.06099*.
- Scharf, Caleb et al. (1992). ‘Spherical harmonic analysis of IRAS galaxies: implications for the Great Attractor and Cold Dark Matter’. In: *Monthly Notices of the Royal Astronomical Society* 256.2, pp. 229–237.
- Sellentin, Elena and Alan F Heavens (2015). ‘Parameter inference with estimated covariance matrices’. In: *Monthly Notices of the Royal Astronomical Society: Letters* 456.1, pp. L132–L136.

- Skilling, John (2004). ‘Nested sampling’. In: *AIP Conference Proceedings*. Vol. 735. 1. American Institute of Physics, pp. 395–405.
- Takahashi, Ryuichi et al. (2012). ‘Revising the halofit model for the nonlinear matter power spectrum’. In: *The Astrophysical Journal* 761.2, p. 152.
- Thomas, Shaun A, Filipe B Abdalla and Ofer Lahav (2010). ‘Upper bound of 0.28 eV on neutrino masses from the largest photometric redshift survey’. In: *Physical Review Letters* 105.3, p. 031301.
- (2011a). ‘Excess clustering on large scales in the MegaZ DR7 photometric redshift survey’. In: *Physical review letters* 106.24, p. 241301.
- (2011b). ‘The angular power spectra of photometric Sloan Digital Sky Survey luminous red galaxies’. In: *Monthly Notices of the Royal Astronomical Society* 412.3, pp. 1669–1685.
- Tinker, Jeremy L et al. (2010). ‘The large-scale bias of dark matter halos: numerical calibration and model tests’. In: *The Astrophysical Journal* 724.2, p. 878.
- Trotta, Roberto (2017). ‘Bayesian methods in cosmology’. In: *arXiv preprint arXiv:1701.01467*.
- Tulin, Sean and Hai-Bo Yu (2018). ‘Dark matter self-interactions and small scale structure’. In: *Physics Reports* 730, pp. 1–57.
- Villaescusa-Navarro, Francisco et al. (2018). ‘Ingredients for 21 cm intensity mapping’. In: *The Astrophysical Journal* 866.2, p. 135.
- Wang, Bin et al. (2016a). ‘Dark matter and dark energy interactions: theoretical challenges, cosmological implications and observational signatures’. In: *Reports on Progress in Physics* 79.9, p. 096901.
- Wang, Huiyuan et al. (2016b). ‘ELUCID—exploring the local universe with reconstructed initial density field. III. Constrained simulation in the SDSS volume’. In: *The Astrophysical Journal* 831.2, p. 164.
- Weinberg, Steven (2008). *Cosmology*. Oxford university press.
- White, Martin and Mark Srednicki (1994). ‘Window functions for CMB experiments’. In: *arXiv preprint astro-ph/9402037*.
- Wuensche, C. A. et al. (2021a). ‘The BINGO project II: instrument description’. In: *arXiv: 2107.01634 [astro-ph.IM]*.
- Wuensche, Carlos A et al. (2021b). ‘Baryon Acoustic Oscillations from Integrated Neutral Gas Observations: an instrument to observe the 21cm hydrogen line in the redshift range $0.13 < z < 0.45$ —status update’. In: *Anais da Academia Brasileira de Ciências* 93.
- Xavier, Henrique S, Filipe B Abdalla and Benjamin Joachimi (2016). ‘Improving lognormal models for cosmological fields’. In: *Monthly Notices of the Royal Astronomical Society* 459.4, pp. 3693–3710.

- Xiao, Linfeng, Andre A Costa and Bin Wang (2021). ‘Forecasts on Interacting Dark Energy from 21-cm Angular Power Spectrum with BINGO and SKA observations’. In: *arXiv preprint arXiv:2103.01796*.
- Yohana, Elimboto, Yi-Chao Li and Yin-Zhe Ma (2019). ‘Forecasts of cosmological constraints from HI intensity mapping with FAST, BINGO and SKA-I’. In: *Research in Astronomy and Astrophysics* 19.12, p. 186.
- Zhang, J., P. Motta, C. Novaes et al. (2021). ‘The BINGO Project VI: HI Halo Occupation Distribution and Mock Building’. In: arXiv: 2107.01638 [astro-ph.CO].
- Zhang, Jiajun, Dalong Cheng and Ming-Chung Chu (2017). ‘New leaves of the tree: percolation analysis for cosmic web with discrete points’. In: *arXiv preprint arXiv:1708.07602*.
- Zwicky, Fritz (1933). ‘The redshift of extragalactic nebulae’. In: *Helvetica Physica Acta* 6, pp. 110–127.